
A microfabricated chip trap for laser-cooled molecules

Cameron McGarry

A thesis submitted to
IMPERIAL COLLEGE LONDON
DEPARTMENT OF PHYSICS
in partial fulfillment of the requirements for the degree of
Doctor of Philosophy.

Supervised by Mike Tarbutt and Ben Sauer

January 2023

Abstract

I present our efforts to develop a molecule chip: a microfabricated device for trapping ultracold molecules near a surface and interfacing them with photons in a microwave resonator. This work is a step towards a cavity quantum electrodynamics system, where molecular qubits could be coupled and controlled via microwave photons. Such a system would feature both the strong coupling of a molecular transition to cavity photons, similar to those found in superconducting systems, as well as long coherence times as can be found in typical atomic systems. I present the design and construction of a chip capable of trapping ultracold molecules, together with simulations informing the design choices. I report the microfabrication processes used to make the chip, characterize the quality of these processes and describe the design and construction of the apparatus needed to load molecules onto the chip and detect them. I also present a scheme for background-free imaging of molecules near the surface. Finally, I show how a microwave resonator could be used to control the state of a trapped molecule, and describe a scheme for generating non-classical states in a trapped spin-ensemble.

Declarations

I declare that all the work presented in this thesis is my own. Where the work of others has been used it has been correctly and clearly attributed and referenced.

The copyright of this thesis rests with the author. Unless otherwise indicated, its contents are licensed under a [Creative Commons Attribution-NonCommercial-ShareAlike 4.0 International Licence](#) (CC BY-NC-SA).

Under this licence, you may copy and redistribute the material in any medium or format. You may also create and distribute modified versions of the work. This is on the condition that: you credit the author, do not use it for commercial purposes and share any derivative works under the same licence.

When reusing or sharing this work, ensure you make the licence terms clear to others by naming the licence and linking to the licence text. Where a work has been adapted, you should indicate that the work has been changed and describe those changes.

Please seek permission from the copyright holder for uses of this work that are not included in this licence or permitted under UK Copyright Law.

Acknowledgements

If I did one thing right during my PhD it was choosing my supervisors. Ben, you are a font of infinite wisdom in the lab, and have tolerated my bush-league attempts at lab work, and your help in navigating the realities of academic life is hugely appreciated. Mike, you are an incredibly committed individual, and the fact that you constantly made time for me despite your immensely busy schedule is hugely appreciated. Thank you in particular for reading and re-reading this thesis. I am grateful to both of you for your patience and for everything you have taught me.

To the other members of the Centre for Cold Matter, I also thank you for making my time as a PhD student educational and enjoyable. All of you have at some point (or at many points) both taught and helped me. Particular thanks goes to Bharath Srivathsan and Kyle Jarvis who worked directly on the chip experiment with me, suffering many laborious hours in the cleanroom, and showing me what's what, how's what and especially where's what in the lab. The experiment would not exist without Jon Dyne and David Pitman from the CCM workshop produced many of the parts for the experiment. Gautam Kambhampati allowed me to hijack his experiment and collaborated with me on the background-free imaging scheme. He also ensured that I took regular coffee breaks to maximise lab and office productivity. Steve Etienne and Vj Krishnan from LCN, and Amado Bautista-Salvador from Hannover were of great help with the microfabrication. I must of course mention Sanja Maricic and Miranda Toora, who have been unendingly helpful with my various inane requests.

I am grateful to have a wide circle of people to complain to when things have gone wrong. The bored gamers: Aniq, Cathy, Jason, Jay and Yuki, your incessant chat kept me sane when locked indoors for weeks at a time. When we were allowed outside I enjoyed many an evening chatting physics and nonsense in the pub with my course-mates: Alvise, George, Hailey, Oli, Sam, Simon, Sissi and Will. Similar services have been provided by Jamie, Jonny, Luke and Sam. It's sad that we can't spend more time together, but it's always fabulous when we do. To the other friends, from CCCBC, OURCs and elsewhere, I'm sorry that my choice of enormous margins has meant that you didn't quite get squeezed onto this page.

The most welcome distraction from studying over the last four years has been time spent on the river or nearby with coffee. I am grateful to the ladies and coaches of Thames Rowing Club. You never stop impressing me, and I will miss yelling at you: yet, I will not miss regularly waking up before five o'clock in the morning.

Susie, thank you for putting up with me. You always keep me on the right path (figuratively speaking only) and tolerate my ceaseless rambling with enormous grace. Your support is beyond measure and you are my favourite human.

Finally, to my parents: I can't thank you enough for everything you have given me. I love you both.

Contents

1	Introduction	12
1.1	Ultracold atoms	13
1.2	Chip traps	15
1.3	Ultracold molecules	17
1.4	Molecule chip trap	20
1.5	Structure of the thesis	21
2	Background theory	22
2.1	Laser-cooling and trapping	22
2.1.1	Doppler cooling	22
2.1.2	Magneto-optical trap	25
2.1.3	Sub-Doppler cooling	26
2.1.4	Magnetic trapping	28
2.2	Chip trap theory	30
2.2.1	Simple wire traps	30
2.2.2	The H-trap	33
2.2.3	Three dimensional single-wire traps	35
2.3	Physics of diatomic molecules	35
2.3.1	Electronic, vibrational, and rotational energy	37
2.3.2	Transitions	42
2.3.3	Good quantum numbers	44
2.3.4	Hyperfine structure	45
2.3.5	Cooling and trapping molecules	45
3	Overview of the experiment	47
3.1	Existing CaF experiment	47
3.1.1	CaF energy structure and constants	48
3.1.2	Buffer gas source	50
3.1.3	Slowing the beam	51
3.1.4	Capture in a MOT	51
3.1.5	Optical molasses	52

CONTENTS

3.1.6	Magnetic trapping and transport	54
3.1.7	Other experiments and transport	55
3.2	Design requirements and overview	56
4	Simulating the trap	63
4.1	Motion of molecules in a trap	63
4.1.1	Phase-space acceptance	65
4.1.2	Simulating the motion	67
4.1.3	Simulation initialisation	68
4.2	Adiabatic transfer between traps	69
4.3	Trajectory simulation of the initial loading stages	70
4.3.1	MTT - U transfer	72
4.3.2	U - Z transfer	74
4.3.3	Z compression	74
4.3.4	Summary of the simulation	77
4.4	Phase-space acceptance of remaining Z-traps	80
4.5	Summary	82
5	Microfabrication	83
5.1	Overview of the fabrication procedure	83
5.2	Metal evaporation of seed layer	86
5.3	Spin coating of photoresist	87
5.4	Lithography of the wire mould	88
5.4.1	Troubleshooting	88
5.5	Electroplating the tall wires	89
5.5.1	Inspecting the wires	92
5.5.2	Troubleshooting	93
5.6	Etching	95
5.7	Inspecting the finished die	96
5.8	Connection to subchip	96
5.8.1	Gluing and wirebonding	98
5.8.2	Soldering connections	98
5.9	Scaling fabrication	99
5.10	Planned fabrication of microwave layer	100
6	Preliminary experiments	101
6.1	Experiment assembly	101
6.2	Vacuum testing	102
6.3	Current testing	104
6.3.1	Wirebond tests	105

CONTENTS

6.3.2	Solder tests	106
6.3.3	Wire failure	107
6.3.4	Current driver concept	108
6.4	Scatter testing	109
6.5	Background-free imaging	110
6.5.1	Scattering rate and power requirements	111
6.5.2	Identifying the transition frequency	113
6.5.3	Attempt to image the CaF cloud	115
6.6	Summary	115
7	Coupling CaF to on-chip microwaves	117
7.1	The coplanar waveguide	117
7.1.1	CPW properties	118
7.1.2	CPW attenuation	120
7.1.3	CPW resonators	122
7.2	How to couple a molecule to a coplanar waveguide	123
7.2.1	Cavity quantum electrodynamics	124
7.2.2	Stark shift	126
7.2.3	Integrating microwave components	126
7.3	Sideband cooling	128
7.4	Entangling light and photon states	130
7.4.1	State readout	132
7.4.2	State preparation	134
7.4.3	Coupling between molecules	134
8	A method to create non-classical spin states	135
8.1	Spin states of an ensemble	135
8.1.1	Coherent spin states	136
8.1.2	Spin-squeezed states	138
8.2	Spin ensemble coupled to a cavity	140
8.2.1	Spin Hamiltonian	140
8.2.2	Quantum non-demolition measurement of the spin state	141
8.3	Implementation on CaF chip	144
8.4	Outlook	146
9	Outlook	148

List of Figures

2.1	MOT operating principles	26
2.2	Subdoppler cooling	27
2.3	Quadrupole and Ioffe-Pritchard traps	29
2.4	Two-dimensional wire trap	31
2.5	Dimple trap	33
2.6	H-trap	34
2.7	U- and Z-traps	35
2.8	Comparison of H- and Z-traps	36
2.9	Geometry of a diatomic molecule	38
2.10	An electronic transition in a diatomic molecule	43
2.11	Hund's cases	44
3.1	CaF source	48
3.2	The energy levels of CaF	49
3.3	The buffer gas cell	50
3.4	Dual-frequency cooling scheme	52
3.5	Blue-detuned molasses	53
3.6	Hyperfine structure in CaF	55
3.7	Magnetic transport scheme	56
3.8	The CaF and CaF chip experiment	58
3.9	Chip schematic	60
3.10	Chip experiment details	61
3.11	Subchip circuit board design	62
4.1	Phase-space acceptance examples	67
4.2	Geometry of a wire segment	68
4.3	Phase-space simulation initialisation	69
4.4	Simulation of exchange between quadrupole traps	71
4.5	Effect of ramp duration on phase-space distribution	72
4.6	Simulation of transfer from MTT to U-trap	73
4.7	Phase-space distribution throughout MTT-U handover	75

LIST OF FIGURES

4.8	Simulation of transfer from U-trap to Z-trap	76
4.9	Simulation of compression in Z-trap	78
4.10	Summary of loading simulations	79
4.11	Mode-matching on-chip traps	81
5.1	Illustration of the fabrication process	85
5.2	Prototype chip layout	86
5.3	Bell jar evaporation	87
5.4	Photoresist moulds	90
5.5	Electroplating scheme and apparatus	90
5.6	Stylus profiling characterisation features	92
5.7	Electroplating problems and solutions	94
5.8	The importance of a fresh bath	95
5.9	Debris after etching	96
5.10	Features detached from chip on etching	97
5.11	Images of a completed chip	97
5.12	A mounted chip	99
6.1	Chip chamber testing setup	103
6.2	RGA scan of empty and full chambers	105
6.3	Current testing electronics	105
6.4	Increasing current across the small chip wire	107
6.5	A wire before and after destruction	108
6.6	Chip current driver concept	108
6.7	Background scatter from the chip	110
6.8	The RROC scheme for CaF	111
6.9	Optical and vacuum setup for RROC spectroscopy experiment	113
6.10	Fluorescence from CaF due to \mathcal{L}_{01}	114
7.1	Waveguide geometry and field	118
7.2	Conductor losses for a CPW	122
7.3	Capacative coupling schemes for resonator	123
7.4	Two-level cavity QED system	124
7.5	The Stark effect in CaF	127
7.6	Microwave components of the flange assembly	128
7.7	Sideband cooling scheme	129
7.8	Calculated sideband cooling rates	130
7.9	Schematic of a homodyne measurement	133
8.1	Graphical representation of a coherent spin state	137
8.2	Graphical representation of a spin-squeezed state	139

LIST OF FIGURES

8.3	Effect of squeezing on state uncertainty	146
8.4	Relationship of squeezing parameter to measurement uncertainty . . .	146
8.5	Representation of a Schrödinger cat spin state	147

List of Tables

1.1	Typical properties of various on-chip systems	18
3.1	Lasers, transitions and wavelengths	48
3.2	CaF constants	50
3.3	Trapping wire properties	59
7.1	Various dielectric constants	121
7.2	Various electrical constants	121

Chapter 1

Introduction

Recently there has been great progress in the production of ultracold molecules by direct laser cooling and trapping [1]. On the whole, progress in this field has followed the existing roadmap of atomic experiments, from laser slowing, to magneto-optical trapping, to optical dipole trapping. Another cold atom experiment, the chip trap, does not yet have a molecular analogue. As we will see below, this tool has proven to be of great use as a robust, compact and portable device for cold atom experiments. A molecular counterpart could prove equally invaluable, and could provide capabilities beyond those of atom chips. This could include strong coupling to on-chip microwave fields and the realisation of a cavity quantum electrodynamics system, exploiting the long coherence times of rotational states of molecules and their strong electric dipole coupling to resonant microwave fields.

The molecule chip was originally proposed by André et al. [2] as a means of leveraging the long coherence times of a diatomic molecule in combination with robust control using on-chip microwave guides. In this proposal a single molecule is trapped in the near field of a resonator, where strong-coupling between molecular transitions and cavity photons can be leveraged for state control and readout. The built-in integration with microwave photons would allow the exchange of information via a flying qubit, either to other devices on the same chip, or to other separate devices. It is possible to envision how such a device is scalable, and could be used to interact with other quantum devices that operate in the microwave regime, such as superconducting charge qubits. Since the rotational states display long coherence states (typical of existing atomic systems) and can be strongly coupled to the cavity photons (similarly to superconducting systems) it may even be possible to achieve a ‘best of both worlds’ scenario which improves on existing quantum architectures.

At the time of this proposal, the field of ultracold molecules was in its infancy. Today it is possible to create dense clouds of ultracold molecules, which are ripe for loading onto a chip trap. In this thesis I will describe the work that has been undertaken to implement such a device. This chapter will further motivate my

research, starting with a review of cold atoms, to atom chips and then cold molecules. I will then summarise the motivation for a molecule chip and outline the structure of the thesis.

1.1 Ultracold atoms

Laser cooling of atoms is a developed field, with the 1997 Nobel Prize in Physics having been awarded to Cohen-Tannoudji, Chu and Phillips for ‘development of methods to cool and trap atoms with laser light’ [3]. This subject is reviewed in various texts, with the canonical reference being Metcalf and van der Straten [4]. Here I will give a brief qualitative overview of the topic and its many applications in modern physics, which include quantum information, communication and metrology. Further details on these cooling mechanisms are given in section 2.1.

In a typical laser slowing experiment, the forward velocity of a beam of atoms is reduced by resonant, counter-propagating laser light. An atom can absorb a photon from the laser and, upon spontaneous re-emission, this photon has no preferred direction of travel. Over a large number of these photon scatters the result is a net reduction in the forward velocity of the atoms [5]. This principle of slowing with radiation pressure was first observed by Wineland et al. [5] in Mg ions, but one of the key goals of laser slowing was to reduce the velocity of a beam of neutral atoms (produced in, for example, an oven) as was achieved by Andreev et al. [6].

A further goal was to reduce the velocity even further, so that the slowed atoms could be loaded into a magnetic trap. To achieve this it is essential to account for the change in the resonant frequency of the atoms due to the Doppler shift that occurs as the atom’s velocity is reduced. Phillips and Metcalf [7] were able to achieve this for Na atoms by the Zeeman slowing technique, where a changing magnetic field across the beamline is used to ensure the relevant transition is always resonant with the light. Later the same group would achieve the same effect by chirping the frequency of the light [8], so that the light is sufficiently red-shifted to be resonant with the atoms as they slow down. Such experiments must take place under ultra high vacuum to prevent loss by collisions with a background gas.

Another key development was the implementation of the magneto-optical trap (MOT) where atoms were confined by a quadrupole magnetic field and red-detuned laser light incident from every direction. This scheme is designed so that atoms that are away from the trap centre experience a Zeeman shift that brings them into resonance with the light. The polarisations are then chosen so that the atom will preferentially scatter photons from the beam that produces a restoring force towards the trap centre. This results in a much stronger restoring force than in a pure magnetic trap, and also produces a velocity-dependent damping to reduce

the temperature of the atoms. This was first implemented by Raab et al. [9], also in Na, although subsequently many different species have been laser-cooled and confined in a MOT.

Due to the stochastic nature of photon scattering, there is a fundamental limit on the lowest temperature that can be achieved using just the Doppler cooling mechanism. Early studies of Doppler cooling in a 3D optical molasses found that in fact, anomalously low temperatures were reached [10]. This was eventually explained by Dalibard et al. [11] as being due to sub-Doppler cooling mechanisms, which rely on polarisation gradients set up in the light field. This reduced the atom temperature close to the recoil limit, which is related to the energy imparted by a single photon scatter.

Once the atoms are cooled to sub-millikelvin temperatures, it becomes possible to trap them without dissipation, that is in a conservative trap. Two main types have become popular – the magnetic trap and the optical dipole trap. In a magnetic trap, atoms are pumped into a weak-field seeking state, and trapped at a local magnetic field minimum, such as can be created, for example, by a pair of anti-Helmholtz coils [12]. In an optical dipole trap atoms are confined by intense, far-off-resonant light [13]. This light induces an a.c. Stark shift, which produces an attractive potential towards the region where the light's intensity is greatest.

For a sufficiently tight optical dipole trap, an optical tweezer is formed, where a single atom can be trapped and easily manipulated by controlling the light [14]. A series of tweezer traps can be used to form a lattice of traps [14], with individually-trapped atoms able to interact with each other by dipole-dipole interactions. A lattice can also be formed in a standing wave optical trap (SWOT), where light reflected from a surface creates a series of local field maxima for trapping of atoms [15].

Inside a magnetic or optical dipole trap it becomes possible to cool beneath even the recoil limit by evaporative cooling, where the hottest atoms are ejected from the trap. The remaining atoms thermalise at a lower temperature than the original cloud. This technique was employed by Anderson et al. [16] to cool ^{87}Rb to sufficiently low temperature and density to form a Bose-Einstein condensate (BEC), earning Cornell and Wieman a share of the 2001 Nobel prize. This prize was also shared with Ketterle, who undertook similar work with Na atoms [17].

With this ability to reliably create low-temperature atomic clouds (or even a single cold atom) confined in traps and lattices, comes the ability to create quantum devices for simulation, communication and metrology, with promises of future applications in quantum computing. Coherent control of atoms in optical lattices for simulation has been demonstrated [18], and optical lattice clocks have become the cutting edge in timekeeping [19]. There are numerous examples of atoms being used for precise sensing, for example, acceleration [20] including gravity [21]. Cold

atoms can also be employed to explore fundamental physics, such as the search for dark matter [22]. Future experiments also plan to utilise cold atoms for new gravitational wave detectors operating in frequency bands that are inaccessible to existing detectors [23].

These experiments, and those like them, have been made easier by technological developments such as atom dispensers, which remove the need to cool a hot beam of atoms, and vapour cells, which can entirely remove the need for a complicated vacuum system. This has led the way to miniaturisation and scalability of cold atom experiments, which is an active field of research. The complexity of these experiments can be further reduced by using, for example pyramid [24], mirror [25, 26] or grating [27] MOTs, where some of the MOT light beams are produced by reflection or diffraction from a surface. These are strongly linked to the main focus of this thesis: the chip trap.

1.2 Chip traps

The chip trap was proposed as a mechanism for studying atoms in very high-gradient magnetic traps [28], but it has evolved into a useful tool for miniaturised and robust cold atom experiments. These can be integrated with, for example, microwave components, to form hybrid quantum systems. Further details will be presented in section 2.2, but here I will give a brief overview of the operating principles and history of atomic chip traps. I will also explain why loading molecules onto a chip may be a useful development of these experiments.

We have already discussed the idea of trapping atoms in a quadrupole magnetic field using macroscopic current-carrying coils. It is also possible to generate magnetic traps from the field of a wire combined with a homogeneous bias field. In a chip trap experiment, the wires are positioned on the surface of a substrate, and can be made very small (on the scale of a few microns) by the use of common microfabrication techniques. Various microscopic atom traps were pioneered by Hänsch and Zimmermann at the Max Planck Institute of Quantum Optics (MPQ) and Tübingen [29, 30], as well as in Harvard [31]. This was followed by work in Innsbruck, where Li atoms were guided using a two dimensional trap formed with a free-standing wire [32].

The first true chip traps, operating in three dimensions were reported by the MPQ group [25], who also implemented a mirror-MOT for loading ^{87}Rb into their traps. This was shortly followed by developments in controlling and guiding Li atoms trapped above a chip's surface from Innsbruck [33]. Atom chips were soon found to be a robust tool for cold atom experiments, including the production of BECs, with groups from the Ludwig Maximilian University of Munich and Tübingen both

reporting ^{87}Rb BECs at the same conference in 2001 [34, 35]. Since then atom chips have been used to investigate lower dimensional gasses, as reported in Refs. [36, 37, 38], and have found uses in various other experiments as a convenient method of preparing cold atomic clouds [39]. This includes experiments creating non-classical spin-squeezed states (see chapter 8), implementing magnetic lattices [40] and performing interferometry [41].

2004 saw the first implementation of an on-chip Michelson interferometer, based on the creation, splitting and guiding of BECs all on a chip. In the same year, the prospect of integrated atom chip devices was fully realised at the National Institute of Standards and Technology, where a compact and portable atomic chip clock was developed [42] based on the hyperfine transitions in Cs. This has since become a commercial product with uses across a variety of fields, such as military and space science [43] including an atom chip experiment conducted on board the International Space Station [44].

Also in 2004, it was demonstrated by the MPQ group that coherence times of around 1 s could be achieved for ^{87}Rb atoms held in a chip trap within 100 μm of the surface [45]. In this experiment microwave fields were used to drive hyperfine transitions in the molecules, with the microwave radiation delivered from an external source. This was soon extended to experiments where the microwaves were delivered by on-chip microwave components built on a two-layer device [46, 47], with a view to develop a microwave trap and perform quantum gates entirely on-chip.

The work of the Munich group built towards coherent control of an atom coupled to on-chip microwaves, however a more ambitious goal is the coupling of an atom to a microwave cavity, which can lead to powerful control over the spin system by leveraging the effects of cavity quantum electrodynamics. One requirement of this is so-called strong coupling between the microwave photons and the atomic transition, which is challenging due to the comparatively small transition matrix element of the hyperfine transitions in the atoms, and the need for a high quality microwave cavity. The latter of these, as we will discuss in chapter 7, requires the use of superconducting microwave components.

A superconducting atom chip is an attractive idea, since as well as the potential for low-loss microwave components, superconducting wires can produce deeper magnetic traps. The first such device was first realised by Haroche's group in Paris in 2006 [48], with a BEC on a superconducting chip following in 2008 [49]. Similar superconducting wire traps were used to investigate the Meissner effect [50], and subsequent development of these superconducting atom chips lead to full quantum control of an atom cloud held in place above a superconducting microwave resonator [51]. Here the resonator was designed to be off the atomic resonance, so that the internal state of the trapped atoms were unaffected by its presence. Of

additional note in this paper is the loading scheme used for the chip – an optical tweezer is used to bring the atoms from a room-temperature environment to within 400 μm of the chip surface, before being transferred to surface-based microtraps.

A later experiment [52] would see the coupling of atoms to the microwave resonator, realising a hybrid atom-microwave system, and the investigation of microwave cavity quantum electrodynamics. Rabi oscillations between hyperfine transitions could be driven, but strong coupling was not realised. It has been possible to couple atoms strongly to monolithic microresonators [53], but only in free fall, not whilst trapped. Further work in the Hogan group at University College London has achieved stronger coupling by utilising the enormous electric dipole moment of transitions in Rydberg atoms [54]. Again, such experiments are performed with atoms that are in flight, and in this case travelling at supersonic speeds.

An improvement to such experiments would be to confine the atom close to the microwave field, near the anti-node of the resonator to maximise the coupling strength. However, another potential method is to use a molecule with high electric dipole moment instead of a Rydberg atom. Recent advances in the laser-cooling and trapping of diatomic molecules make these an exciting prospect for implementing a microwave cavity QED device, as was originally proposed by André et al. [2]. In the next section we will briefly review this field, before further outlining the prospects for a molecule chip trap.

1.3 Ultracold molecules

There are a number of potential benefits that can come from cooling molecules rather than atoms. As already mentioned, molecules have a rich energy structure, including the rotational states. These are closely-spaced energy levels of opposite parity, with strong electric dipole transitions between them. Hence, molecules are far more polarisable than atoms and couple strongly to d.c. electric fields and resonant microwave fields, and also to one another through their dipole-dipole interactions. Together with their long coherence times, this makes them an attractive candidate for use in quantum technologies, as shown in Table 1.1. Molecules also allows the investigation of fundamental physics, such as the measurement of the electron’s electric dipole moment, which has helped to constrain particle physics theories that go beyond the standard model [55].

The energy structure of molecules is far richer than that of atoms; a diatomic molecule will have both vibrational and rotational energy levels, which can be leveraged for novel imaging schemes, strong coupling to microwave transitions, amongst other applications. However these introduce additional complications that make experiments with ultracold molecules more challenging than their atomic equivalents.

System	$\Omega_{\text{typ}}/(2\pi)$	τ_{typ}
Superconducting	100 MHz	$\sim 100 \mu\text{s}$
Atomic	20 kHz	$> 1 \text{ s}$
Molecular	1 MHz	$> 1 \text{ s}$

Table 1.1: Typical Rabi frequencies (Ω_{typ}) and coherence times (τ_{typ}) for various quantum systems on chips. Molecules can achieve sufficient Rabi frequencies to reach the strong-coupling regime, whilst also offering long coherence times as seen in atomic systems. See Refs. [1, 2, 56, 57, 58].

There are two main schools of ultracold molecule experiments. In the first of these gases of cold atoms are used to synthesise cold molecules, usually by association via a Feshbach resonance [59]. In this thesis we will focus on the second school: direct cooling of hot diatomic molecules. The first experiment to successfully trap molecules was reported by Weinstein et al. [60], who created calcium monohydride (CaH) molecules by laser ablation, and then cooled them to below the depth of a magnetic trap by buffer-gas cooling. In this technique, an inert buffer gas is used as an intermediary to thermalise the molecules with a cold copper cell typically held at a few kelvin. An alternative technique to slow a beam of molecules was developed in Gerard Meijer’s group, who used Stark deceleration to first slow a beam of carbon monoxide [61], and later to slow then electrostatically trap ammonia in both a quadrupole trap [62] and a storage ring [63, 64]. However these methods produce molecules that are orders of magnitude warmer than the atoms produced by laser cooling.

Buffer gas cooling has become a staple of cold molecule experiments, being routinely used in the production of slow, high-flux molecular beams [65, 66, 67]. Optical cycling in a diatomic molecule with the potential of laser slowing was first seen using strontium monofluoride (SrF) by DeMille’s group [68]. To account for the more complex energy structure of the molecule, additional lasers were used to repump the molecule from states that were dark to the cooling transition. Despite this difficulty, the DeMille group had soon enough applied the technique to achieve laser-slowing [69] and eventually an SrF MOT in 2014 [70, 71]. The initial report boasted temperatures of 2.5 mK and there was scope to reduce this further.

Alongside the development of laser-cooling SrF, there have been developments in the laser-cooling of various other molecules, notably yttrium oxide (YO), ytterbium monofluoride (YbF) and calcium monofluoride (CaF), the latter being the main molecule of focus in this thesis. YO has been trapped in a MOT, stored in a lattice and cooled to the order of a micro kelvin [72]. YbF has been used in various experiments to measure the electric dipole moment of the electron [73], and it is hoped that laser-cooling could be a method for further improving the precision of this experiment [74]. Meanwhile, CaF shows promise as a molecule of interest for

investigating quantum information and the fundamentals of quantum chemistry. Laser-slowing of CaF was first observed in the Centre for Cold Matter (CCM) at Imperial College London [75], where a supersonic beam was slowed by 20 m s^{-1} using a chirped beam of light. The CaF experiment was further developed with the implementation of a buffer gas source for CaF [76], with further developments in laser slowing coming from both CCM [77] and the Doyle group in Harvard [78].

A CaF MOT was first reported by CCM [79] in 2017, followed by the Harvard group [80]. These experiments took slightly different approaches to avoid the pumping of molecules into dark states: the Imperial College group used a dual frequency technique [81], while the Harvard group used an r.f. switching technique that was first developed in Jun Ye's group at JILA [82]. The CaF MOT has opened the door to experiments with large clouds of CaF molecules, with today's MOTs capable of loading $\sim 10^5$ molecules [80]. The temperatures of these clouds can be further reduced to below the Doppler limit [83, 84] and can then be further trapped and controlled by some of the same techniques already discussed above for atoms. This includes confinement in magnetic traps [85] and in an optical dipole trap and lattice [86]. Further cooling schemes such as transverse cooling (similar to that seen for YbF in Ref. [87]) and Zeeman-Sisyphus cooling have been demonstrated [88, 89]. Combining these various schemes with ongoing research into collisions with atoms [90] and sympathetic cooling could see even lower CaF temperatures achieved in the near future.

CaF has shown to have promise in quantum information and simulation, with coherent control in a magnetic trap having been demonstrated [85, 91] with coherence times of over 1 s plausibly achievable [92]. Coherent control of the molecule has also been demonstrated in a dipole trap [93], showing that there is significant potential for the implementation of quantum simulations and computing. Further novel schemes for molecule-based quantum information have been proposed, such as those described for topological quantum computing in Ref. [94] or for the implementation of qudits in Ref. [95].

Another topic of interest is collisions between cold molecules and cold atoms. This has recently been observed in NaLi molecules by Son et al. [96], and in CaF at Imperial College [97, 98]. The thermalisation of molecules with atoms could lead to further temperature reduction by sympathetic cooling, which may be enhanced in a dipole trap. It also paves the way for investigations into quantum chemistry at a very fundamental level. Recent research into the production of polyatomic MOTs by the Harvard group [99] will no-doubt also play an important role in such investigations.

To summarise, research into ultracold molecules is rapidly developing, with methods for producing cold, dense clouds of diatomic molecules already available. The

rich energy structure of molecules makes them a promising candidate for use in quantum information, communications and sensing experiments including in chip-based devices.

1.4 Molecule chip trap

We have seen in the above discussion that ultracold molecules can be a useful tool in quantum information and simulations. Further, recent developments in cooling techniques mean that we are now able to produce dense clouds of molecules such as CaF, which exhibit long coherence times in magnetic traps. Various techniques that have been applied to cold atoms have been equally successfully applied to cold molecules, but a conspicuous absence in the preceding discussion is a chip trap for ultracold molecules.

Such a device is of significant interest, since it provides a robust and stable architecture for quantum experiments could prove extremely useful when applied to cold molecules. In addition to the magnetic traps discussed above, polar molecules can be contained in electrostatic traps, which could be leveraged to construct traps similar to existing ion chip traps [2, 100]. Such devices are inherently scalable, with the ability to constrain multiple molecules at various sites across the chip surface. They can then be transported by changing the electric potentials, which simply amounts to changing the voltages on trapping electrodes.

Another very significant benefit of a molecule chip system is that the rotational transitions in a diatomic molecule can couple very strongly to microwave fields, much more so than the hyperfine transitions in atoms (see Table 1.1). André et al. [2] propose that building a molecule chip with integrated microwave guides, similar to equivalent atom chips reported in Ref. [48], could enable strong coupling between microwaves and rotational states, resulting in the production of powerful tools for quantum information and communication. Amongst these are the ability to carry out a state-dependent measurement of the molecule. This, along with the ability to drive microwave transitions using the guide, allows the device to be totally self contained – once molecules are loaded all interactions can be performed electrically. The long-lived rotational states of CaF make this molecule a promising candidate for such a device.

Along with readout, strong coupling to a resonator could allow for the implementation of a novel sideband cooling scheme to reduce the molecule’s motional energy to the ground state of the trapping potential. It would also be possible to couple molecules on neighbouring trapping sites using the resonator as a bus. Similarly it may be possible to extend the interaction to longer ranges, since photons can be used as flying qubits to couple quantum mechanical systems over long distances.

The schemes mentioned in this section will be explored further in chapter 7.

There has been some work investigating molecules trapped close to chips, mainly by the Meijer group, who have designed and implemented microfabricated Stark decelerators [101], and even trapped molecules on a chip [102]. However, similar to their other work, these molecules are much hotter than can be achieved with laser-cooling.

This thesis describes the work that has been undertaken in CCM to build a microfabricated chip trap for CaF molecules at ultracold temperatures. I will outline a design inspired by existing atom chips, and the proposals in Ref. [2]. This design will provide a stepping stone towards more advanced devices, which can realise strong coupling between rotational transitions in CaF and microwaves in a cavity, leading to the implementation of the various schemes described above. It will integrate with the existing experiment, and take advantage of the properties of CaF, including the long coherence times of rotational transitions that can be achieved in magnetic traps.

1.5 Structure of the thesis

In chapter 2 I will introduce key background theory: laser-cooling of simple systems, the operation of chip traps, and the physics of diatomic molecules. Next, chapter 3 gives an overview of the existing CaF experiment, as well as some particulars of the laser-cooling methods used specifically for CaF. Here I will also outline the new chip experiment, and how it will integrate with the existing apparatus. We have studied the loading procedure for the trap with simulations, and these are presented in chapter 4.

I microfabricated chip traps, as will be discussed in chapter 5, and then loaded these into a vacuum chamber for initial testing. This included testing that the current capacity of the trapping wires was as expected, that ultra-high vacuum could be reached, and that it will be possible to image molecules without too much background scatter created by the chip. These tests, and a scheme to reduce the background scatter are discussed in chapter 6. Chapter 7 describes how a microwave guide and resonator can be implemented as part of the experiment, as well as the behaviour of a single molecule coupled to a microwave cavity. I will extend this idea for ensembles of molecules coupled to a cavity in chapter 8, where I propose a scheme to use a quantum non-demolition measurement to create a spin-squeezed state in such an ensemble. Finally, chapter 9 describes the future prospects for this project.

Chapter 2

Background theory

This chapter outlines some background theory that will be important throughout the rest of the thesis. In section 2.1 I will give an abstracted overview of the principles of laser-cooling and trapping of atoms and molecules, including magnetic traps. In section 2.2 I will explain how it is possible to create magnetic fields for such traps using wires on the surface of a chip. Finally in section 2.3 I will introduce the structure of diatomic molecules, which is essential for understanding how to apply these techniques to our experiment.

2.1 Laser-cooling and trapping

2.1.1 Doppler cooling

We will introduce Doppler cooling in the idealised case of a two-level atom or molecule (henceforth the particle) travelling in one dimension, x . Say that light is incident on the particle from the positive x direction. If the light is resonant with an internal transition then the particle can absorb a photon, which will at some later time be re-emitted when the particle spontaneously decays. This two-step process – absorption followed by spontaneous emission – is the scattering of photons by the particle. The absorbed photons all come from the beam of light, whereas the spontaneously emitted photons have no preferred direction, so over a large number of these scattering events the average effect is a net reduction in the atom's velocity in the positive x direction.

In order to quantify this process, we might start by asking ourselves, what is the force exerted on the particle by the photons? This will be

$$F = \text{photon momentum} \times \text{scattering rate}. \quad (2.1)$$

The momentum of a photon with frequency ω

$$p_\gamma = \hbar k = \frac{\hbar\omega}{c}, \quad (2.2)$$

where c is the speed of light, \hbar is the reduced Planck constant, and $k = 2\pi\omega/c$ is the photon's wavenumber. The scattering rate will be the product of the decay rate of the transition (its linewidth) Γ and the population of the excited state ρ_{22} . We use this notation to denote the excited state population, since it can be found by solving the optical Bloch equations in the rotating wave approximation and in steady state. This gives [4]

$$\rho_{22} = \frac{\Omega^2/4}{(\omega - \omega_0)^2 + \Omega^2/2 + \Gamma^2/4}. \quad (2.3)$$

Here Ω is the Rabi frequency,

$$\hbar\Omega = \langle g | \mathbf{d} \cdot \mathbf{E} | e \rangle, \quad (2.4)$$

with $|g\rangle$ and $|e\rangle$ as the ground and excited state of the transition respectively, \mathbf{d} as the dipole operator, and \mathbf{E} as the driving field. We introduce $\gamma = \Gamma/2$, as well as the unitless parameters $\delta = (\omega - \omega_0)/\gamma$ and $s = 2\Omega^2/(\Gamma^2)$ so that

$$\rho_{22} = \frac{s/2}{\delta^2 + 1 + s}. \quad (2.5)$$

We can now write down the scattering rate

$$R = \frac{s\gamma}{\delta^2 + 1 + s} \quad (2.6)$$

and the force follows as

$$F = \frac{s\gamma}{\delta^2 + 1 + s} \hbar k. \quad (2.7)$$

At this point it is useful to note that the scattering rate will be saturated for sufficiently large s . When the detuning is small, saturation occurs when $\delta \ll 1 \ll s$. Hence the saturation condition is $\Omega^2 \gg \Gamma^2/2$. This can be used to determine the intensity at which the transition will be saturated. Using eqn (2.4) and relating the field amplitude to the intensity by

$$I = \frac{c\epsilon_0 E^2}{2} \quad (2.8)$$

the saturation intensity (the intensity at which $s = 1$) is

$$I_s = \frac{c\epsilon_0 \Gamma^2}{4} |\langle g | \mathbf{d} \cdot \mathbf{E} | e \rangle|^{-2} \quad (2.9)$$

where we have re-written the field vector in terms of its amplitude (E) and direction (ϵ which is a unit vector), $\mathbf{E} = E\epsilon$. Note also that we can write $s = I/I_s$.

The force acting on the particle can be related to its velocity by the Doppler effect. A particle moving at speed v will have its resonant frequency shifted to new frequency ω' such that

$$\frac{\omega' - \omega_0}{\omega_0} = \frac{v}{c}, \quad (2.10)$$

Therefore δ can be re-written as

$$\delta \rightarrow \delta_+ = \delta + \frac{\omega_0}{\gamma c} v, \quad (2.11)$$

where δ represents the detuning of the laser from the resonant frequency at rest, and the second term is the additional shift due to the Doppler effect. For a particle with $v > 0$, this means that the light must be red-shifted to remain resonant with the particle's transition (or blue-shifted for $v < 0$).

However, what if the light is incident from the negative x direction? This is analogous to changing the sign of v in the above case, so we can immediately write

$$\delta \rightarrow \delta_- = \delta - \frac{\omega_0}{\gamma c} v. \quad (2.12)$$

By combining counter-propagating beams, it is possible to create a net force

$$F_{\text{res}} = F_+ + F_-, \quad (2.13)$$

where

$$F_{\pm} = \frac{s\gamma}{\delta_{\pm}^2 + 1 + s} \hbar k. \quad (2.14)$$

For small v we perform a Taylor expansion around $v = 0$ to find that

$$F_{\text{res}} \approx \frac{s\delta}{(1 + s + \delta^2)^2} 4\hbar k^2 v. \quad (2.15)$$

Which is maximised when $\delta = -1$ and $s = 1 + \delta^2 = 2$, so that

$$F_{\text{max}} = -\alpha v, \quad (2.16)$$

where $\alpha = -\hbar k^2/2$.

Hence the counter-propagating beams provide a velocity-dependent damping force. We call this arrangement an optical molasses, and it can equally be applied in three dimensions. It is important to note that the particles will not be brought to a standstill under this effect. The molasses force does not contain the information on the heating that occurs when the particles re-emit the absorbed photons.

This stochastic process limits the minimum attainable temperature to the Doppler temperature [4]

$$T_D = \frac{\hbar\Gamma}{2k_B}. \quad (2.17)$$

2.1.2 Magneto-optical trap

Doppler cooling is an important tool in the creation of ultracold atoms and molecules, but it is of note that this technique does not provide any position-dependent restoring force. In other words, particles that are slowed by the above-described techniques are not trapped. The magneto-optical trap (MOT) is the preeminent tool of atomic and molecular physics, providing a way to trap a relatively cold gas of particles. It is the backbone of many experiments including the cooling and trapping of CaF molecules, which is the starting point for this work [79]. In this section I will describe the basic operation of the common type-I MOT, that is a two level system where the ground state has total angular momentum F and the excited state has total angular momentum F' such that $F' > F$. In this example $F = 0$ and $F' = 1$ are chosen. In reality the molecule MOT that we will discuss is a type-II MOT ($F' \leq F$), as will be discussed in section 2.3.5.

The MOT consists of two components, a magnetic quadrupole field, and restoring laser beams, which are detuned from the $F \rightarrow F'$ transition by some amount δ . This setup is shown for one dimension in Fig. 2.1. The Zeeman effect lifts the degeneracy of the excited state, and introduces the energy shift [103]

$$\Delta E = g_F m_F \mu_B B, \quad (2.18)$$

where g_F is the Landé g-factor, μ_B is the Bohr magneton, and B is the magnetic field. For a one-dimensional quadrupole field, we write $B = B'x$, where B' is the field gradient. We therefore have a position-dependent change in the energy. Note that for negative x , the $m_F = -1$ state has lower energy, and for positive x the $m_F = 1$ state has lower energy (when $g_F > 0$, if $g_F < 0$ this is reversed). The detuning δ is chosen such that this shift brings the lowered state into resonance with the light so that the particle will then preferentially absorb photons when it is away from the trap centre.

We wish to ensure that when a photon is absorbed the momentum change provides a restoring force towards the centre of the MOT. This is achieved by choosing the polarisation so that the light coming from the positive (negative) direction drives σ^+ (σ^-) transitions. The result is that the particle will then always absorb light that is propagating towards the centre of the trap, resulting in a restoring force. We also observe the same Doppler cooling force from the molasses, so the resulting force

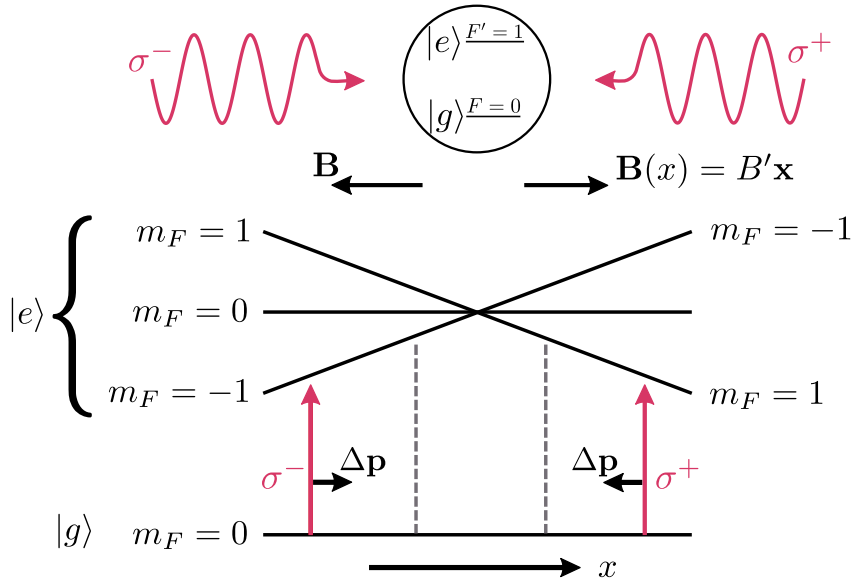


Figure 2.1: Illustration of the operating principle of a one-dimensional MOT on a two-level system with $F = 0$ and $F' = 1$. The particle is represented by the circle, and has counter-propagating beams of light (pink arrows) incident on it. A quadrupole magnetic field is applied, lifting the degeneracy of the excited state as shown by the black lines. The light is red-detuned so as to be resonant with the transition to the lower m_F state, but only the restoring beam will be absorbed due to the choice of polarisation. The direction of the momentum change $\Delta \mathbf{p}$ is indicated by the black arrows. The excited state will decay back to the ground state (dashed lines).

is

$$F = -\alpha v - \left(\frac{\mu_B B'}{\hbar k} \right) \alpha x. \quad (2.19)$$

2.1.3 Sub-Doppler cooling

We might expect that a MOT would cool the atoms to around the Doppler temperature, but in fact the temperature reached is often lower, due to sub-Doppler cooling effects that often occur in a MOT. The most common of these is polarisation gradient cooling, which cannot occur in the $F = 0, F' = 1$ system used to introduce the MOT. We instead consider a new system with $F = 1/2, F' = 3/2$ which we note is still a type-I MOT.

In the centre of the MOT where there is near zero magnetic field, the m_F states of the system would be degenerate except that the degeneracy can be lifted by the field of the light. This is the a.c. Stark shift, which is a function of the light's polarisation. For red-detuned light, the shift is negative for all the ground states, and is proportional to the square of the Rabi frequency. Hence it is also proportional to the square of the transition dipole moment, which depends on the light's

polarisation. When the light drives σ^+ transitions, the $m_F = 1/2 \rightarrow m'_F = 3/2$ transition will be the strongest, and hence experience the greatest shift. This example is pictured, along with the relative matrix elements, in Fig. 2.2 (a). For the case of σ^- transitions being driven, similar reasoning means that the $m_F = -1/2$ state is lower.

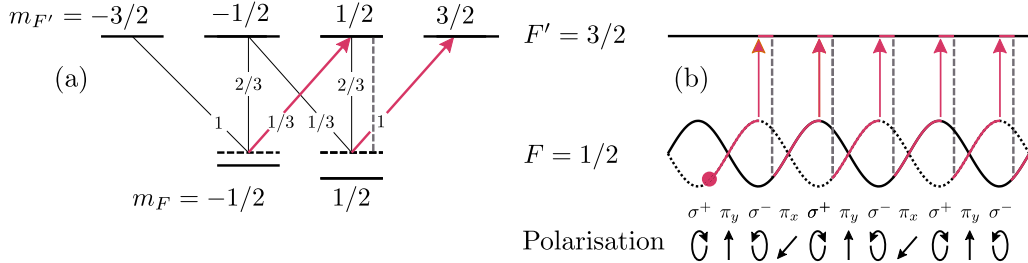


Figure 2.2: In (a) we have the optical pumping scheme, and polarisation shift for σ^+ light. The relative coupling strengths (squared values shown inline) cause the $m_F = 1/2$ state to be reduced further than $m_F = -1/2$. The reverse is true for σ^- light. The optical pumping (pink arrows and dashed decay) show how population can be transferred to $m_F = 3/2$. A similar scheme can be used to pump to $m_F = -3/2$ with σ^- light. Subfigure (b) shows the polarisation gradient cooling scheme described in the main text. The polarisation gradient is depicted in the bottom row, and the $m_F = 1/2$ ($m_F = -1/2$) state is shown by the dashed (solid) line. A particle in the molasses (pink circle) will follow a path such as the one shown here in pink, being pumped into the $F' = 3/2$ state at the top of the potential hill, then decaying (dashed grey lines) back to the lower of the ground states and climbing the hill again. The vertical scaling is different between the two figures for clarity.

The counter-propagating beams establish a polarisation gradient across the trap, and hence the Stark shift of the ground states also varies across the trap, as shown in Fig. 2.2 (b). The detuning of the light means that whichever of the m_F states is higher is preferentially excited to the excited $F' = 3/2$ level. The atom can then decay into the lower of the two ground states, where it will follow the potential curve until it is pumped again. The particles on average spend more time climbing the potential than descending it, and therefore expend energy through this process, reducing their temperature to the recoil limit, which corresponds to the energy exchanged by a single photon scatter

$$T_{\text{recoil}} = \frac{\hbar^2 k^2}{m k_B} \quad (2.20)$$

which is normally on the order of $1 \mu\text{K}$. Normally to achieve such low temperatures the magnetic field of the MOT is switched off, so that only the molasses is active, and the polarisation gradient cooling occurs across the entire cloud. Lower temperatures can be reached by other techniques such as evaporative cooling [4].

2.1.4 Magnetic trapping

The MOT is an important tool for trapping, and can be configured in various ways [9, 24, 104], but there is considerable benefit to being able to confine particles using only a magnetic field. Primarily, a magnetic trap can be a conservative potential, where the total energy of the system remains the same, and transitions do not need to be actively driven to maintain the trap. This allows for coherent control of particles in trappable states. Another benefit of a magnetic trap is that since there is no light involved, it is much easier to control the trapping potential. This opens the door to applications in guiding [105] and transporting [106] particles, but also confining close to a surface such as that of a chip. This will be discussed in more detail in the next section, but for the moment we limit ourselves to a basic description of magnetic trapping.

Continuing with the above example of a two-level particle with $F = 1/2$, $F' = 3/2$, we notice that when the particle is in a state where $g_F m_F > 0$, the Zeeman shift due to a magnetic field is positive (c.f. eqn (2.18)). Hence if the magnetic field B is chosen such that there is a local minimum in the vicinity of the particle, then these states will be attracted to that minimum. Such a state is called a weak-field seeker. We can equally have strong-field seekers when $g_F m_F < 0$, but these cannot be magnetically trapped since, according to Earnshaw's theorem, it is not possible to create a local magnetic field maximum in free space. Note that the dependence here is on the magnitude of the magnetic field, so the direction of the field does not directly affect the trapping potential.

To magnetically trap our particle we need to first ensure it is in a weak-field seeking state, and then we need to introduce a magnetic field with a local minimum. The first of these is readily achieved by optical pumping [12]. A suitable magnetic field can be formed in many ways, but the canonical choice is the quadrupole trap, which can be formed from a pair of anti-Helmholtz coils, as shown in Fig. 2.3 (a). We can approximate the field generated near the centre of such a configuration as [4]

$$\mathbf{B} = B' \begin{pmatrix} -x/2 \\ -y/2 \\ z \end{pmatrix}, \quad (2.21)$$

where B' is the field gradient in the z direction, and depends on the currents in the coils as well as their geometry.

One of the drawbacks to a quadrupole is that the magnetic field at the centre is zero. In regions of low field there is no breaking of the degeneracy, and so it is possible for the m_F quantum number to change to an untrappable state. This is known as a spin-flip or Majorana loss [107]. One method of resolving this is to instead use a

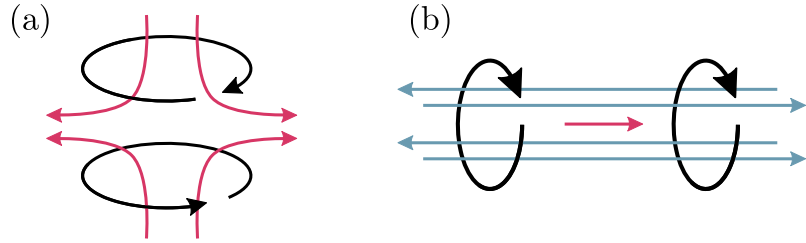


Figure 2.3: Subfigure (a) demonstrates the generation of a quadrupole field (pink arrows) by anti-Helmholtz coils (black arrows). Subfigure(b) demonstrates the current configuration for a Ioffe-Pritchard trap, with longitudinal currents (blue arrows) and endcap coils (black arrows) The field near the trap centre is also shown (pink arrow).

Ioffe-Pritchard trap, which has a non-zero field minimum. The standard method of implementing such a trap is shown in Fig. 2.3 (b). Four straight wires are arranged in a square, with a pair of parallel coils on either end to form end-caps. The field generated is of the form

$$\mathbf{B} = b_1 \begin{pmatrix} x \\ -y \\ 0 \end{pmatrix} + b_0 \begin{pmatrix} 0 \\ 0 \\ 1 \end{pmatrix} + b_2 \begin{pmatrix} -xz \\ -yz \\ z^2 - \rho^2/2 \end{pmatrix}, \quad (2.22)$$

where $\rho^2 = x^2 + y^2$ and the constants b_i are again functions of the currents and the geometry.

For a quadrupole field, the motion is characterised by the gradient, but for a Ioffe-Pritchard trap, the motion is harmonic, and we can find the frequencies by evaluating the shape of the potential μB , where μ is the magnetic moment of the trapped state. From eqn (2.22) we have

$$\mu B \approx \mu \sqrt{b_0^2 + (b_1^2 - b_0 b_2) \rho^2 + 2b_0 b_2 z^2} \quad (2.23)$$

and higher order position terms. Now expanding for $z = 0$ and small ρ we get

$$\mu B \approx \mu b_0 \left(1 + \frac{b_1^2 - b_0 b_2}{2b_0} \rho^2 \right) \quad (2.24)$$

which is a harmonic potential with minimum μb_0 and frequency

$$\omega_\rho = \sqrt{\frac{\mu}{m} \left(\frac{b_1^2}{b_0} - b_2 \right)} \quad (2.25)$$

for a particle of mass m .

Similarly for the z direction, we can find the potential approximates to

$$\mu B = \mu b_0(1 + b_2 z^2) \quad (2.26)$$

which is again harmonic, with frequency

$$\omega_z \approx \sqrt{\frac{\mu}{m} 2b_2}. \quad (2.27)$$

Note that if the orientation of the magnetic field at the particle changes too quickly, due to the motion of the particle through the inhomogeneous field, spin flip transitions will be driven. To avoid this, we typically require that $(dB/dt)/B$ to be small compared to $g_F \mu_B B / \hbar$. Provided this condition is satisfied, the particle will adiabatically follow the changing magnetic field and there will be no loss. Similarly, the field can be changed adiabatically (slowly compared to the speed of the trapped particles) without heating. This can be used for transport, or transferring particles between magnetic traps, and will be discussed further in chapter 4.

2.2 Chip trap theory

The main subject of this thesis is the trapping of particles near chips. In this section we will see that it is possible to use wires on a chip, combined with external magnetic fields to produce trapping potentials that resemble either a quadrupole or Ioffe-Pritchard trap. Further details can be found in Ref. [108].

2.2.1 Simple wire traps

We begin our discussion by considering a simple case of a two-dimensional trap. This will be formed from a straight wire carrying current I , which we approximate to have infinite length. Such a wire can be free-standing or deposited on a substrate. The magnetic field due to the wire is described by the Biot-Savart law, having magnitude

$$B_w(r) = \frac{\mu_0 I}{2\pi r}, \quad (2.28)$$

where r is the distance from the wire. The direction of the field obeys the right hand rule. With such a geometry it is possible to create a rudimentary two-dimensional trap at a distance h from the wire, by applying an external bias field $\tilde{\mathbf{B}}$, whose direction opposes the field of the wire. To create the trap at the desired bias, the strength of the bias field must be $\tilde{B}_y = B_w(h)$.

Figure Fig. 2.4 illustrates this two-dimensional trap. Here the wire is oriented along the x direction, with the current $I = 1 \text{ mA}$, flowing in the positive direction

(out of the page). This generates the expected field \mathbf{B} shown in subfigure (a). This is superimposed with the bias field $\tilde{\mathbf{B}}_y$, also shown in (a), to produce the resulting field $\mathbf{B} = \mathbf{B}_w + \tilde{\mathbf{B}}$ shown in (b). This subfigure details the field lines (pink arrows) and field magnitude, shown by the colour gradient (blue, guide to the eye) where darker areas indicate lower field. The bias field is chosen to induce a field minimum at $h = 1$ mm. Subfigure (c) shows a cut through of the potential along y with $x = 0, z = h$. Subfigure (d) also shows a cut through of the potential along z with $x = y = 0$. This demonstrates the two-dimensional trap.

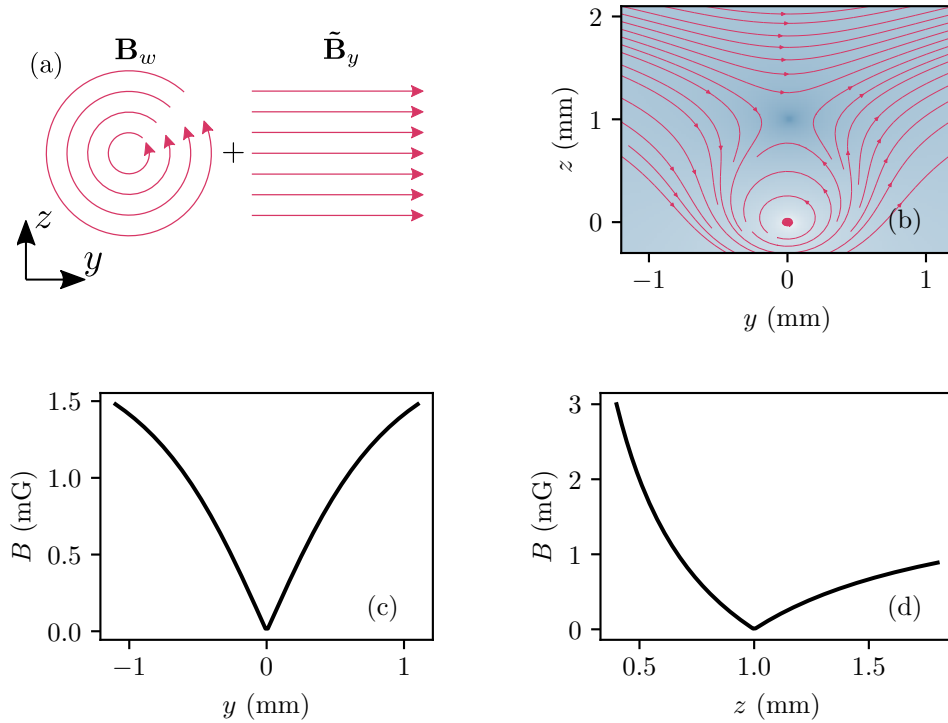


Figure 2.4: The field from a simple two-dimensional wire trap. In subfigure (a) a wire carries current $I = 1$ mA in the positive x direction (out of the page) to create the usual field \mathbf{B}_w . This is combined with the external bias field $\tilde{\mathbf{B}}_y$ to create the two-dimensional trap at height $h = 1$ mm shown in subfigure (b). The field lines are shown by pink arrows, and the magnitude of the resulting field is shown with the blue gradient (darker means weaker field, guide to the eye). Cut throughs of the potential are shown for y (with $x = 0, z = h$) in (c) and for z (with $x = y = 0$) in (d).

Since the field minimum here is a zero, we can approximate the value near the centre by a (two-dimensional) quadrupole with gradient. The gradient will be the normal gradient of the wire field at the trap centre

$$B'_w(h) = \left. \frac{dB_w}{dz} \right|_{z=h} = -\frac{\mu_0 I}{2\pi h^2}, \quad (2.29)$$

where the height can be written in terms of the bias field by eqn (2.28), and using $B_w(h) = -\tilde{B}_y$

$$h = -\frac{\mu_0 I}{2\pi \tilde{B}_y}. \quad (2.30)$$

So the gradient near the centre is

$$B' = -\frac{2\pi \tilde{B}_y^2}{\mu_0 I}. \quad (2.31)$$

The depth of the trap is $\mu \tilde{B}_y$, where μ is the magnetic dipole moment of the trapped particle. This can be seen in Fig. 2.4 (d): the potential is $B = |B_w(z) + \tilde{B}_y|$, and so has an asymptote at $B = |\tilde{B}_y|$ as $z \rightarrow \infty$. It is useful to write this depth as a temperature

$$T = \frac{\mu \tilde{B}_y}{k_B}. \quad (2.32)$$

We can transform such a trap into a Ioffe-Pritchard trap by applying a second bias field along the x direction to lift the field minimum away from zero.

Of course, it is commonly desirable to trap in all three dimensions. A simple way to introduce confinement along the x axis is to introduce a second wire trap acting in the perpendicular direction. Such a device is called a dimple trap (or cross conductor trap, or X-trap) and is illustrated in Fig. 2.5. We label the current in the second wire I_1 and the new bias field, which is parallel to the x -axis and opposes the I_1 field is labelled \mathbf{B}_x . In the case that $I_1 \ll I$, the second wire can be treated as a perturbation of the first. The field minimum is therefore still at h , and its depth is given by eqn (2.32).

The dimple trap can be used as a quadrupole trap when the bias fields are chosen to exactly cancel the magnetic field at the centre, or it can be used as a Ioffe-Pritchard trap when there is a non-zero minimum. We will focus on the latter case. The trapping frequencies can be obtained as follows. The trapping from the I wire will be stronger than the x -axis confinement from the I_1 wire, hence the trapping frequency in this direction (ω_x) will be lower than the trapping frequency in the other directions (ω_\perp). We again write down the field minimum

$$B_0 = \left| \tilde{B}_x + \frac{\mu_0 I_1}{2\pi h} \right|, \quad (2.33)$$

the transverse gradient

$$B'_\perp = \frac{\mu_0 I}{2\pi h^2}, \quad (2.34)$$

and the curvature along the weak component

$$B'' = \frac{\mu_0 I_1}{\pi h^3}. \quad (2.35)$$

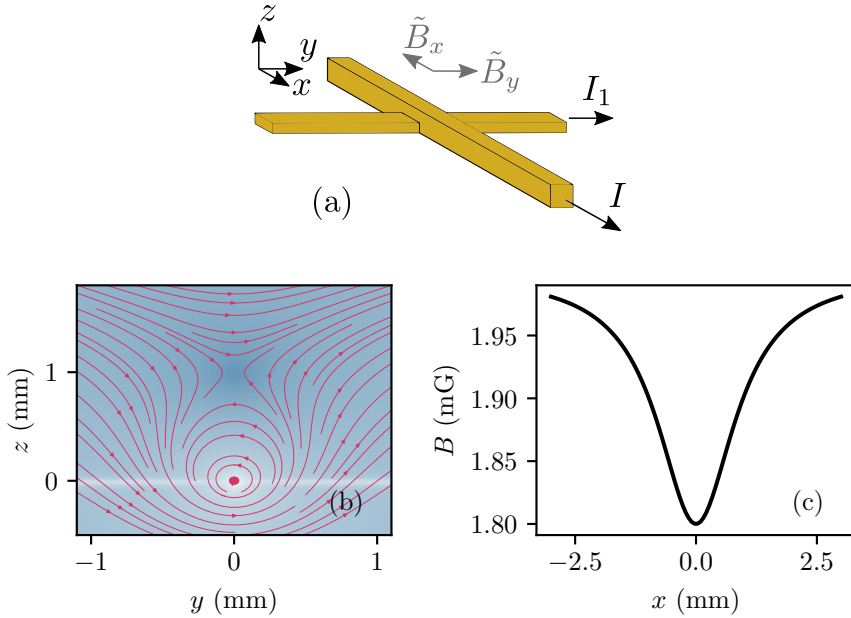


Figure 2.5: The geometry of the dimple trap is shown in subfigure (a), with the new wire along y carrying current I_1 intersecting the I wire. An additional bias field in the x direction, \tilde{B}_x creates the field minimum. The field lines (pink) and magnitude (blue, darker is weaker, guide to the eye) is shown in subfigure (b) along $x = 0$. Note the strong field region along the y axis around the I_1 wire. Subfigure (c) shows a cut through of the trapping potential in the x direction with $y = 0$, $z = h$.

The trap frequencies can be found by comparing to the frequencies of a general Ioffe-Pritchard trap (see eqn (2.22)) and noting that $B'' \ll B'^2/B_0$. Hence we have in the strong direction

$$\omega_{\perp} = \sqrt{\frac{\mu B_{\perp}^{\prime 2}}{m B_0}}, \quad (2.36)$$

where m is the particle mass. In the weak direction (along x) the frequency is

$$\omega_x = \sqrt{\frac{\mu B''}{m}}. \quad (2.37)$$

It is worth noting that in this simplified diagram, and in those to follow, the wires are shown as touching. In reality it is common to electrically isolate the wires from one another during fabrication. However in section 6.3.4, we will also present a scheme for how electrically connected wires can have their currents controlled independently.

2.2.2 The H-trap

Consider the dimple trap, but with \tilde{B}_x set to zero. Now what was previously a magnetic field minimum will be a field maximum. By putting two such dimple traps

next to each other, it is possible to create a local minimum within which we can trap molecules. Such a trap is called an H-trap, and is pictured in Fig. 2.6. We label the current due to the second dimple trap I_2 , and again note that the bias field in the x direction can be set to zero. The distance between I_1 and I_2 is denoted d , and we now refer to the wire carrying current I as the axis of the trap.

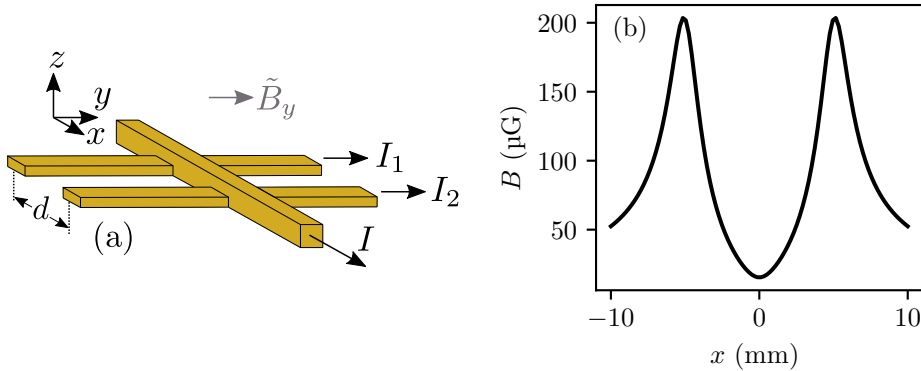


Figure 2.6: The geometry of the H-trap is shown in subfigure (a). In subfigure (b) we show the potential for an H-trap with $I_1 = I_2 = I/10 = 0.1$ mA and $d = 10$ mm. Again the bias field is chosen so that $h = 1$ mm.

We note that we need not choose I_1 and I_2 to be the same, although from now on we will assume that they have the same magnitude; the sign can differ. In other words these currents can be parallel or anti-parallel. In the former case the wires form a Ioffe-Pritchard trap; this is due to the fields from I_1 and I_2 adding in the centre, to provide some overall non-zero component in the x direction. When the currents are anti-parallel, the I_1 field opposes the I_2 field in the centre of the trap, the two cancel and there is a field zero. Hence the latter configuration is a quadrupole trap.

In the Ioffe-Pritchard configuration, we can write down the field's minimum

$$B_0 = \tilde{B}_x + 2\tilde{B}_y \frac{I_1}{I} \frac{h^2}{(d/2)^2 + h^2} \quad (2.38)$$

transverse gradient

$$B'_\perp = \frac{2\pi\tilde{B}_y^2}{\mu_0 I} \quad (2.39)$$

and curvature [109]

$$B'' = \tilde{B}_x + 2\tilde{B}_y \frac{I_1}{I_0} \frac{h^2}{(d/2)^2 + h^2} \quad (2.40)$$

and the trap frequencies are again given by equations 2.36 and 2.37 [109]. In the quadrupole configuration, the trap is characterised by the perpendicular gradient B'_\perp .

2.2.3 Three dimensional single-wire traps

Although the H-trap provides a method of creating a three dimensional microtrap, it is not always convenient to have to use three distinct wires. Fortunately the H-trap can be approximated by a single wire, either in a U-shape for the quadrupole variant, or a Z-shape for the Ioffe-Pritchard variant [108]. These are pictured in Fig. 2.7. Note that for the U-trap the currents in the off-axis wires are once again anti-parallel, and in the Z-trap these currents are parallel. For the U- and Z-traps, we denote the distance between the end wires as d , and refer to the direction of the current in the central wire as the axis.

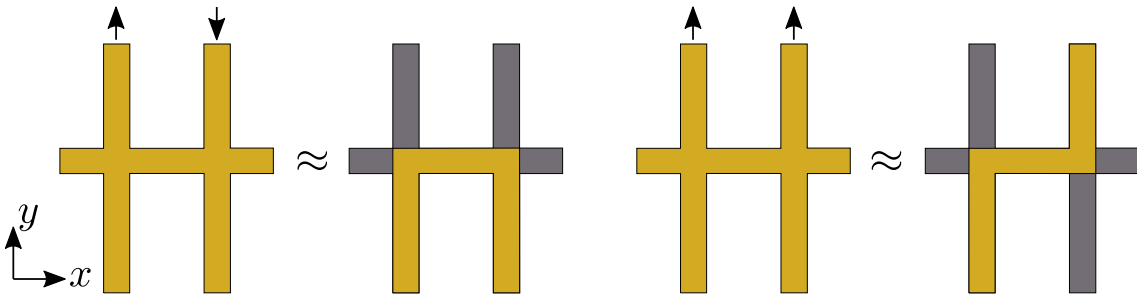


Figure 2.7: Current configuration for U-trap (Z-trap) approximating the quadrupole (Ioffe-Pritchard) H-trap configuration.

The Z-trap will be the primary focus of this thesis, and so we will focus on this as an example. In Fig. 2.8 we compare an H-trap with a current of 1 mA on each wire with the potential due to a single Z-wire also with current 1 mA. In both cases $d = 10$ mm, and a bias field of 2 mG in the y direction is chosen, so as to create a minimum at approximately $z = 1$ mm from the axis. The potentials are similarly comparable for the H-trap in quadrupole configuration and the U-trap. Note that the ambient magnetic field in the lab can be zeroed by the use of shim coils outside the experiment.

This illustrates that a single current-carrying wire can be used to form a trap in three dimensions. The examples here use length scales of a few millimeters, and have typical depths of 100 nK, but we will discuss in chapter 4 that it is possible to realise much smaller and deeper traps.

2.3 Physics of diatomic molecules

Up to this point we have considered abstracted and idealised systems, but in the next chapter we will begin to think about the realities of trapping cold molecules on a chip. It is essential that we introduce and understand the energy structure of diatomic molecules, which is far richer and more complex than the structure of atoms due to the additional effects of vibration and rotation of the two nuclei. This

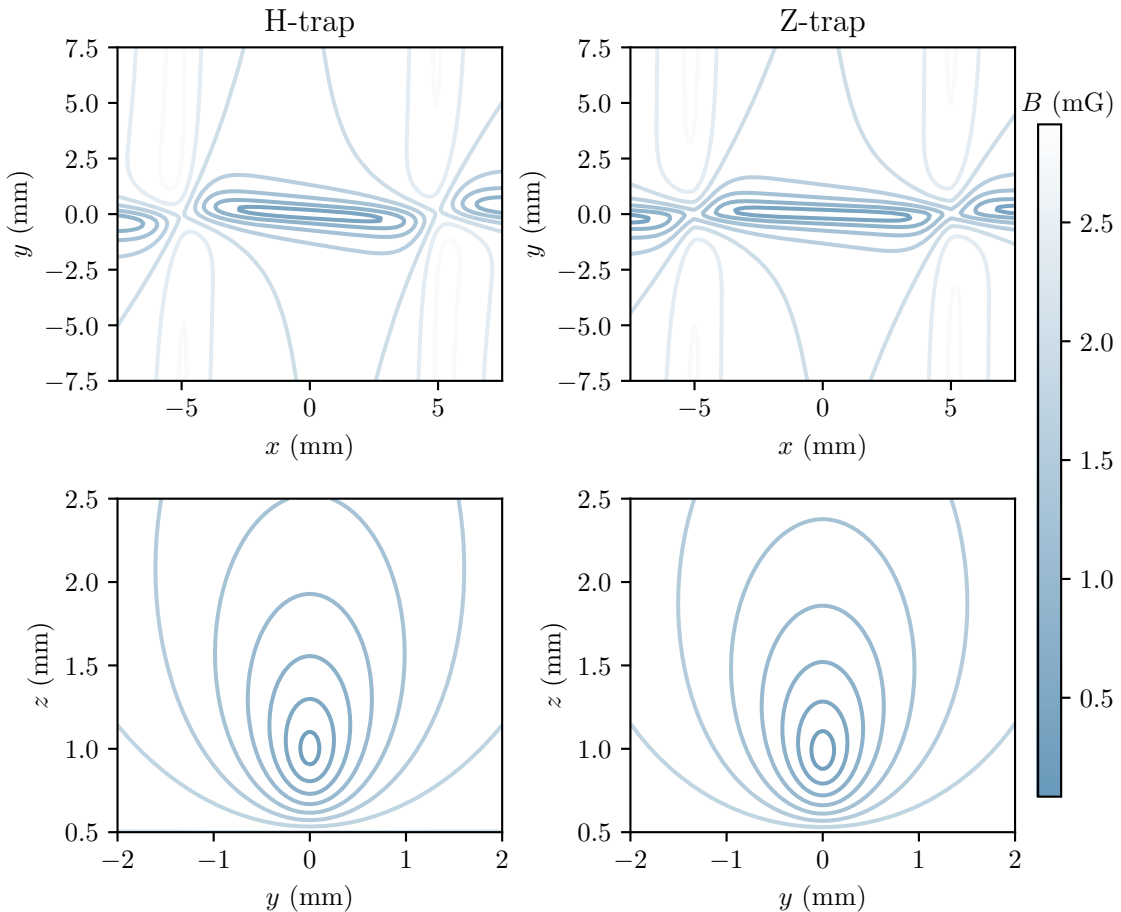


Figure 2.8: Contour plots comparing the potentials ($B = \sqrt{\mathbf{B} \cdot \mathbf{B}}$) for a H-trap in Ioffe-Pritchard configuration (left column) and Z-trap (right column), with cut throughs for $z = 1$ mm (top row) and $x = 0$ (bottom row). All wires carry a current of $I = 1$ mA and a bias field of 2 mG is applied in the y direction.

section will explain the physics of diatomic molecules so that the particulars of the cooling transitions and magnetically trappable states can be easily explained in the next chapter. A more detailed review of the topic can be found in Ref. [110].

2.3.1 Electronic, vibrational, and rotational energy

We can begin by considering two atoms, which we label A and B , with masses m_i , $i \in \{A, B\}$ and m_p is the proton rest mass. We say that the location of the atoms is \mathbf{R}_i and the distance between them is R_{AB} where $\mathbf{R}_{AB} = \mathbf{R}_B - \mathbf{R}_A$. In the case that $R_{AB} \rightarrow \infty$ we have two distinct atoms that will behave as we would expect them to in isolation (see, for example, Ref. [56]).

As R_{AB} is reduced, the atoms will begin to perturb each other, with the perturbation dominated by the Coulomb interaction between the various charges. We can write down the Hamiltonian of such a system, and it is most useful to do so in the centre of mass (COM) frame, with the reduced mass

$$m_{\text{red}} = \frac{m_A m_B}{m_A + m_B} \quad (2.41)$$

and COM location

$$\mathbf{R}_{\text{COM}} = \frac{m_A \mathbf{R}_A + m_B \mathbf{R}_B}{m_A + m_B}. \quad (2.42)$$

The Hamiltonian is then the sum of the terms arising from the Coulomb interaction, and the motion of the molecules

$$H = T_n + T_e + V_{nn} + V_{en} + V_{ee}, \quad (2.43)$$

where

$$T_n = -\frac{\hbar^2}{2m_{\text{red}}} \nabla_{AB}^2, \quad (2.44)$$

$$T_e = -\frac{\hbar^2}{2m_e} \sum_{i=1}^{N_e} \nabla_i'^2 - \frac{\hbar^2}{2(m_A + m_B)} \sum_{i,j} \nabla_i' \cdot \nabla_j', \quad (2.45)$$

$$V_{nn} = \frac{Z_A Z_B e^2}{4\pi\epsilon_0 R_{AB}}, \quad (2.46)$$

$$V_{en} = -\frac{e^2}{4\pi\epsilon_0} \sum_{i=1}^N \left(\frac{Z_A}{R_{Ai}} + \frac{Z_B}{R_{Bi}} \right), \quad (2.47)$$

$$V_{ee} = \frac{e^2}{4\pi\epsilon_0} \sum_{i < j} \frac{1}{R_{ij}}, \quad (2.48)$$

and we have introduced the relative distances R_{ij} being the distance between the i^{th} and j^{th} electrons, and R_{Ai} the distance between A and the i^{th} electron (and similar for B) as shown in Fig. 2.9. The total number of electrons is N_e . The primed

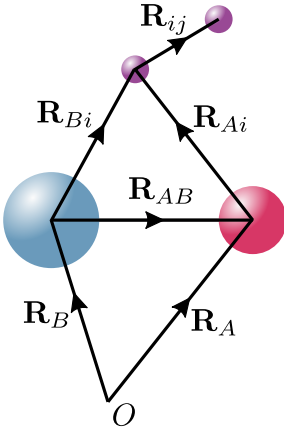


Figure 2.9: The geometry of a diatomic molecule, with relevant vectors labelled. Nuclei in blue and pink, electrons in purple.

gradient operators represent differentiation with respect to the COM coordinates. These terms represent the kinetic energy of the nuclei and the electrons in the COM frame (T_n and first term in T_e respectively), the various Coulomb attraction and repulsions V_* terms), and the so-called mass polarisation term. This is the second term in eqn (2.46), and it is a correction term to account for small fluctuations in the COM. This is necessary since the movement of any one particle will change the position of the COM, hence the particle coordinates are all coupled in this frame. Fortunately this term can usually be neglected, or treated as a perturbation [110, 111]. The time-independent Schrödinger equation (TISE),

$$H\psi = E\psi \quad (2.49)$$

can now in principle be solved for this Hamiltonian, although we will only sketch the solution here. A full derivation can be found in Ref. [110].

Electronic states

The wavefunction ψ is a function of \mathbf{R}_{AB} and the position of each of the electrons, that is

$$\psi = \psi(\mathbf{R}_{AB}, \mathbf{R}_1, \dots, \mathbf{R}_{N_e}). \quad (2.50)$$

We now make the Born-Oppenheimer approximation, where we say that because the nuclear mass is much higher than that of the electrons, the nuclei are stationary on the timescale of the electronic motion. For this reason we are able to separate the wavefunction into the electronic and nuclear parts

$$\psi(\mathbf{R}_{AB}, \mathbf{r}) = \psi_e(\mathbf{R}_{AB}; \mathbf{r})\psi_n(\mathbf{R}_{AB}). \quad (2.51)$$

Note here that \mathbf{R}_{AB} is treated as a parameter of ψ_e and we have introduced $\mathbf{r} = \{\mathbf{R}_1, \dots, \mathbf{R}_{N_e}\}$ to represent the set of electronic coordinates.

There is then a separate electronic TISE

$$H_e \psi_e(\mathbf{R}_{AB}; \mathbf{r}) = E_e(R_{AB}, \mathbf{r}) \psi_e(\mathbf{R}_{AB}; \mathbf{r}), \quad (2.52)$$

where the Hamiltonian $H_e = H - T_n$ is the previous Hamiltonian but excluding the term for the nuclear motion. This problem now begins to resemble the analogous one of finding the electronic states of atoms, and can be solved by similar numerical methods [56, 112]. The upshot is that it is possible to determine the electron eigenstates, which we label $\psi_e(\mathbf{R}_{AB}; q)$, with q being the quantum number for the electronic configuration¹. The energy of the state is now denoted $E_e(q; R_{AB})$, with q as a parameter and E_e a function of R_{AB} . It is common to approximate this energy as the Morse potential

$$E_e(q; R_{AB}) = D(1 - e^{-\beta(R_{AB} - R_{AB}^0)})^2, \quad (2.53)$$

where R_{AB}^0 is the equilibrium displacement of the nuclei, D is the dissociation energy, and β is a parameter for the width of the potential. All of these are dependent on the electronic configuration, but this dependence is suppressed in the notation. From here on, we suppress the dependence of E_e on R_{AB} and write $E_e(q; R_{AB}) = E_e(q)$.

Implicit in the Born-Oppenheimer approximation is that the electronic configuration is the largest contribution to the state's energy. We can make a naive estimate of this energy as the typical kinetic energy of the electrons

$$E_e \approx \frac{p^2}{2m_e} = \frac{\hbar^2}{2m_e a^2}, \quad (2.54)$$

where $a \sim 1 \text{ \AA}$ is the length scale of the molecule and m_e is the electron mass, so that $E_e/h \sim 1000 \text{ THz}$. This gives us the first order contribution to the energy of the molecule.

Nuclear motion

We now turn our attention to the nuclear wavefunction. It is possible to continue manipulation of the Hamiltonian so as to write down the relevant TISE for the nuclei [110]

$$\left(-\frac{\hbar^2}{2m_{\text{red}}} \nabla_{AB}^2 + E_e(q; R_{AB}) - E \right) \psi_n(\mathbf{R}_{AB}) = 0. \quad (2.55)$$

¹The numbering of the electronic configurations is actually more complicated than this. We will discuss how these states are labelled in section 2.3.3.

Note that the potential that the nuclei move through is the potential generated by the electron configuration, and that this potential is central. We can therefore anticipate the separation of the nuclear wavefunction into radial and angular parts,

$$\psi_n(\mathbf{R}_{AB}) = \frac{1}{R_{AB}} f(R_{AB}) Y_{R,m_R}(\theta, \phi), \quad (2.56)$$

where we choose the factor of $1/R_{AB}$ to simplify the equation in the rest of the section. We will introduce the operator \mathbf{R} to describe the rotational angular momentum. The angular part of the solution is given by the usual spherical harmonics Y_{R,m_R} where

$$\mathbf{R}^2 Y_{R,m_R} = R(R+1) Y_{R,m_R}, \quad (2.57)$$

$$R_z Y_{R,m_R} = m_R Y_{R,m_R}. \quad (2.58)$$

The rotational quantum number for the state, and m_R is the projection onto the z -axis.

Substitution of eqn (2.56) into eqn (2.55) yields

$$\left(-\frac{\hbar^2}{2m_{\text{red}}} \frac{d^2}{dR_{AB}^2} + \frac{\hbar^2 R(R+1)}{2m_{\text{red}} R_{AB}^2} + E_e(q; R_{AB}) - E \right) f(R_{AB}). \quad (2.59)$$

where we have expanded ∇_{AB}^2 in terms of the second derivative in R_{AB} and the angular momentum operator \mathbf{R}^2 . This equation is now that of an oscillator in the Morse potential $E_e(q; R_{AB})$, with an additional energy term that arises due to the rotation,

$$E_{\text{rot}}(R) = \frac{R(R+1)}{2m_{\text{red}}(R_{AB}^0)^2}. \quad (2.60)$$

Here we have approximated the internuclear separation to be at its equilibrium value.

The vibrational part of the wavefunction can be solved by the standard computational methods for finding the wavefunctions of anharmonic potentials [56]. These vibrational states form a ladder of states inside an anharmonic potential [103] as pictured in Fig. 2.10. We label these states with the quantum number v , and so re-write $f(R_{AB}) = f_v(R_{AB})$ to clarify which vibrational level we are referring to.

At low energy the Morse potential approximates to a harmonic potential

$$E_e(q; R_{AB}) \approx D\beta^2(R_{AB} - R_{AB}^0)^2, \quad (2.61)$$

where the vibrational frequency is related to the potential by

$$\frac{1}{2} m_{\text{red}} \omega_{\text{vib}}^2 (R_{AB} - R_{AB}^0)^2 = D\beta^2 (R_{AB} - R_{AB}^0)^2. \quad (2.62)$$

We can estimate this vibrational frequency by considering the opposite limit, near dissociation. We approximate D to be the typical electronic energy E_e and note that for dissociation to occur we expect $\beta(R_{AB} - R_{AB}^0) > 1$ and also that at this point $(R_{AB} - R_{AB}^0)^2 \sim a^2$. We therefore substitute into eqn (2.62) $D \approx E_e$ and $\beta \approx a^{-1}$

$$\hbar\omega_{\text{vib}} \approx \sqrt{\frac{\hbar^4}{m_{\text{red}} m_e a^4}} \sim h \times 10 \text{ THz}, \quad (2.63)$$

where we took $m_{\text{red}} \approx m_p$. The vibrational energy E_{vib} can be approximated for low v as a harmonic oscillator, so that

$$E_{\text{vib}}(v) \approx \hbar\omega_{\text{vib}} \left(v + \frac{1}{2} \right). \quad (2.64)$$

We now have an estimate for the vibrational energy, and the final step is to compare this to the rotational energy in eqn (2.60), where we expect typical values

$$E_{\text{rot}}(0) = \frac{\hbar}{2m_{\text{red}} R_{AB}^0} \sim h \times 100 \text{ GHz} \quad (2.65)$$

it is clear that the rotational energy levels can be treated as perturbations of the vibrational levels.

Qualitative summary

We have described how the wavefunction of a diatomic molecule in free space can be written as three separate wavefunctions, one each for the electronic, vibrational and rotational Hamiltonians. We denote the wavefunction in the form

$$\psi_{q,v,R,m_R} = \frac{1}{R_{AB}} \psi_e(\mathbf{R}_{AB}; q) f_v(R_{AB}) Y_{R,m_R}(\theta, \phi). \quad (2.66)$$

The Born-Oppenheimer approximation states that the electrons move on a much faster timescale than the nuclei, and hence have a higher energy (by about a factor of 100) than the nuclear motional energy.

Due to this difference in timescale, the nuclei move in the electrostatic potential generated by the electrons, which can be approximated to be a Morse potential. This means that the nuclei vibrate as an anharmonic oscillator, with some equilibrium distance R_{AB}^0 . The vibrational motion is again higher (by about a factor of 100) than the rotational energy, which comes from the tumbling of the two nuclei. The total energy is

$$E_{q,v,R} = E_e(q) + E_{\text{vib}}(v) + E_{\text{rot}}(R). \quad (2.67)$$

2.3.2 Transitions

We will now state with brief justification the selection rules describing the allowed transitions between the various states of the molecule [110]. We will label the original state in the transition $|g\rangle = |q, v, R, m_R\rangle$ and the final state $|e\rangle = |q', v', R', m'_R\rangle$. It is useful to remember that the following results are found by considering the intensity of the transition. This, as we saw above when discussing the Rabi frequency, is proportional to $|d_{ge}|^2$, where

$$d_{ge} = \langle g | \mathbf{d} \cdot \boldsymbol{\epsilon} | e \rangle \quad (2.68)$$

is the matrix element of the transition, representing a coupling between the molecular dipole and the light. Again we have \mathbf{d} as the dipole moment operator, and $\boldsymbol{\epsilon}$ as the unit vector representing the polarisation of the light. This dipole moment operator is the familiar one from atomic physics, and is the same regardless of the molecule's orientation.

Since we will typically consider cases with linear or circular polarisation, it is convenient to take $\boldsymbol{\epsilon}$ to be represented in the spherical basis. To evaluate the above integral we therefore express the dipole moment in this rotated frame by means of a rotation operator. This process is fully described in Ref. [110]. The result allows us to separate to good approximation the molecular transitions due to the changing rotational, vibrational and electronic states.

Pure rotational transitions

In a pure rotational transition, the electronic and vibrational states are unchanged ($q' = q$ and $v' = v$). Such transitions are permitted only when $\Delta R = R' - R = \pm 1$. The selection rule for m_R is dependent on the polarisation of the light. For linearly polarised light $\Delta m_R = m'_R - m_R = 0$, whereas for circularly polarised light $\Delta m_R = \pm 1$ for σ^\pm polarised light. The molecule tumbles with a rotation vector perpendicular to the internuclear axis, any rotation around the internuclear axis is symmetrically invariant. The intensity of rotational transitions is proportional to the square of the molecular frame dipole moment.

Vibrational transitions

In the case where there is still no change in electronic state ($q' = q$) we have the same selection rules for any change in the rotational quantum numbers. It can be shown that when the states are well approximated by a quantum harmonic oscillator (which occurs for sufficiently small v so that we can ignore the anharmonicity), the additional selection rule for the vibrational transition is $\Delta v = v' - v = \pm 1$. Of course, $\Delta v = 0$ is allowed, but then this reduces to the above case of a pure

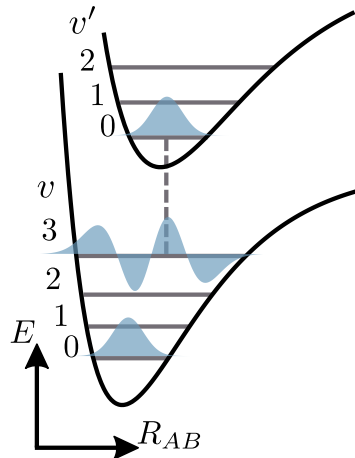


Figure 2.10: A cartoon depiction of a transition between electronic states. Various vibrational wavefunctions (blue) are shown for two electronic potentials. The $0 \rightarrow 0$ transition is weak, since there is small overlap between the vibrational wavefunctions, but the $0 \rightarrow 4$ transition (dashed line) is stronger.

rotational transition.

Changing the electronic state

When the electronic state changes the analysis is more complicated, and there are no consistent selection rules for the change in the vibrational state. This can be explained when we recall that the matrix element d_{ge} is an integral over the state's wavefunction $\psi = R_{AB}^{-1}\psi_e f_v(R_{AB})Y_{R,m_R}$. When the electronic states are the same, the electronic contribution becomes a factor of one and the vibrational states are all states from the same anharmonic oscillator, as can be seen in Fig. 2.10. In this case we can derive the above selection rules.

Now that $q \neq q'$, the vibrational states are not states of the same potential, and so the overlap integral of the wave functions must be computed numerically. The vibrational component of this integral is called the Franck-Condon factor, and is written as

$$q_{v',v} = \left| \int f_{v'}^*(R_{AB})f_v(R_{AB})dR_{AB} \right|^2. \quad (2.69)$$

The rotational state can change by the same selection rules as before, except in the case that the rotational angular momentum is coupled to the angular momentum of the electrons. In this case we can have J as the good quantum number, with a selection rule $\Delta J = 0, \pm 1$.

Parity

Since \mathbf{d} is anti-symmetric under parity inversion, d_{ge} will be zero unless the parity of the wavefunction changes during the transition. This does not apply to homonuclear

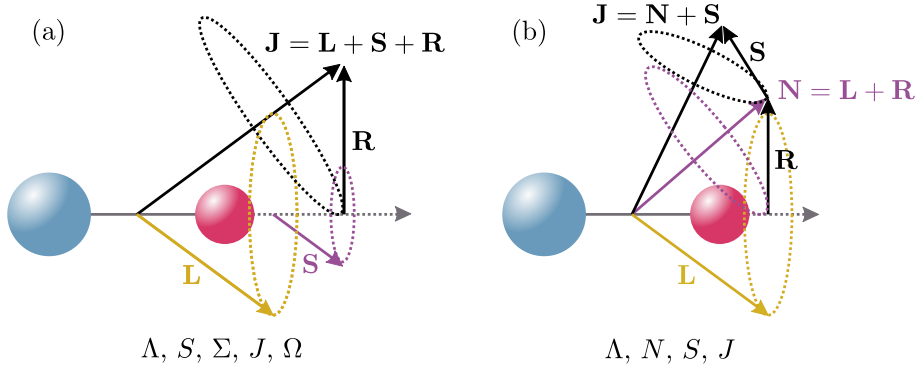


Figure 2.11: Coupling schemes in Hund’s (a) and (b) cases. Arrows are angular momenta. Dashed circles indicate precession of the angular momenta about various axes. See main text for detailed description. This figure is adapted from Ref. [110].

molecules.

2.3.3 Good quantum numbers

We will now briefly review the quantum numbers that we have introduced to describe the molecule state. First note that the quantum number for the electronic level is not really a quantum number at all. It obfuscates the true quantum numbers, which come from the angular momentum operators for the electrons. We will describe the good quantum numbers for two of Hund’s cases [110], which differ depending on how strongly each of the angular momentum operators couple to each other. They are pictured in Fig. 2.11.

In the first case (a), the electron orbital angular momentum \mathbf{L} is strongly coupled to the molecular axis by the electrostatic force, and the spin angular momentum \mathbf{S} couples strongly to \mathbf{L} by spin-orbit coupling. Hence, these momenta both precess around the molecular axis. The good quantum numbers associated with these operators are their projections onto the axis which we label Λ and Σ respectively, as well as S . L is not a good quantum number since it couples very strongly to the axis and so precesses rapidly around it. The rotation operator \mathbf{R} coupling is much weaker, and hence can be approximated to couple to the projection of $\mathbf{L} + \mathbf{S}$ onto the axis. We label this projection $\mathbf{\Omega} = \Omega \hat{\mathbf{e}}$ where $\hat{\mathbf{e}}$ is the unit vector along the internuclear axis, and $\Omega = \Lambda + \Sigma$. The total angular momentum is $\mathbf{J} = \mathbf{L} + \mathbf{S} + \mathbf{R}$. Again, due to the rapid precession of \mathbf{L} and \mathbf{S} , we show this in the figure as a precession of $\mathbf{\Omega}$ and \mathbf{R} around \mathbf{J} . Note that $\mathbf{\Omega}$ is not truly an operator, and is only useful for illustrative purposes.

In the second case of interest (b), \mathbf{L} is strongly coupled to the axis as before, and its projection onto the axis is quantum Λ . L is not a good number for the same reason as before. \mathbf{R} has the next strongest coupling, so we define a new operator $\mathbf{N} = \mathbf{L} + \mathbf{R}$, which for illustrative purposes we show in the figure as $\Lambda \hat{\mathbf{e}} + \mathbf{R}$. Finally

\mathbf{N} and \mathbf{S} add together to form a new total angular momentum $\mathbf{J} = \mathbf{N} + \mathbf{S}$. If $L = 0$ then the state will belong to this coupling scheme. The good quantum numbers for both cases are summarised in the figure.

We label the electronic states by spectroscopic notation taking the form

$$(\text{Unique letter})^{2S+1} |\Lambda|_{|\Omega|}^{\pm},$$

where the unique letter is always X for the ground state, and for the excited states are incrementing letters of the alphabet, starting with A for the first excited state. Λ is not represented by its numerical value, but by the Greek characters Σ , Π , Δ , etc. in analogy with the notation for the orbital states in atoms. The superscript \pm represents the is only used for Σ states, and is defined by the change to the wavefunction on reflection through a plane containing the nuclear axis. When Ω is redundant it can be omitted.

Up to this point we have mainly denoted the wavefunctions as functions, but we will soon find it useful to write the states using braket notation. We will not denote electronic states, this way, but will describe the other quantum numbers. For example, we may write for a Hund (b) case state $|N, S, J, \Lambda\rangle$. However, for an electronic state where $L = 0$, we could express this in an equivalent manner such as $|N, m_N\rangle |S, m_S\rangle$. The quantum number that the ket refers to is implicit by its contents.

2.3.4 Hyperfine structure

The rotational states can be further split into hyperfine states by the angular momentum contribution of the nuclear spin, which has operator \mathbf{I} . The new total angular momentum is $\mathbf{F} = \mathbf{J} + \mathbf{I}$. These states will be important later, since the m_F substates will be used as weak-field seekers for magnetic trapping.

2.3.5 Cooling and trapping molecules

Up to this point we have discussed only the theoretical descriptions of cooling for two-level systems. Although useful, and good descriptions of atomic systems, schemes for cooling and trapping molecules are somewhat more involved. They will be described in greater detail in the context of the CaF experiment in the next chapter, but here I outline the key differences from the two-level systems discussed in section 2.1.

Vibrational repumping: Consider a three-level system, with two ground states $|g_0\rangle$ and $|g_1\rangle$ and excited state $|e\rangle$. If we implement a two-level cooling scheme between $|g_0\rangle$ and $|e\rangle$ then this may well reduce the particle's temperature. However

if the particle can decay from $|e\rangle$ into $|g_1\rangle$, then this particle can become dark to the cooling laser. This can occur for diatomic molecules, for example if the molecule decays from the excited electronic state into a ground electronic state with higher vibrational energy. In such cases it is necessary to introduce additional lasers which will repump these dark states, and ensure that the particle is not lost from the cooling cycle.

Rotational branching: Similar decays into dark states can occur by rotational branching. One way to avoid this is to drive cooling transitions on states with rotational quantum numbers $N = 1 \rightarrow N' = 0$. Then by the selection rules given in section 2.3.2 ($\Delta R = \pm 1$ and parity), it is not possible for a particle in the excited state to decay into states with other values of R . This is explained further in Ref. [1].

Destabilising dark states: We will see in section 3.1.4 that the complex structure of the molecule means that a type-II MOT is required for trapping. This will provide weaker confinement than the type-I MOT described above, but is required in order to address ground states that would otherwise be dark to the cooling light.

Chapter 3

Overview of the experiment

The design of the CaF chip experiment was motivated by three main factors: the need to integrate with the existing experiment, the core proposal of confining molecules close to a microwave guide, and the practicalities of fabricating the chip. In this chapter I will describe how the first two factors informed the design choices, with changes due to fabrication discussed in chapter 5. The design will be further justified by simulation in chapter 4. We begin with a discussion of the existing experiment, which will be used to create the ultracold CaF for loading onto the chip. I will then give an overview and motivation of the design of the chip experiment.

3.1 Existing CaF experiment

In this section I will present a summary of the process used to produce ultracold CaF molecules in a magnetic trap, which we intend to load onto the chip trap. We will consider the various stages of the process, which are presented in Fig. 3.1. First a beam of CaF molecules is created using a buffer gas source [76]. A fraction of the molecules in the beam are slowed to below the capture velocity of the MOT by radiation pressure from counter-propagating resonant light [77]. We can also apply separate light in the transverse direction to improve collimation of the beam during its flight. The molecules are captured in a MOT [79] and cooled in optical molasses [83] before being optically pumped into a weak field seeking state [85]. This allows for magnetic trapping and transport of the molecules. The experiment is conducted under ultra-high vacuum (UHV, $P < 1 \times 10^{-9}$ mbar) conditions to limit background induced loss. Only the source chamber operates at a higher pressure, but the molecule beam quickly exits this chamber into the low pressure region.

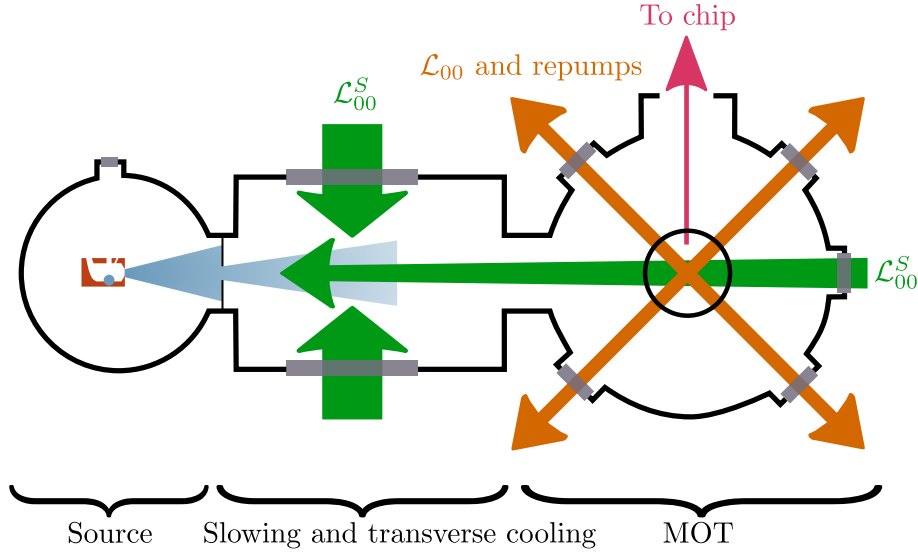


Figure 3.1: A schematic of the CaF source, slowing region and MOT chamber. CaF molecules (blue) are produced by the buffer gas cell, and are slowed by longitudinal slowing and transverse cooling light (green, \mathcal{L}_{00}^S). The molecules are then captured in a MOT (MOT light \mathcal{L}_{00} and repumps combined are shown here in orange) where they can be further cooled and transferred to a magnetic trap. The molecules can then be transported out of the chamber by the MTT in the direction of the pink arrow. A detailed view of the source is shown in Fig. 3.3. This figure is based on one in Ref. [83].

3.1.1 CaF energy structure and constants

The energy structure of CaF is depicted in Fig. 3.2. Here we show only the levels that are pertinent to this thesis, those being the X, A and B electronic levels up to vibrational level $v = 3, 2$ and 0 respectively. The relevant Hund's cases are (b), (a) and (b) respectively. For the X state, we will discuss $N = 0\text{--}2$ but for clarity $N = 2$ is not included in this figure. Figure 3.2 and Table 3.1 also label the various lasers that are used to address the CaF transitions. We denote these $\mathcal{L}_{vv'}$ where v (v') is the lower (excited) vibrational level that the laser addresses. The superscript S is used to distinguish the $X \rightarrow B$ transition since it is used for the slowing light.

The permitted decay paths are shown by the dashed lines, along with their

Symbol	Ground state	Excited state	Wavelength (nm)
\mathcal{L}_{00}	$X(v = 0)$	$A(v = 0)$	606.3
\mathcal{L}_{00}^S	$X(v = 0)$	$B(v = 0)$	531.0
\mathcal{L}_{01}	$X(v = 0)$	$A(v = 1)$	628.6
\mathcal{L}_{12}	$X(v = 1)$	$A(v = 2)$	628.1
\mathcal{L}_{23}	$X(v = 2)$	$A(v = 3)$	628.7
\mathcal{L}_{10}	$X(v = 1)$	$A(v = 0)$	585.4

Table 3.1: The various lasers used in this thesis. The laser \mathcal{L}_{10} is included for completion, and will be explained in chapter 6.

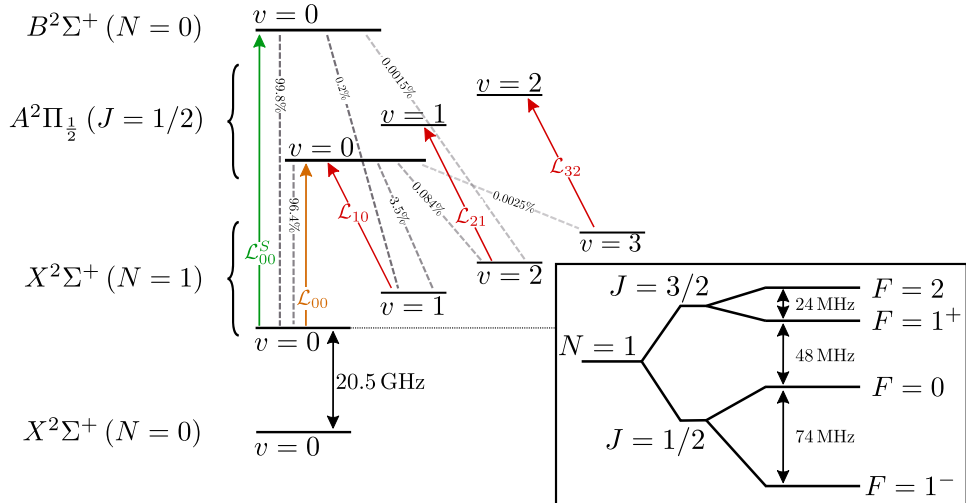


Figure 3.2: The energy levels of CaF are shown, along with the lasers that will be used to address the various transitions (further information is found in Table 3.1). The branching ratios for the allowed decays are shown with dashed lines. Note that the $X(N = 0)$ level is included, but for simplicity the $X(N = 2)$ level is omitted. The box shows the hyperfine states of $X(N = 1, v = 0)$, how these arise from the N and J angular momenta is described in the main text. This figure is adapted from Ref. [79].

branching ratios. One of the reasons CaF is chosen for study over other molecules is its highly diagonal Franck-Condon factors, so that most decays occur with $v' = v$. However, as we discussed in section 2.3.5, for large numbers of scattered photons we must employ the various repump lasers to avoid pumping into states that are dark to the cooling light. This will be discussed further when describing slowing of the beam and the MOT.

Hyperfine splitting occurs in CaF due to the spin-half contribution of the fluorine atom. This is not resolved in the A state, but it accounts for the hyperfine splitting of the X state as is shown in the box of Fig. 3.2. It is worth explaining why we have the four F states $F = 2, 1^+, 0, 1^-$. These arise due to the combination of the hyperfine interaction and a spin rotation interaction of the form $\mathbf{S} \cdot \mathbf{N}$. Since we are in Hund's (b) case, the $N = 1$ state is split into angular momenta states $\mathbf{J} = \mathbf{N} + \mathbf{S}$. Here $S = 1/2$, so the possible values of J are $N + 1/2$ and $N - 1/2$ (with the exception of $N = 0$ where we have only $J = 1/2$). For $N = 1$, we have $J = 3/2$ and $J = 1/2$. Each of these is again split by the hyperfine interaction into $\mathbf{F} = \mathbf{J} + \mathbf{I}$, with $I = 1/2$. This gives us the allowed values $F = 2, 1^+, 0, 1^-$.

In the B state, the $F = 0$ and $F = 1$ states are split by 20 MHz, which can usually be neglected for the purposes of our discussion. A full description of the CaF energy structure and various constants can be found in Ref. [86], those that are most useful are presented in Table 3.2.

Constant	Symbol	Value
Mass	m	59 u
Electric dipole moment (X state)	μ_e	-3.08 D
Magnetic dipole moment	$g_F \mu_B m_F$	

Table 3.2: Various constants for CaF taken from Ref. [86]. Note that the magnetic dipole moment is given in terms of the g-Factor g_F and the quantum number m_F , which are state dependent, as well as the Bohr magneton $\mu_B = 9.274 \text{ JT}^{-1}$.

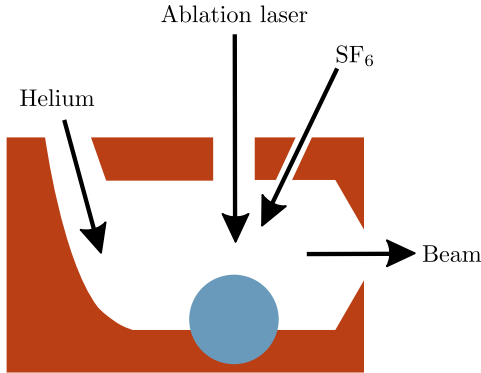


Figure 3.3: The buffer gas cell. Helium and SF_6 flow into the cell. Ca atoms are ablated from a target (shown in blue) by a Nd:YAG laser. CaF molecules are formed which thermalise with the He and a molecule beam exits from the aperture.

3.1.2 Buffer gas source

We begin all our experiments by creating a pulsed beam of CaF molecules using a buffer gas source. This is pictured in Fig. 3.3 and consists of a copper cell which is cryogenically cooled to 4 K. Helium gas, also cooled to 4 K, and SF_6 gas near room temperature, flow through the cell. A Ca target (shown in blue) is ablated by a pulsed Nd:YAG laser. The Ca reacts with the SF_6 to produce CaF, which is then flushed out of the cell by the helium flow.

The cell is designed to optimise the flow of He so as to entrain the CaF and guide it to the exit aperture without the creation of vortices, where the molecules can be trapped [76]. For this reason He enters from towards the rear of the cell at 4 K and flows towards the exit aperture. The Ca target is mounted on a rotating stage, so that when one region is depleted another can be targeted.

In order to prevent excess helium entering the slowing and MOT chambers, a second aperture is positioned between the source and slowing chambers. Differential pumping ensures that the slowing chamber remains at UHV. A mechanical shutter at this aperture reduces the time that helium is able to leave the source chamber to only the time when there is a pulse of CaF. We also use a copper shield, coated with coconut charcoal and cooled to 4 K as a helium absorber [113]. This is thermally cycled overnight when the source is not in use to avoid saturation. As noted in

Ref. [97], this buffer gas source originally produced up to 5×10^{10} molecules/steradian molecules in $X(N = 1, v = 0)$ per pulse, with a mean velocity of 160 m s^{-1} [76] but its performance has degraded since the original report. As a result we now observe 50%–60% lower MOT population than at the time Ref. [79] was published.

3.1.3 Slowing the beam

The buffer gas source produces a beam of molecules with mean forward velocity 160 m s^{-1} – slower than for example, a supersonic source [114] but they are still far above the capture velocity of our MOT, which is approximately 10 m s^{-1} . The beam’s velocity can be further reduced by radiation pressure due to a counter-propagating beam of \mathcal{L}_{00}^S slowing light. This is chirped to account for the change in Doppler shift of the transition frequency as the molecules slow. The slowing light is also combined with the \mathcal{L}_{10} repump light to avoid pumping into the $X(v = 1)$ state. To again account for Doppler shift during slowing, the repump light is frequency broadened by 300 MHz by a series of three electro-optic modulators.

We apply the light for 6 ms, which slows over approximately 90 cm of travel from the buffer gas cell’s exit aperture. Linear chirps used in previous experiments have been used to slow the molecules for loading into the MOT, as detailed in Ref. [79]. Implementing an exponential chirp originally proposed in Ref. [115] produced a 60%–80% improvement in the number of molecules in the MOT [97].

It is also possible to reduce the transverse velocity of the beam by applying slowing beams in the perpendicular direction close to the source. This is shown for one dimension in the ‘slowing and transverse cooling’ section of Fig. 3.1, however in reality there is a second pair of beams going into and out of the page. For this cooling step we also use the $X \rightarrow B$ transition along with the \mathcal{L}_{10} repump [97].

3.1.4 Capture in a MOT

We aim to capture molecules in a MOT positioned 130 cm from the cell’s exit aperture inside a separate vacuum chamber. The MOT magnetic field is provided by in-vacuum anti-Helmholtz coils and the MOT light is formed from a single beam which is reflected along each axis before being retro-reflected through the entire experiment to provide the restoring beams. We described in section 2.3.5 that laser cooling and trapping of diatomic molecules requires us to address three key differences to atomic systems. The first is the repumping of the vibrational levels. We apply vibrational repumps (\mathcal{L}_{10} , \mathcal{L}_{21} and \mathcal{L}_{32}) along with the main cooling light (\mathcal{L}_{00}). All of these beams must have the r.f. sidebands to address the hyperfine levels of the X state (recall that the hyperfine levels of A are unresolved).

The second nuance is the rotational branching, which we avoid by cooling on the

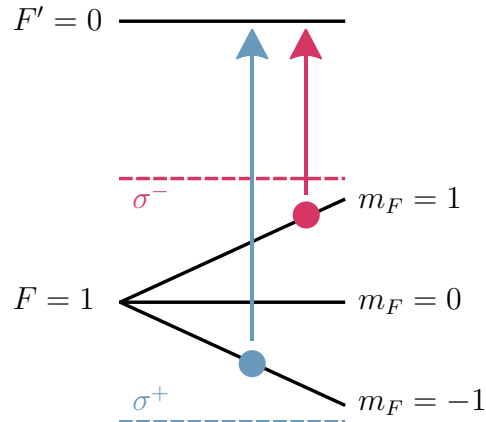


Figure 3.4: A dual frequency scheme for the type-II case $F' = 0$, $F = 1$. The molecules in each state (circles) can be pumped by their corresponding red- (blue-) detuned light. This figure is adapted from one in Ref. [117].

$X(N=1) \rightarrow A(N=0)$ transition. This immediately leads to the third nuance, which is the remixing of resulting dark states. The CaF MOT is a type-II MOT [116], meaning that the angular momentum of the excited state is less than that of the ground state . Unlike a type-I MOT (where $F' > F$), it is possible for a molecule that has been pumped into the excited state to decay into a dark state, or into a state that is anti-trapped by the MOT [1]. To resolve this, we employ a dual-frequency MOT. Figure 3.4 illustrates this MOT scheme for the simplified case of a ground state with $F = 1$ and an excited state with $F' = 0$. When there is no blue-detuned light, any molecule that decays into the $m_F = -1$ state can be lost from the cycle. When blue-detuned light of opposite polarisation is present these molecules can be repumped.

We are typically able to capture on the order of 10^4 molecules from our beam. The MOT population can be estimated by the light-induced fluorescence. The MOT temperature is reduced to its minimum value by lowering the intensity of \mathcal{L}_{00} , since this reduces the effects of Sisyphus heating [83]. We typically observe MOT temperatures below 4 mK. A complete description of the CaF MOT is far beyond the scope of this overview, and has been described in detail elsewhere, for example see Ref. [79]. We will not discuss an important alternative scheme for forming a CaF MOT, the r.f. MOT, a description of which can be found in Ref. [80].

3.1.5 Optical molasses

Sub-Doppler cooling of CaF is achieved with a blue-detuned molasses. In this scheme the MOT coils are switched off, and \mathcal{L}_{00} is now blue-detuned from the transition frequency. This scheme is somewhat complex, so consider again the simplified example of a molecules travelling in one dimension and having an $F = 1$ ground state and $F' = 0$ excited state, as is shown in Fig. 3.5. The counter-propagating beams

establish gradients of both polarisation and intensity. As explained in Ref. [118] we will have bright states that have an a.c. Stark shift, and dark states which do not. The a.c. Stark shift of the bright states depends on polarisation, and so as molecules move through the gradient the bright state energy changes, as is shown in the figure.

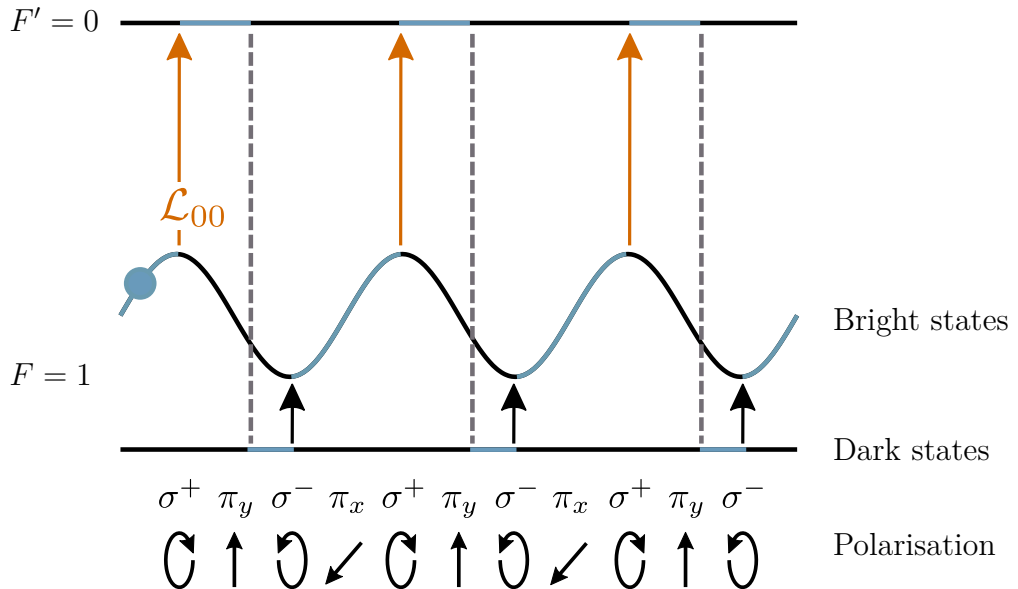


Figure 3.5: Blue-detuned molasses for a type-II system with $F = 1$, $F' = 0$. Here the polarisation gradient across a 1D system (bottom row) causes a change in the coupling strength of bright states. A molecule travelling through the gradient (blue) will be preferentially excited by \mathcal{L}_{00} to the excited state when the coupling is strong. It will decay into the dark states, and adiabatically transfer back to the light states (black arrow) when the coupling is weak. Repeating this process results in a net loss of energy for the molecule. This figure is adapted from Ref. [116].

When a molecule in a bright state moves through the polarisation gradient it can expend energy climbing the potential. It is preferentially pumped into the dark state (via $F = 0$) at the top of the potential because the probability of pumping is proportional to the square of the Rabi frequency, which is greatest at this point. From the dark state, molecules can non-adiabatically transfer back into the dark state at regions where the energy difference is low. The molecule can now repeat this cycle, each time losing energy travelling up the potential. Note that the light must be blue-detuned because in the case of red-detuning the bright states have lower energy than the dark states, and there is a heating rather than a cooling effect [116].

These same principles apply in the three dimensional case, although the polarisation and intensity structure of the light field is more complicated. We must also

consider the numerous energy levels of CaF and the sideband structure required to address the hyperfine state. A full treatment requires solving the optical Bloch equations, which is done in Ref. [116]. In our experiment we apply this technique to produce a CaF cloud of temperature $< 6 \mu\text{K}$ [84].

3.1.6 Magnetic trapping and transport

The molecules can now be transferred into a weak-field seeking state by optical pumping. The weak-field seekers can be confined in a magnetic trap, provided either by the MOT coils, or by the external transport coils (see Fig. 3.1. In the case of the latter, the molecules can then be transferred to the tweezer chamber, or in the future to the chip for loading.

During the molasses there is no magnetic field to lift the degeneracy between the Zeeman states. Therefore after the molasses light is turned off the molecules are distributed between the Zeeman substates of $X(v = 0, N = 1)$. Attempting to magnetically trap at this point would cause a significant loss, so we optically pump into the weak-field seeking state by a procedure originally proposed for SrF in Ref. [119] and described for CaF in Ref. [97].

In this scheme a weak magnetic field (200 mG) is applied across the cloud, and two beams of light are incident on the molecules. Both act on the $X \rightarrow B$ transition, but their frequency components are tuned to be close to the $F = 2$ and $F = 1^-$ hyperfine levels respectively. The $F = 2$ ($F = 1^-$) frequency component propagates parallel (perpendicular) to the magnetic field and its polarisation is chosen to drive σ^+ (π) transitions. This means that the only state dark to the light is the magnetically trappable state $|N = 1, F = 2, m_F = 2\rangle$, which is eventually populated. From here it is possible to transfer to other states by microwave spectroscopy techniques [85]. Various weak-field seeking states of CaF are detailed in Fig. 3.6.

At this stage we also introduce three stretched states in CaF. These states lie in the X electronic level, and are denoted

$$|N\rangle_{\text{str}} = |N, m_N = N\rangle |S, m_S = S\rangle |I, m_I = I\rangle, \quad (3.1)$$

where the degeneracy must be lifted by the application of an external magnetic field, m_X is then the projection of X onto this field's axis. The stretched states are of interest because they are not only weak-field seekers, but the transitions between neighbouring stretched states ($|N\rangle_{\text{str}} \leftrightarrow |N + 1\rangle_{\text{str}}$) are highly insensitive to magnetic fields. Of particular note are, the $|0\rangle_{\text{str}} \leftrightarrow |1\rangle_{\text{str}}$ ($\omega_0/(2\pi) = 20.5 \text{ GHz}$) and $|1\rangle_{\text{str}} \leftrightarrow |2\rangle_{\text{str}}$ ($\omega_0/(2\pi) = 41.1 \text{ GHz}$) transitions observed in Ref. [92], which we will discuss further in chapter 7.

After transferring into the magnetically-trappable states, the molecules can be

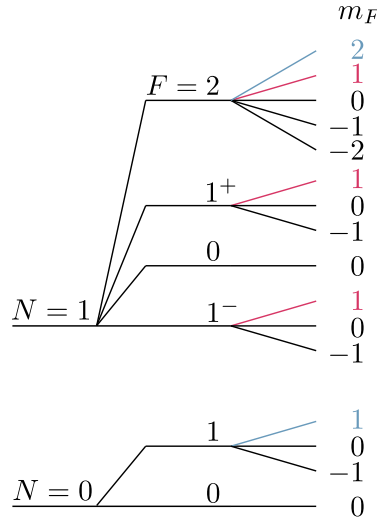


Figure 3.6: Hyperfine structure of CaF ground states. The stretched states are highlighted in blue, and other weak-field seekers are highlighted in pink. Adapted from Ref. [85].

contained in a quadrupole magnetic trap generated by anti-Helmholtz coils inside the vacuum chamber, as also discussed in Ref. [85]. They can then be used for a variety of experiments, including the chip experiment, as we will now discuss.

3.1.7 Other experiments and transport

The CaF MOT is the workhorse of our experiment which, after the further cooling discussed above, can be used to study collisions with Rb atoms (see Refs. [90, 97, 120]) or can be loaded into optical tweezers. Due to the limited optical access available in each chamber it is convenient to perform some experiments in separate chambers to that which contains the initial MOT. Hence other members of CCM have developed a scheme for transporting the molecules from the MOT chamber to a neighbouring chamber by means of a magnetic transport trap (MTT). This second chamber is used for experiments with optical tweezers and so is referred to as the tweezer chamber. The MTT consists of magnetic coils in anti-Helmholtz configuration, situated outside the vacuum chamber (as opposed to trapping with internal coils). These coils are mounted on a transport stage, so that they and hence the field they generate can be translated.

The transportation procedure is depicted in Fig. 3.7. Molecules are initially trapped using internal coils in the MOT chamber. They are then handed over to the MTT by ramping off the current in the internal coils, and ramping on the current in the external coils. The coils are then translated by the stage at speeds sufficiently slow to bring the molecules with them. The ramping process can then be inverted to hand the molecules back over to an internal trap, either to coils in the tweezer chamber, or to a wire trap in a third chamber to be used for the chip (the chip

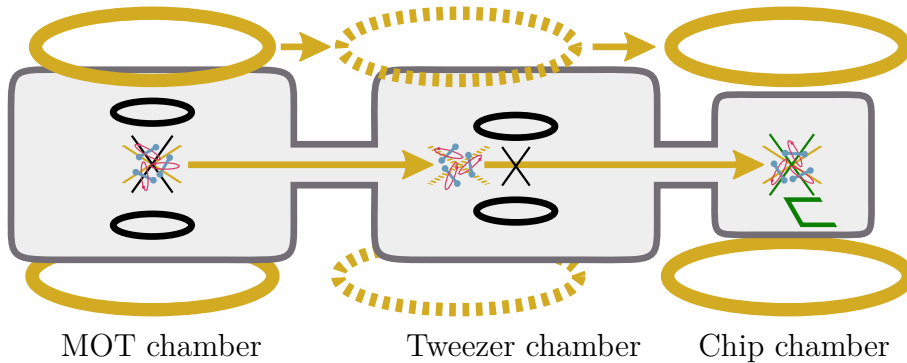


Figure 3.7: Depiction of the MTT scheme. CaF molecules trapped initially in the MOT chamber using internal coils (black, with quadrupole field marked by the black cross) are transferred to the external trapping coils (gold, with field marked by gold cross). The coils can then be translated to transport the molecules to neighbouring chambers. The dashed lines depict transport in progress. They can be loaded back into internal coil traps (such as the black coils in the tweezer chamber) or onto a wire trap (shown in green in the chip chamber), as is shown occurring here.

chamber). This transport of the molecules is similar to that used in Refs. [121, 122] and elsewhere. Details of the handover procedure and simulations thereof will be discussed further in chapter 4. In the next section, we will begin to discuss how the molecule chip can also be incorporated as an additional experiment.

3.2 Design requirements and overview

This section will present the design of the molecule chip experiment, and how it is to be integrated into the existing CaF experiment whilst accounting for fundamental constraints. I will present computer-aided designs of the chip chamber, which were created by Kyle Jarvis in CCM, as well as my designs for the chip itself, and a PCB for power delivery.

As discussed in chapter 1 the aim of this project is ultimately to trap molecules in close proximity to microwave resonators so that we can perform coherent control of quantum states on the rotational transitions in the molecules. Following the proposal by Ref. [2], this can be achieved in a chip architecture, with the molecule trapped as close to the resonator as possible. The ultimate limiting factor will come from the Van der Waals force¹, where the fluctuating electric dipole moment of the molecule results in attraction between the molecule and the chip surface [108]. The associated energy shift is

$$V_{\text{vdW}}(z) \approx \frac{\mu_e^2}{4\pi\epsilon_0 z^3}. \quad (3.2)$$

¹One might wonder about the effect of an increase in black body radiation near to the chip. It transpires that the excitation rate for CaF by black body radiation remains mostly constant as the molecule approaches a surface [123].

We require that the gradient,

$$V'_{\text{vdW}}(z) = \frac{3\mu_e^2}{4\pi\epsilon_0 z^4}, \quad (3.3)$$

to be small compared to the force from a magnetic trap, which can be calculated for a representative dimple trap using eqn (2.34). Taking the operating current to be $I = 1 \text{ mA}$. The condition $V'_{\text{vdW}}(z) \ll \mu_B B'$ can be written as

$$z \gg \sqrt{\frac{3\mu_e c^2}{2\mu_B I}}, \quad (3.4)$$

limiting the height by $z \gg 10^{-7} \text{ m}$. We therefore take the minimum possible trap height to be $10 \mu\text{m}$. The trapping wires must be on a smaller scale than this so that the trapping potential is sufficiently localised. Features of such a size can be easily created by standard photolithography techniques.

Additionally, we aim to integrate the chip trap into our existing CaF experiment. This can be done by the addition of a new chamber to our setup, shown in Fig. 3.8. The chip chamber will be positioned along the existing MTT axis, allowing extension of the transport system and the delivery of molecules to this chamber. CaF molecules can then be transferred onto the chip trap via the process also outlined in Fig. 3.8.

At this point, we note that the long-lived stretched states discussed in section 3.1 are promising candidates for the qubit states in a molecule chip. For this reason it was decided that using magnetic traps, such as those described in section 2.2 would be preferable to the electrostatic traps suggested in Ref. [2]. We are now faced with the question of how exactly we can load molecules from the MTT into the microscopic chip trap.

Fortunately this problem has previously been addressed for atom chips. We discussed already in chapter 1 that atoms can be guided on chips by changing of trapping currents. We also discussed the transfer of atoms between on-chip magnetic traps. For the problem of loading from a macroscopic trap, we can turn to Ref. [35], where transfer from a transport trap to a microtrap is made easier by the use of an intermediary macroscopic trap that is well-aligned with the microtrap. We propose a similar solution: embedding a macroscopic U-wire beneath our chip trap which is aligned to the chip and makes a large target for loading from the MTT.

To ensure that molecules are then loaded into the smallest trap efficiently, we again follow in the footsteps of atom chips, and have designed a series of traps of decreasing size [25]. For magnetic traps, the width of the wires should decrease, so that the molecules remain localised around the trap centre throughout loading. Each wire trap will begin trapping at one height before the bias field is increased to bring the trap centre closer to the surface (as per eqn (2.30)). We choose the wires

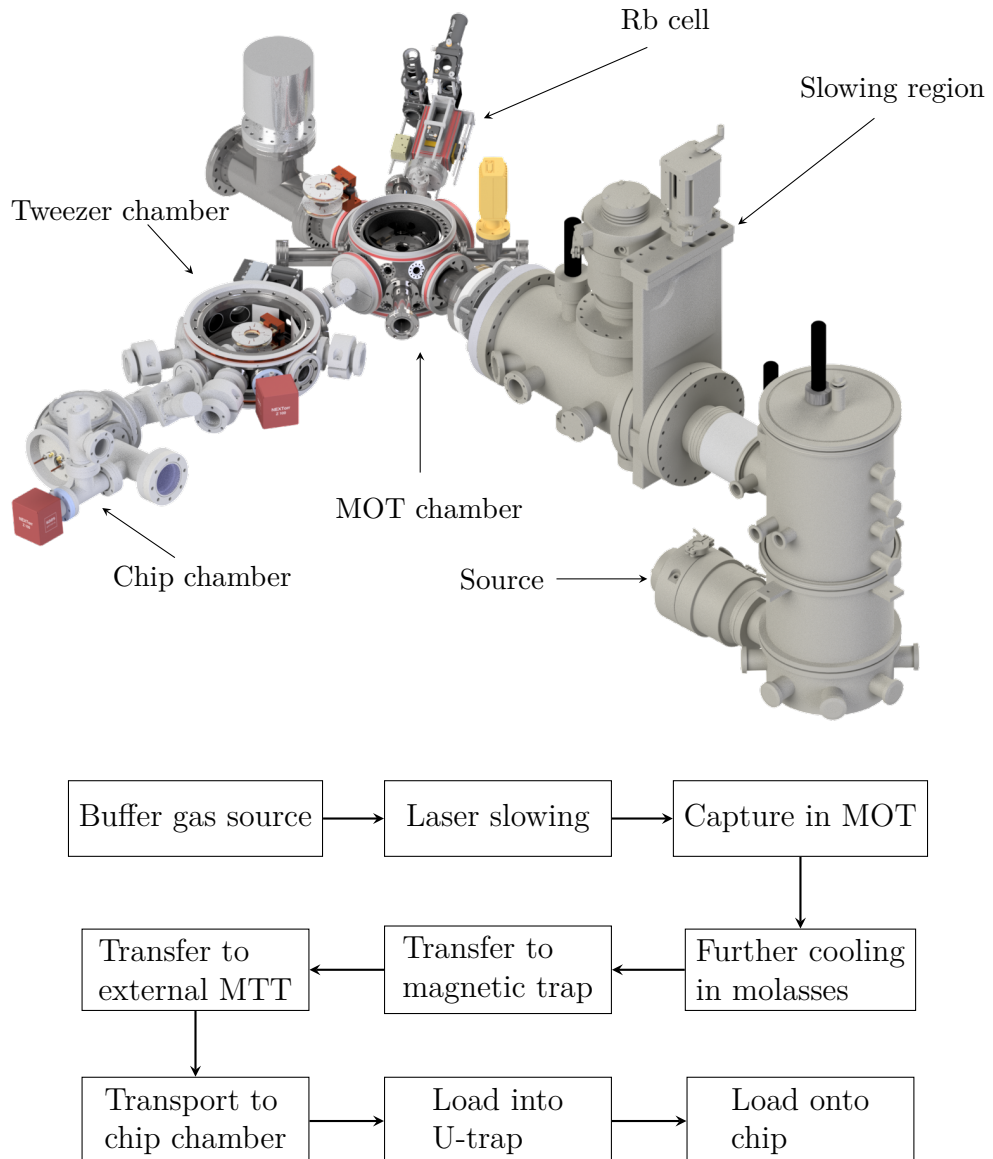


Figure 3.8: The CaF experiment is shown along with the planned additional chip chamber. Not shown: external transport coils and transverse cooling region. The flowchart outlines the various stages of the chip experiment.

Name	Axis length (mm)	Width (μm)	I_{\max}	Trap height (μm)
U	16	N/A	100	3000
Z0	12	200	60	3000 → 1000
Z1	6	20	6	1000 → 100
Z2	2	9	2.7	100 → 10

Table 3.3: Details on the wire dimensions, maximum current, and desired trapping heights. The wire design is shown in Fig. 3.9. Note that the U-wire current is limited by vacuum feedthroughs and not by the maximum current calculated by the wire dimensions. The maximum currents have been designed for use at only 50% of their potential maximum (I_{\max}).

to be Z-traps so as to avoid any losses by spin-flips, and so we label the stages ZX_i for initial (higher) traps and ZX_f for the final (lower) trap, with ZX corresponding to the wire labels in Table 3.3. Bias fields for all traps are to be provided by external Helmholtz coils.

Each Z-wire should be sufficiently large to maintain the currents required to form a trap at height z below the trap, whilst having a width and height $w, h \ll z$ so that the current is highly localised compared to the cloud size. In the case of the first Z-wire, the molecules are still 3 mm away from the trapping wire. If we demand a trap depth of $k_B \times 1 \text{ mK}$, then we require a trapping current of 30 A to form a trap of this depth. We will discuss in chapter 5 that the maximum wire height that can reliably be fabricated is 5 μm , and we expect that the wires will be able to carry a maximum current density of $6 \times 10^{10} \text{ A m}^{-2}$, as was found for a similar chip design in Ref. [46]. Consequently, the required width of the first Z-wire is $w = 200 \mu\text{m}$. The currents and widths of other wires are calculated similarly. All wires have been designed to carry twice the current that is required in the loading scheme, so that there is sufficient headroom for further experiments, and to reduce risk of accidental damage to the chip during normal operation. The axial length of the wires also decreases to gradually reduce the size of the trapped cloud in the x direction.

The final chip design was informed both by the requirements here, the simulations presented in chapter 4 and the restrictions due to the fabrication process, which will be discussed in chapter 5. We tried various different designs, but the final one that was chosen is shown in Fig. 3.9. It features the wires as stipulated in Table 3.3, fanouts for connection of macroscopic current delivery wires, and various other features that will also be explained in chapter 5.

Notice that this design is a single-layer design, with the wires intersecting. A system has been devised to ensure that the desired currents are achieved in each wire segment, and is described in section 6.3.4. Further, this initial design does not incorporate microwave guides. These are to be installed on a second level, separated

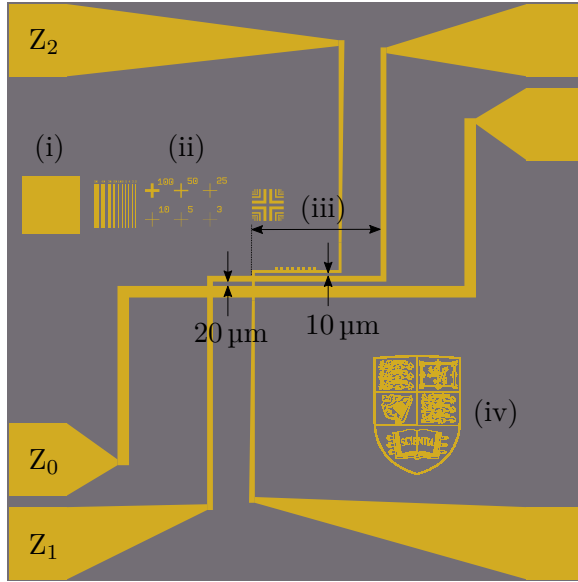


Figure 3.9: A schematic of the single-layer chip features, with the scaling exaggerated for visibility. The three overlapping Z-wires are shown and labeled. The gaps between the wires are highlighted. Toward the left (i) is the electroplating connection pad and various features used for characterisation (ii). On Z₂ it is possible to see several small pads used as anchors, to secure the thin wire to the substrate. The axis of the Z₁ wire is labeled for reference (iii) and the other wires are similar. All of the above features will be discussed further in chapter 5. The crest of Imperial College London (iv) is also included.

from the trapping wires by a thin insulating layer, on which we can fabricate coplanar waveguides [124]. This stage of the project has not yet been reached, but the planned fabrication procedure for microwave guides is discussed in section 5.10 and their operation is discussed in chapters 7 and 8.

To facilitate all of this, the chip is mounted on a flange with supporting infrastructure, as detailed in Fig. 3.10. This chip flange assembly is equipped with a large copper heat sink, a large U-wire to form the macroscopic alignment trap and a subchip for current and microwave delivery (detailed in Fig. 3.11). Connection is possible via soldering or wire bonding, as will be discussed in chapter 5. The chip is mounted into a recess in the subchip so that it is flush with the surface. It is mounted facing downwards so that molecules can be dropped for imaging as they fall.

The flange itself is fitted with two high-current (100 A) feedthroughs, a 16-pin feedthrough rated for 3 A currents, and microwave feedthroughs. All access to the chip is therefore through this one flange, allowing for easy access and assembly. It will be housed in the chip chamber, positioned as shown in Fig. 3.7 and Fig. 3.8. The chip chamber will be arranged so that molecules can be brought in along the transport axis (shown by the arrow in the Fig. 3.10 (b)) and positioned below the surface of the chip. This arrangement will be explained in further detail in chapter 6.

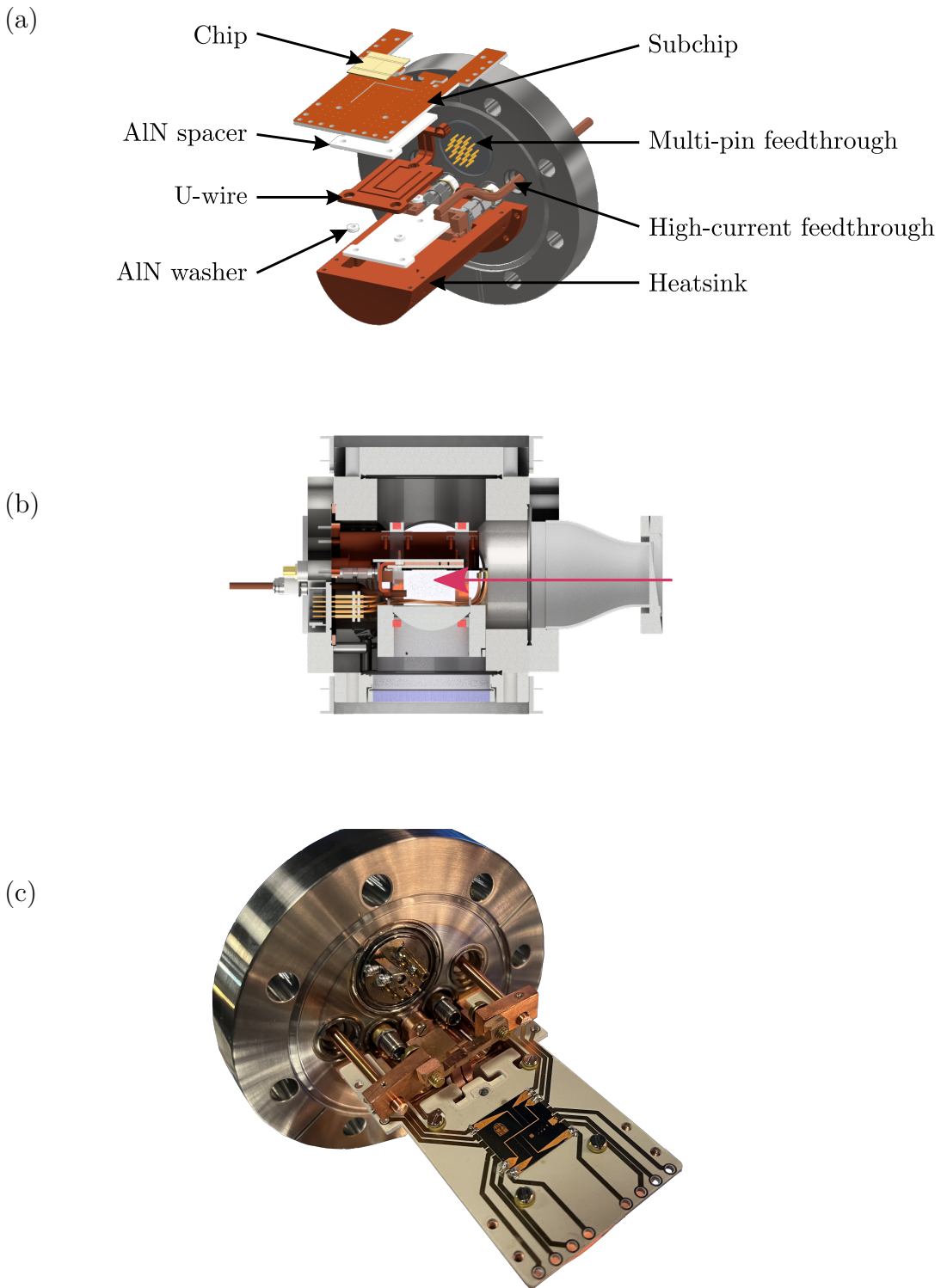


Figure 3.10: The chip experiment is shown in detail. In (a) we show an exploded view of the chip flange assembly, with the various components labeled. A cross section of the chip chamber is shown in (b). The arrow shows how molecules will enter the chamber, brought in by the MTT. In (c) we have the chip assembly fully constructed, with a view of the aluminium-core PCB (subchip) for current delivery. The microwave feedthroughs remain disconnected.

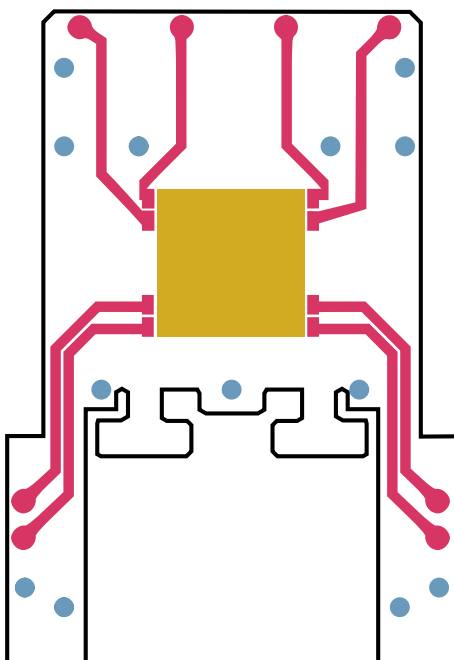


Figure 3.11: The subchip layout for power delivery to the chip. Traces are shown in pink (the number of traces used depends on the number of wires in the chip design and can vary between subchips), and mounting holes in blue. The chip is situated in a recessed alcove marked by the gold square. Connections can be made to the PCB by mounting screws at the end of the traces. Connection from the PCB to the chip can be made by soldering or wire bonding, as will be discussed in chapter 5.

Chapter 4

Simulating the trap

In this chapter I present simulations of the molecules in the trap. In particular I show that we have developed a procedure for loading molecules into the chip trap. This was done using the custom USP python package, which I developed for this project. The codebase can be found in Ref. [125], and contains tools for simulating particle trajectories in a magnetic field, and also for calculating the fields generated by wires typically used in chip trap experiments. The code can also be used for other field geometries, such as common quadrupole traps, or those used in Zeeman guiding experiments [88].

4.1 Motion of molecules in a trap

We can assume that the motion of the molecules in the trap is classical. They move in the potential $V(t, \mathbf{q}) = \mu B(t, \mathbf{q})$, where $\mu \approx \mu_B$ is the magnetic dipole moment of the molecule in the $|N = 0, F = 1, m_F = 1\rangle$ state. The motion of any one particle is described by Hamilton's equations, [126]

$$\dot{\mathbf{q}} = \frac{\partial H}{\partial \mathbf{p}} \quad \dot{\mathbf{p}} = -\frac{\partial H}{\partial \mathbf{q}}, \quad (4.1)$$

where H is the classical Hamiltonian of the system

$$H(t, \mathbf{q}, \mathbf{p}) = \frac{\mathbf{p}^2}{2m} + V(t, \mathbf{q}). \quad (4.2)$$

For now we neglect the time dependence of the potential, so that $V(t, \mathbf{q}) = V(\mathbf{q})$.

Solving Hamilton's equations tells us the position and momentum of a single particle. Taken together these two vectors describe a point in a six dimensional phase-space of position and momentum. For an ensemble of particles we often consider the envelope of the region they occupy, calling this space the phase-space volume of the ensemble. This is a powerful tool, since calculating the trajectory of particles on

the boundary of this region is often sufficient to describe the behaviour of the whole ensemble. This technique is commonly used in particle trapping, and especially when considering the behaviour of beams of particles, where a four-dimensional phase-space is used [126, 127].

It is helpful for us to write the phase-space volume V in terms of the spatial volume occupied by the ensemble (V_{space}) and its temperature. This is possible because in thermal equilibrium the momentum distribution is

$$f(p) = \frac{1}{(2\pi m k_B T)^{\frac{3}{2}}} \exp\left(-\frac{p^2}{2m k_B T}\right) \quad (4.3)$$

whose maximum value

$$\left(\frac{\lambda_{\text{dB}}(T)}{h}\right)^3 = \frac{1}{(2\pi m k_B T)^{\frac{3}{2}}} \quad (4.4)$$

depends only on the temperature T . Here we have introduced the de Broglie wavelength $\lambda_{\text{dB}}(T)$, the length-scale for a monatomic gas of temperature T . [128]

The unitless phase-space volume is

$$V = V_{\text{space}} \lambda_{\text{dB}}^{-3}(T). \quad (4.5)$$

It is also useful to define a unitless phase-space density [129]

$$\rho = \frac{N}{V} = \frac{N \lambda_{\text{dB}}(T)^3}{V_{\text{space}}}. \quad (4.6)$$

For a given cloud with uniform phase-space density ρ , trap with volume V_{trap} and depth T_{depth} , the maximum possible number of particles that can be trapped is $\rho V_{\text{trap}} / \lambda_{\text{dB, trap}}^3$, where $\lambda_{\text{dB, trap}} = \lambda_{\text{dB}}(T_{\text{depth}})$.

A second powerful tool for determining the motion of the particles is Liouville's theorem [127, 130] which states that the phase-space volume is a conserved quantity, as long as the trapping potential is conservative. This means that the phase-space density of a trapped molecular cloud cannot be increased without application of some velocity-dependent force, such as an optical molasses [4]. The impact of this for the chip is that the phase-space density of the cloud at the point of loading onto the chip determines the maximum number of molecules that can be trapped in the final trap.

If we do not introduce any further cooling steps, then the number of molecules we are able to contain in the final trap will be

$$N_{\text{final}} = \frac{\rho_{\text{CaF}} V_{\text{trap}}}{\lambda_{\text{dB, trap}}^3} = \frac{\rho_{\text{CaF}} V_{\text{trap}} (2\pi m k_B T_{\text{trap}})^{\frac{3}{2}}}{h^3}. \quad (4.7)$$

Phase space densities of $\rho_{\text{CaF}} \sim 10^{-8}$ can be achieved by laser cooling¹ [131]. The smallest trap will have volume $V_{\text{trap}} \sim (10 \mu\text{m})^2 \times 1 \text{ mm}$ and depth $T_{\text{trap}} = 4 \text{ mK}$, which can be calculated by equation 2.32. We therefore expect that as many as 10^5 molecules can be trapped.

In the current experiment we are not able to implement a dipole trap, although this technique is being developed within our group. Using sub-Doppler cooling techniques, the maximum phase space density that we can achieve is much lower, at $\rho_{\text{CaF}} = 3 \times 10^{-12}$ meaning the number of molecules trapped will be of order one. Clearly we require the high phase-space density cloud to efficiently load the final trap, however it will still be possible to load molecules into the outer traps with the techniques available to us. By carefully designing a loading scheme, we hope to be able to maximise the number of molecules that will be accepted in the final trap.

4.1.1 Phase-space acceptance

For a particle to be trapped it must occupy some spatial region that is within the trapping potential and it must not have sufficient energy to escape from said potential. In other words, the total energy of the particle, given by the classical Hamiltonian $H(\mathbf{q}, \mathbf{p})$, must be less than the trap depth $k_B T_{\text{depth}}$. This relation defines a region of phase-space that we call the acceptance. Any particles within this region will not have sufficient energy to escape, and so will remain trapped under classical motion unless externally influenced (ignoring for example any collisions, decays, Majorana losses, etc.) [126].

As an example consider the one-dimensional case of a harmonic trap found in Ref. [64]

$$V(z) = \begin{cases} 0 & |z| > l \\ \frac{1}{2}m\omega^2 z^2 & |z| \leq l. \end{cases} \quad (4.8)$$

Here, any particle which starts with a position $-l \leq z \leq l$ will be trapped, so long as its velocity is not sufficiently large that it will escape into the $|z| > l$ region. To reach $z = l$ from an initial position z_0 , the particle must have kinetic energy of at least

$$\frac{1}{2}mv_0^2 = \frac{1}{2}m\omega^2(l^2 - z_0^2), \quad (4.9)$$

where v_0 is the initial velocity. It is now clear that a particle is trapped on the condition that

$$(v_0/\omega)^2 + z_0^2 < l^2 \quad (4.10)$$

which defines an ellipse in phase-space.

¹Even higher phase-space densities (of the order 10^{-4}) have been achieved using a cross-dipole trap [86], but for now this is beyond the capabilities of our experiment

This trapping condition can be verified by simulation, as is shown in Fig. 4.1 (a) and (d), where the trap has been simulated for $m = 1$, $\omega = 10^3 \text{ rad s}^{-1}$ and $l = 1 \text{ mm}$. We initialise 2000 particles uniformly distributed with $|z_0| < 0.2 \text{ mm}$ and $|v_0| < 1.5 \text{ m s}^{-1}$. Their trajectories are computed for 1.2 ms by the methods described in the next section. The boundary of the acceptance, called the separatrix is shown in black. All particles that are initialised inside the acceptance remain trapped and evolve through time in the usual way for a harmonic potential. Particles initialised outside the acceptance are rejected and lost.

It is also instructive to consider anharmonic potentials, for example

$$V(z) = -V_0 \cos(\omega z) \quad (4.11)$$

which is also presented in Fig. 4.1, using the same parameters as for the previous potential. We again see that particles with sufficiently low energy in the trapping region remain trapped, however in this case the anharmonicity of the trap results in the particle cloud spiralling outwards, undergoing an effective increase in the phase-space density. This means that although the actual phase-space density remains the same, the envelope of the region that they occupy becomes increasingly convoluted. This makes it effectively impossible to contain them in any potential with a volume smaller than that of the trapping potential. This effect is often referred to as filamentation.

Finally, it is useful to consider the phase-space acceptance of a wire trap. For simplicity we begin by considering only the acceptance in the z direction (perpendicular to the chip surface). We calculate the acceptance of a Z-wire with an axis of 20 mm, current of 40 A and a trapping height of 3 mm. The particles are initialised such that they have no motion in the x and y directions, and the trajectories are simulated for 200 ms. Figures 4.1 (c) and (f) show the distribution at the start and end of the simulation. The accepted molecules (blue) are once again those that start inside the separatrix. There are also metastable molecules (orange) which remain outside the acceptance but stay nearby the trap. These are molecules with nearly sufficient energy to escape the trap, but may take some time to do so. We call the occupied area of phase-space at the end of the trapping period the trap's phase-space emittance.

While this applies to a rapid switching off and on of trapping potentials, we note that it is possible to adiabatically transform potentials in such a way that the phase-space density of the ensemble remains unchanged. This can be achieved because the Liouville theorem also holds for time-dependent Hamiltonians, as long as the potential remains conservative throughout [126, 127]. Hence a cloud of trapped particles can be translated, for example in the transport coils, or towards the surface

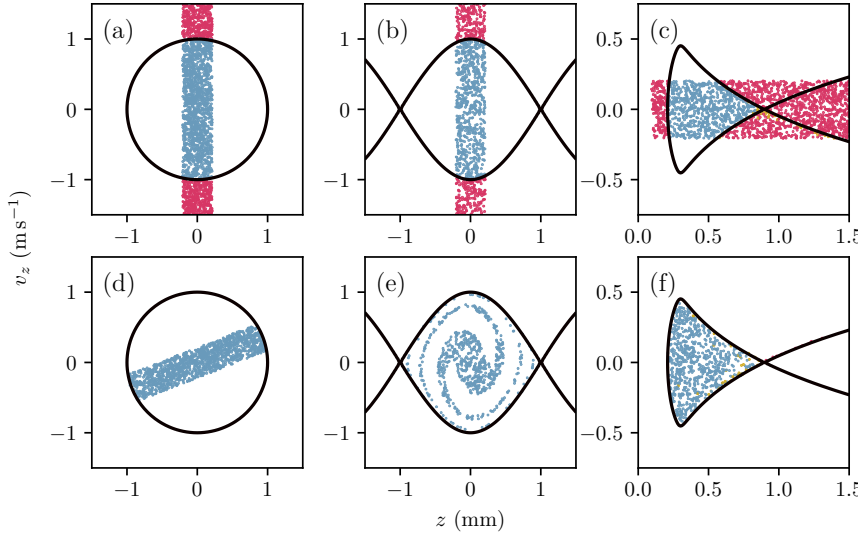


Figure 4.1: The phase-space acceptance for harmonic (a, d), anharmonic (b, e) and Z-wire trap (c, f) are shown. The top row shows the initial positions of the particles: those that are accepted by the trap are shaded blue, particles that are lost are shaded red, and metastable particles in orange. The energy contour of the trap depth is also shown. The end state of the simulation is shown in the lower row. Note the filamentation effect in (e) and (f), where the effective phase-space density of the particles decreases as they explore regions that are energetically accessible. The harmonic and anharmonic examples are inspired by the discussion in Ref. [64].

of the chip as will be discussed in section 4.2.

4.1.2 Simulating the motion

The motion of a particle can be simulated by numerically solving eqn (4.1), which we do using Python [132] and the symplectic Euler method [133, 134] provided by the Desolver package [135]. Unlike other numerical methods, symplectic integrators guarantee the conservation of energy and momentum. We are able to simulate any arbitrary potential, such as those already discussed in the previous section, but it is useful to consider a more realistic potential given by the sum of the magnetic and gravitational potentials,

$$V(t, \mathbf{q}) = V_{\text{mag}} + mg(z_0 - z) \quad (4.12)$$

where $g = 9.8 \text{ m s}^{-2}$ is the acceleration due to gravity, and z_0 is an arbitrary point chosen to be the zero of the gravitational potential. The actual value chosen does not matter as it constitutes only a linear offset in the entire potential. We choose z_0 to be the minimum of the trapping potential at the start of each simulation. The Van der Waals attraction between the chip and the molecules is neglected, since

the molecules will (by design) never be close enough to the chip for this force to be significant.

The magnetic potentials of the wire traps are calculated by considering the traps to be formed of segments of straight wires, each producing a magnetic field $\mathbf{B}_{\text{seg}}^{(i)}$, and the bias field $\mathbf{B}_{\text{bias}}(t)$. The total field is the sum of contributions from the set of all segments (S), and the bias. We also make the approximation that the field changes slowly compared to the alignment of the spin with the field², so that $V = \mu \cdot \mathbf{B} \approx \mu B$. The potential is therefore

$$V_{\text{mag}}(t, \mathbf{q}) = \mu B(t, \mathbf{q}) = \mu \left| \sum_{i \in S} \mathbf{B}_{\text{seg}}^{(i)}(t, \mathbf{q}) + \mathbf{B}_{\text{bias}}(t) \right|, \quad (4.13)$$

where the field of each wire segment is [136]

$$\mathbf{B}_{\text{seg}}(t, \mathbf{q}) = \frac{\mu_0 I(t)}{4\pi s_{\text{seg}}(\mathbf{q})} (\sin(\theta_2) - \sin(\theta_1)) \hat{\phi}. \quad (4.14)$$

Here $s_{\text{seg}}(\mathbf{q})$ represents the shortest distance between the point \mathbf{q} and the line that runs through the segment off to infinity in each direction as defined in Fig. 4.2. We also have the unit vector $\hat{\phi} = \mathbf{I} \times \mathbf{q}/(qI)$.

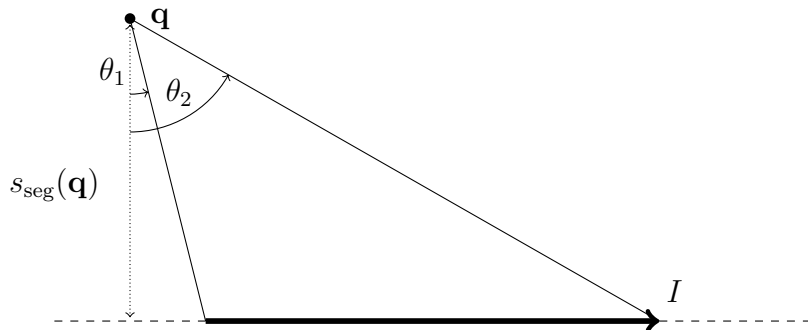


Figure 4.2: Geometry of a wire segment (bold) carrying current I , whose field can be calculated using eqn (4.14). The dotted line shows $s_{\text{seg}}(\mathbf{q})$, the shortest distance from the point at which the field is calculated (\mathbf{q}) to the line parallel with the wire (dashed line).

4.1.3 Simulation initialisation

For all the simulations described below, we begin with a cloud of molecules in a magnetic quadrupole trap. We use the following initialisation procedure so that the distribution of our molecules matches that which we expect in the experiment.

²This means that simulations investigating fast-changing fields present an optimistic result. However we will see below that the limiting factor for changing the field is the time constant of the classical motion of the molecules (which is longer than the dipole alignment). Hence this adiabatic approximation is sufficient for our investigations.

The simulation begins with a cloud of N molecules whose positions are normally distributed in all three spatial dimensions with a standard deviation of σ_i (typically $\sigma_i = 1\text{ mm}$). Similarly the velocity components are normally distributed with a standard deviation of σ_{v_i} (typically 400 mm s^{-1} , corresponding to a temperature of $50\text{ }\mu\text{K}$).

The cloud is initialised in a quadrupole trap with gradient 10 G cm^{-1} . They are held for 50 ms before the gradient is linearly ramped over 100 ms to 60 G cm^{-1} (the gradient used in the MTT). The molecules are then held for a further 50 ms, as a stabilisation time. The increasing trap gradient compresses the distribution. The resulting distribution is Gaussian in velocity and position, centred on $z = 3\text{ mm}$, as shown in Fig. 4.3.

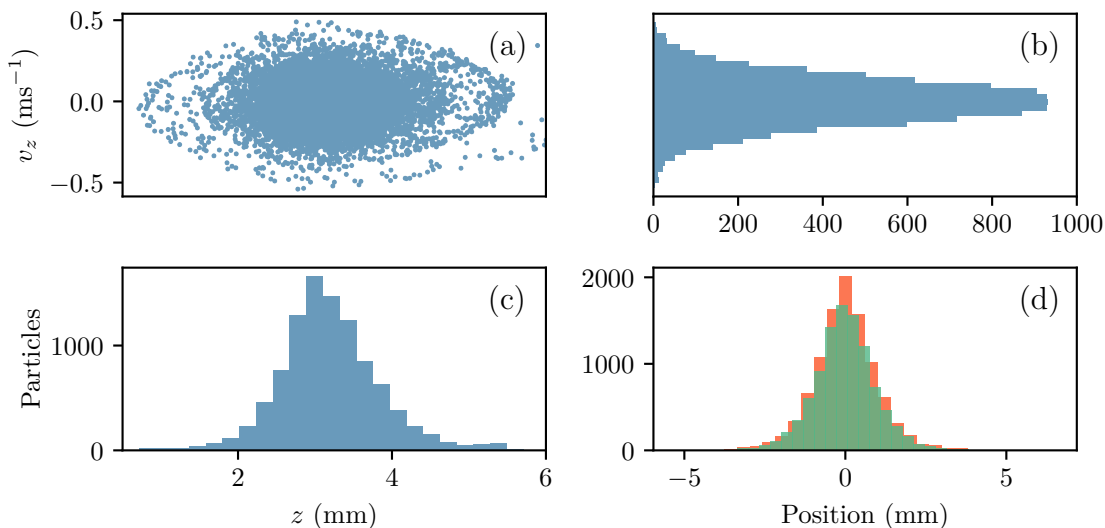


Figure 4.3: The particle distribution in phase-space after initialisation. A scatter plot of the $z v_z$ -phase-space plane the is shown in (a), with histograms of z and v_z distributions in (b) and (c) respectively. The position distributions for x and y are shown in (d) in orange and green respectively.

4.2 Adiabatic transfer between traps

It should be obvious that if we start with molecules in one potential, then rapidly turn that one off and turn on another with a different shape, is likely to cause heating and increase the size of the cloud. However, if we ramp between the traps adiabatically then we expect the phase-space density to be conserved. In order to understand how best to load the chip trap it is important that we understand the extent of heating in the case of rapid transfer and the timescale required to be adiabatic with respect to the motion of the molecules.

We investigate this with a simple example: consider two ideal quadrupole traps with gradients of 60 G cm^{-1} separated by 3 mm in the x direction. We simulate 2000 CaF molecules using the above-described initialisation procedure, with initial $\sigma_i = 2 \text{ mm}$ in all directions, and initial temperature $T = 50 \mu\text{K}$. We ramp linearly between the potentials in a time t_{ramp} , which we vary between 1 ms and 100 ms. The molecules are then held for a further 100 ms. The state of the system at the end of the simulation is shown for $t_{\text{ramp}} \in \{1 \text{ ms}, 30 \text{ ms}, 100 \text{ ms}\}$ in Fig. 4.4, along with the behaviour of the cloud in the 100 ms hold time. Note that as the ramp time increases, the oscillation in cloud size, temperate and position decreases, as we have said we expect.

The question then is at what point do we enter the adiabatic regime? Fig. 4.5 shows the cloud width and temperature at the end of the simulation for varying t_{ramp} . After $t_{\text{ramp}} \sim 50 \text{ ms}$ the reduction is minimal, and we are strongly in the adiabatic regime. This is approximately the timescale we would expect. Although the trap is not harmonic, we can still give the characteristic period for a particle that has a characteristic amplitude of motion. Assuming that the particle is under constant acceleration, the timescale for a particle to traverse the trap is

$$\tau = \sqrt{\frac{m\sigma}{\mu_B B'}}, \quad (4.15)$$

where σ here means the width of the trapped cloud. To be in the adiabatic regime, we expect to have any particle traverse the trap multiple times over the duration of a ramp. Our typical CaF clouds have width $\sigma = 5 \text{ mm}$, so the timescale will be $\tau \approx 10 \text{ ms}$. We expect the adiabatic regime to be reached when a process takes place over a duration that is several multiples of this timescale, which is in good agreement with the simulations.

4.3 Trajectory simulation of the initial loading stages

In this section we will present simulations of loading molecules from the MTT into the on-chip Z-wire traps. This demonstrates the two main types of transitions in the loading process: handovers between traps, and compression within a single trap. The timing of the simulation do not exactly reflect those that will be used in practice and long holding periods have been inserted between ramps to better illustrate the cause of particle loss. It is useful to perform direct trajectory simulations as opposed to simple analysis of the phase-space emittance and acceptance, since (as we will see later) brief lowering of trap depth during trap handovers can induce additional

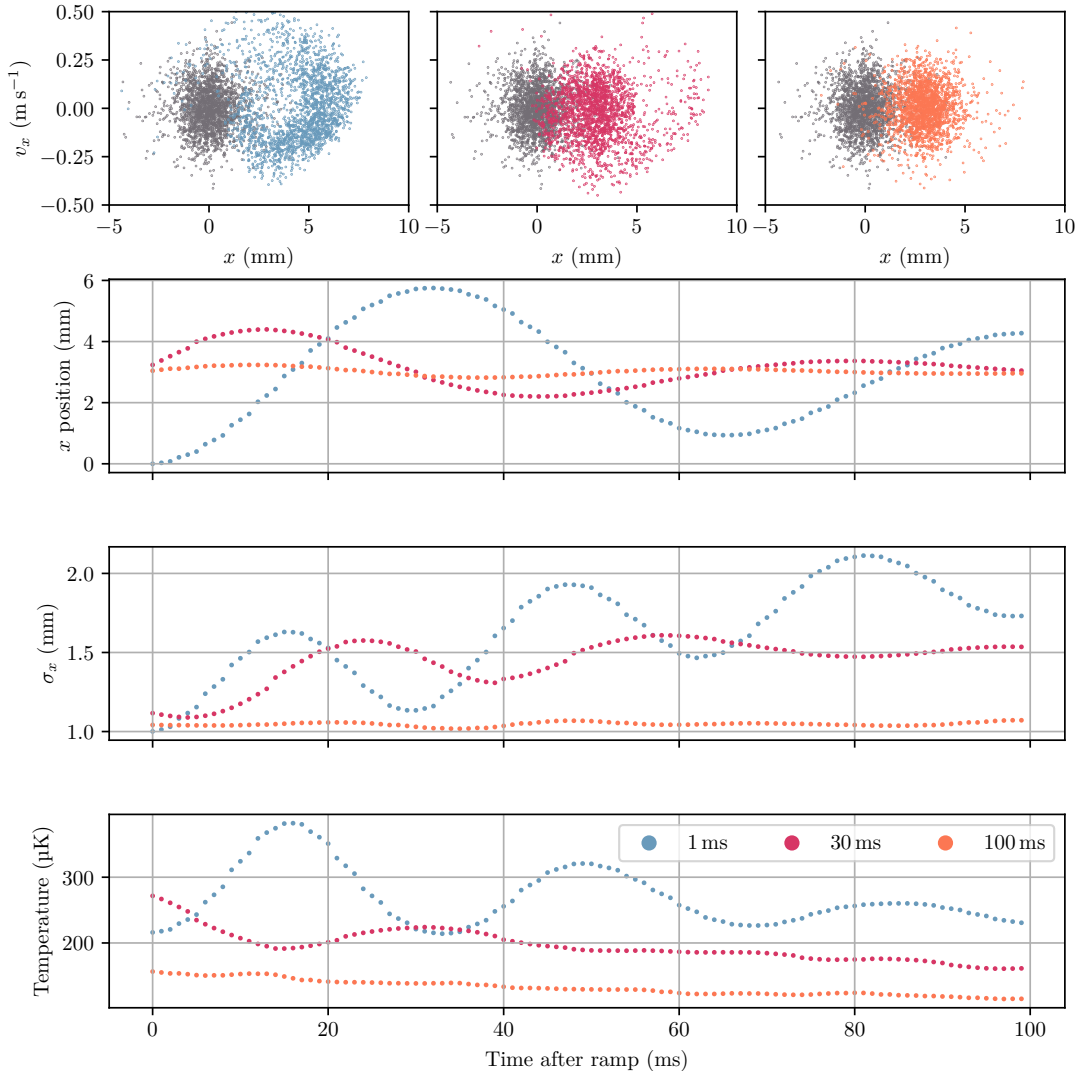


Figure 4.4: Exchange between two quadrupole traps, separated by 3 mm, for three different ramp times. The top row shows the x -projection of the phase-space distributions of the particles at the start of the simulation (grey) and after various ramp times (see legend) followed by a 100 ms hold in the displaced trap. The mean position, size and temperature of the cloud are shown throughout the hold time for each simulation. Note that for the longer ramps we observe less severe heating, oscillation and widening of the cloud.

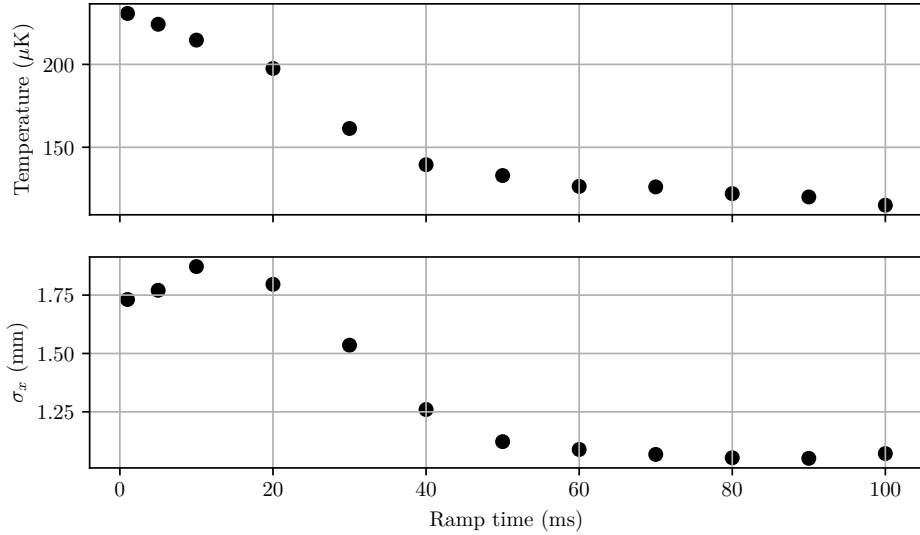


Figure 4.5: The final temperature and size of particle clouds transferred between offset quadrupole traps at various ramp times. Note that the large oscillations in width that occur for short ramp times (see Fig. 4.4) can result in the instantaneous width of the cloud being small, such as in the shorter ramp times here.

loss of particles.

We will consider the handover in four stages: the particle initialisation, which was already discussed in section 4.1.3; followed by the handover from the MTT to the U-wire; then the U-wire to Z_0_i . Finally we will simulate the compression in the Z-wire trap from Z_0_i to Z_0_f . A full summary of the changing parameters throughout the simulations is given at the end of the section, see especially Fig. 4.10. Note that throughout the rest of this chapter we say that the chip is situated at a height $z = 0$.

4.3.1 MTT - U transfer

The cloud is initialised by the usual procedure, with $\sigma_i = 1 \text{ mm}$ and $T = 50 \mu\text{K}$, corresponding to the typical cloud sizes and temperatures we measure in the tweezer chamber after transport. Over 100 ms the coil current is linearly reduced to zero and the U-wire current is ramped up to its maximum value of 100 A. The bias fields in the y and z directions (no x bias is applied) are also ramped linearly, to maintain the trap centre at a height of 3 mm below the chip. The state of the system before and after the ramp is shown in Fig. 4.6.

The phase-space distribution in the $z-v_z$ projection is shown for the start (Fig. 4.6 (a)) and end (Fig. 4.6 (b)) of the simulation. Note that there is little change to the velocity distribution, but in position the particles shift to occupy the positive z direction, where the potential is less steep.

Looking at the change in the particle number throughout the ramp (grey region

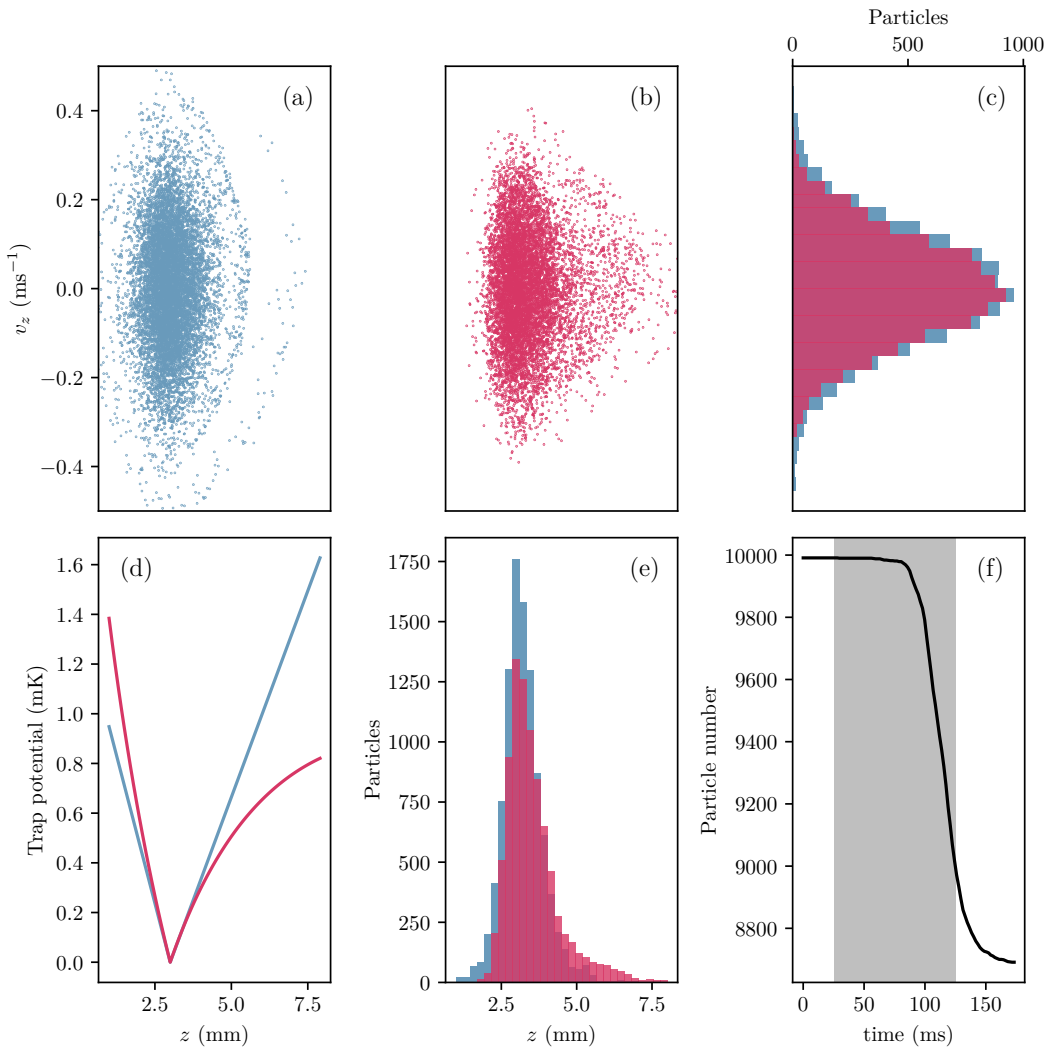


Figure 4.6: The simulation of the transfer from the MTT to the U-wire. The state of the system is presented at the end of the initialisation procedure (blue) when the trapping potential is that of the MTT, and after ramping to the U-trap (red). The phase-space distributions are shown in the z - v_z plane in (a) and (b), with histograms of the z and v_z projections in (c) and (e) respectively. The potentials at the start and end of the transfer are shown in (d). Subfigure (f) shows the temperature and the particle number varying throughout. Transfer occurs during the times that are shaded grey (c.f. Fig. 4.10).

of Fig. 4.6 (f)) it is clear that there is some particle loss. We would naively expect there to be no loss during this transfer, since the final trap depth is larger than the temperature of the cloud, and there is good mode-matching of the two potentials. To see why this loss occurs, we look at the evolution in phase-space for each projection throughout the ramp, as shown in Fig. 4.7.

At $t = 75$ ms there is a noticeable decrease in the trapping depth in the $-y$ and $+z$ directions. This is the cause of the particle leak, and occurs due to the superposition of the two fields causing an overall decrease in the trap depth. When the trap depth is increased again, the energy of particles in this region is increased, and they can leave the trap. This only occurs for a brief period during the ramp (lasting approximately 40 ms). Hence some of the more energetic particles are lost, as can be seen in the figure. The key finding is that the molecules are able to be transferred from the MTT to the U-trap with minimal loss by mode-matching of the potentials.

4.3.2 U - Z transfer

The next stage of loading is the U to Z_{0i} handover. We simulate this process as a continuation of the MTT-U transfer. The Z-wire current is then linearly ramped on over 100 ms to 30 A, while the U-wire current is ramped off. The bias fields are linearly ramped to maintain the trap height at 3 mm. The simulation is presented in Fig. 4.8, and the ramps are summarised in Fig. 4.10.

In the former figure we have the initial (a, blue) and final (b, red) particle distributions. With the z velocities and positions summarised in the histograms in (c) and (e) respectively. We can see that the mean position and velocity remains the same, but it is clear from (b) that there are a number of particles that have picked up velocity in the positive z direction, and can be seen leaving the trap. This is the notable streak to the right of the subfigure, and can also be seen in the tail of the histogram in (e). The particle number decreases by 20% as seen in (f), although the particles do not fully leave the trap until the next step (see Fig. 4.10 (d)). This loss is similar to that of the MTT to U-trap handover, with a decrease in trap depth that we attribute from changing from a quadrupole to Ioffe-Pritchard trap. This changeover can be seen in (d) where we note that the final trapping potential's minimum is non-zero. Despite the particle losses there is minimal change to the particle distribution

4.3.3 Z compression

The final stage of the loading procedure is a linear ramp of the trap height from 3 mm below the chip surface to 1 mm below. Here only the y bias field is changed so that

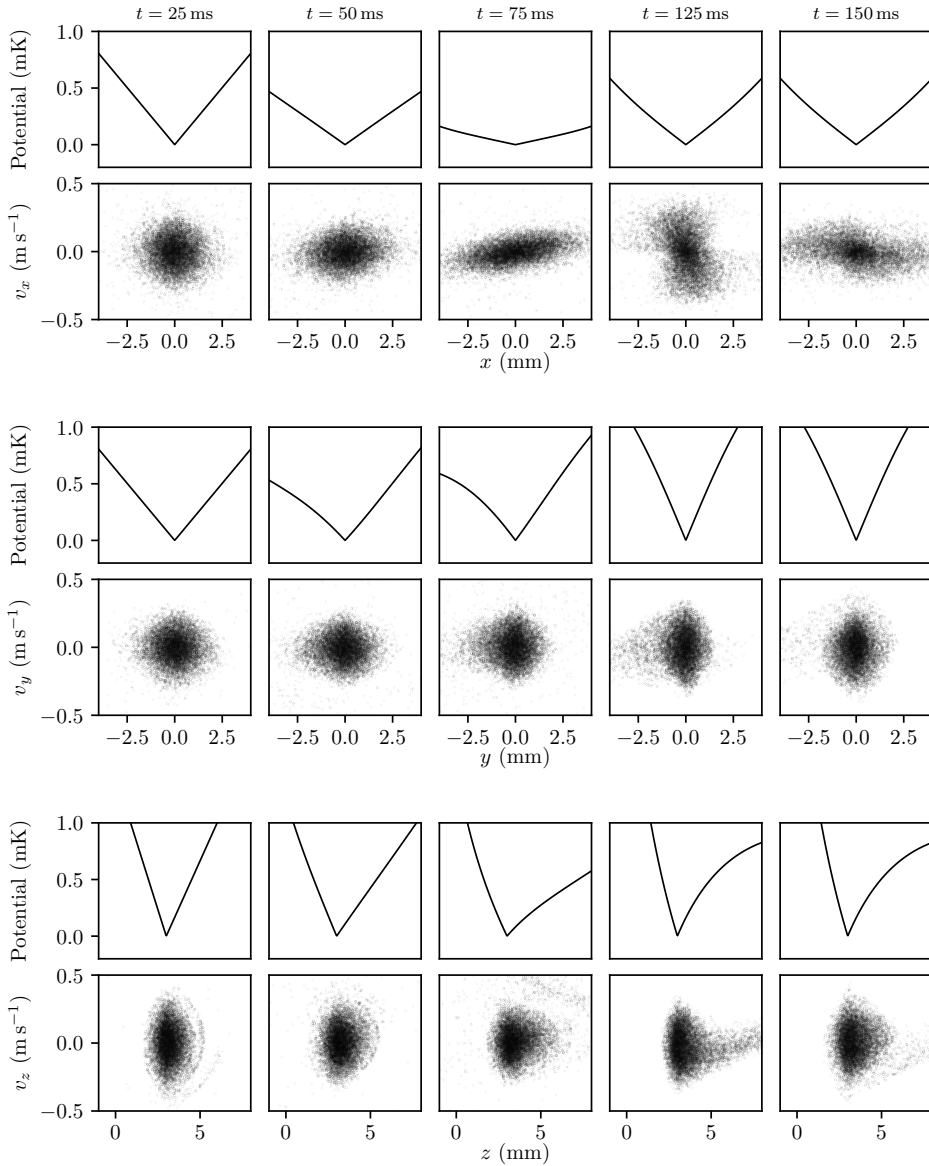


Figure 4.7: Each pair of rows shows the phase-space plots for the MTT to U-trap handover simulation in the q_i-v_i plane, along with the cut-through of the potential through the trap centre along q_i at various times. This supplements the simulation summary shown in Fig. 4.6. The superposition of the quadrupole and U-traps briefly causes a lowering of the trapping potential, as can be seen at 75 ms. These reductions can occur when moving between different types of traps, such as from the coil-based to wire trap, or from a quadrupole to Ioffe-Pritchard trap. Care must be taken in such cases to ensure the potential is sufficiently deep throughout the handover.

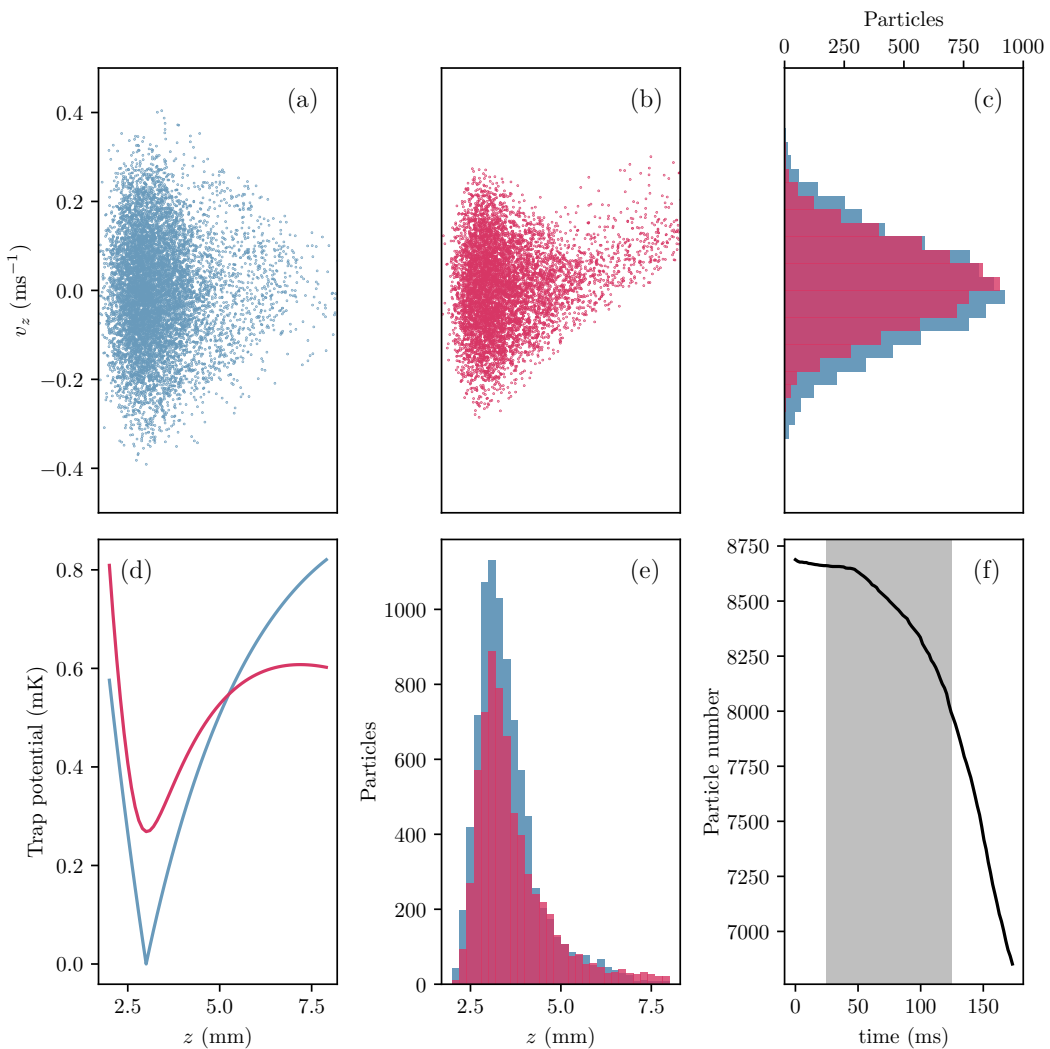


Figure 4.8: The simulation of the transfer from the U-wire to the Z-wire. The state of the system is presented at the end of the initialisation procedure (blue) when the trapping potential is that of the U-trap, and after ramping to the Z-trap (red). The phase-space distributions are shown in the z - v_z plane in (a) and (b), with histograms of the z and v_z projections in (c) and (e) respectively. The potentials at the start and end of the transfer are shown in (d). Subfigure (f) shows the temperature and the particle number varying throughout the simulation. Transfer occurs during the times that are shaded grey (c.f. Fig. 4.10).

the trap depth increases and the cloud is compressed, providing good localisation of the molecules. Ramping the height linearly requires the bias to change as a function of time so that $\tilde{B}_y \propto t^{-1}$.

As can be seen in Fig. 4.9, there is particle loss, although much of this is due to particles that had already left the trapping region in the previous ramp. As can be seen in subfigure (f), the particle number is decreasing before the ramp begins. The other major effect of the ramp is heating, which occurs due to the spatial compression and conservation of phase-space density. The transfer of the cloud towards the chip surface is successful, as can be seen in Fig. 4.9 (e), the particles are highly localised around the new trap minimum at $z = 1$ mm.

4.3.4 Summary of the simulation

The entire simulation from MTT to Z_{0f} is summarised in Fig. 4.10. For each stage: initialisation (a), MTT-U transfer (b), U-Z transfer (c) and Z compression (d) the particle number is shown. The total temperature and cloud width are also given for the particles that remain in the trap at the end of the simulation. The profile of parameters that are changed for each ramp are also shown.

The simulation shows that the loading of the initial chip trap can bring in approximately 60% of the initial cloud. We assumed an initial temperature of $50\text{ }\mu\text{K}$, however refining the transport process could allow us to load clouds of lower temperatures, which could mean that a higher loading efficiency is possible. It may also be possible to implement cooling during the trap transfer, but this is restricted by the limited optical access in the chip chamber. There is some expansion of the cloud as molecules are lost, particularly caused during the U-Z handover stage. Heating in the trap is largely due to the compression in the final stage. This is inevitable, but does not cause any problems, since the trap depth increases for traps closer to the surface, and the molecules are well contained.

The trajectory simulation discussed in this section is instructive, since it tells us about the handovers between different types of traps. Notice that the largest source of particle loss is when converting from the quadrupole U-trap to the Ioffe-Pritchard Z-trap. Here it is not sufficient to look just at the phase-space emittance and acceptance in the final traps, but we must investigate the potential across the ramp, since a brief lowering of the potential can induce enormous loss. Fortunately this is not an issue when compressing and handing over between Z-traps, and the phase-space analysis is sufficient for the rest of the procedure.

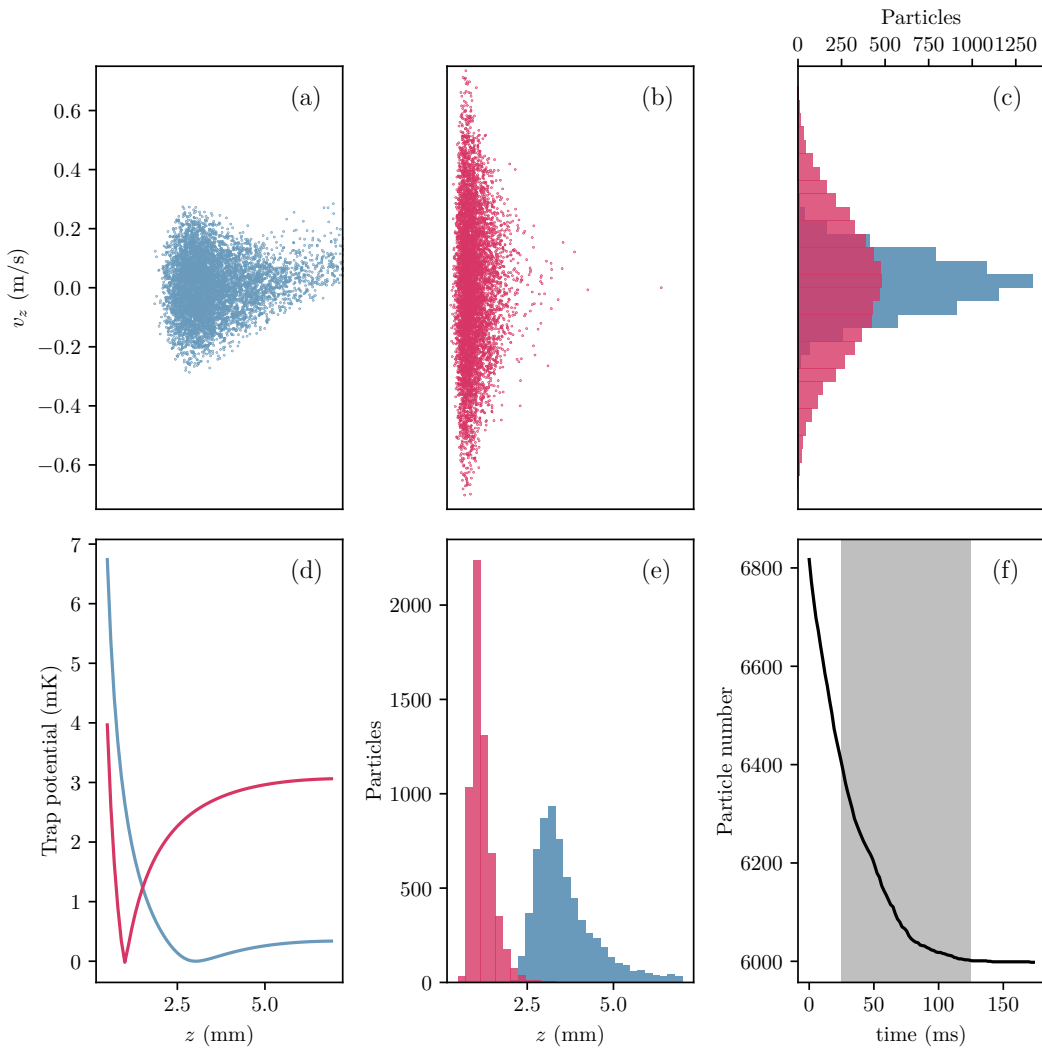


Figure 4.9: The simulation of the compression in the Z-wire trap. The state of the system is presented at the end of the initialisation procedure (blue) when the trapping potential minimum is held 3 mm from the surface, and after compressing to the height of 1 mm (red). The phase-space distributions are shown in the z - v_z plane in (a) and (b), with histograms of the z and v_z projections in (c) and (e) respectively. The potentials at the start and end of the transfer are shown in (d). Subfigure (f) shows the temperature and the particle number varying throughout the simulation. Transfer occurs during the times that are shaded grey (c.f. Fig. 4.10).

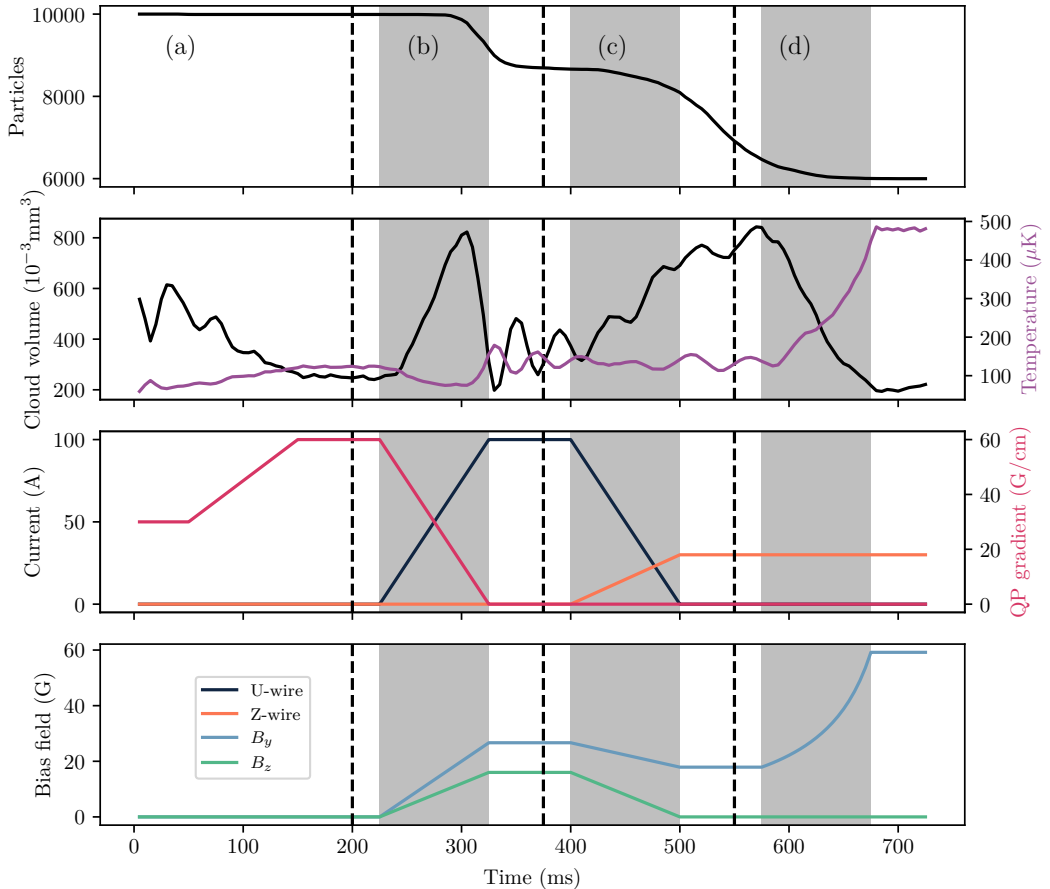


Figure 4.10: Details for each stage of the simulation in turn. The top two rows show properties of the molecule cloud and the second two rows show the trapping currents and bias fields throughout. Column (a) shows the initialisation procedure. Column (b) shows the ramp from the MTT to U-wire, with the ramp duration shaded grey. In column (c) we have the U-Z handover and the z bias field is switched off. Finally in column (d) is the compression in the Z-trap.

4.4 Phase-space acceptance of remaining Z-traps

Once trapped in Z_{0f} , the remaining loading stages are simply repeated handovers to the smaller wires, with a compression stage carried out on each wire to bring the molecules closer to the surface. This is a well-understood and robust procedure that has been used before to load atom chips with minimal losses [137]. The ramps used are detailed in table 3.3. The timing of the ramps could be shorter for the Z-traps, since the timescale of motion in these traps is higher. This, as well as the optimal shape of the ramp can be determined empirically.

That said, since our experiment will operate with a significantly lower phase space density than previous experiments with atoms, it is important to ensure that our loading procedure will not suffer from any unnecessary losses. These compressed traps contain hotter molecules, requiring a smaller time step for simulation. It is therefore easier to directly examine the acceptance of each trap. We also note now that the trap gradients are sufficiently large the effects of gravity can be ignored.

The trap acceptances are shown in Fig. 4.11, starting with Z_{0f} in row (a). The region of the trap that we expect to be occupied (as determined by the simulation above) is marked with a dashed line. This cloud of molecules will be adiabatically transferred into Z_{1i} . The cloud of molecules will be transferred to Z_{1i} with negligible heating. However, the total acceptance of the trap is less than the expected phase-space volume of the cloud. We can estimate the spillover loss to be 73% on the phase-space volumes in Fig. 4.11. Performing the handover adiabatically will maximise the number of molecules that can be transferred.

Next, Z_{1i} is adiabatically compressed to Z_{1f} , with the molecules held 100 μm from the surface, as shown in row (b). The particles will undergo filamentation, exploring all regions that are energetically accessible and increasing the effective phase-space volume that they occupy. This expected occupation region is calculated from the energy-contour in phase-space that matches the temperature of the cloud, and is marked by the dotted line. There is now handover into Z_{2i} , with the particles inside the phase-space acceptance contained in the new trap. We expect spillover losses of 84%. In the final stage the trap is compressed, into Z_{2f} , during which we expect no loss. The final occupation is shown in Fig. 4.11 (c). Particle loss during the procedure can be estimated from the mismatching of these phase-space emittances and acceptances.

The above-described spillover losses can be combined with the loading efficiency determined by the trajectory simulations. We expect a total loading efficiency of 2%. This would deliver only 50 molecules into the final trap in what is a highly-idealised loading simulation. Notably the analysis of the phase-space acceptance does not account for decrease in effective phase-space density by filamentation, which will

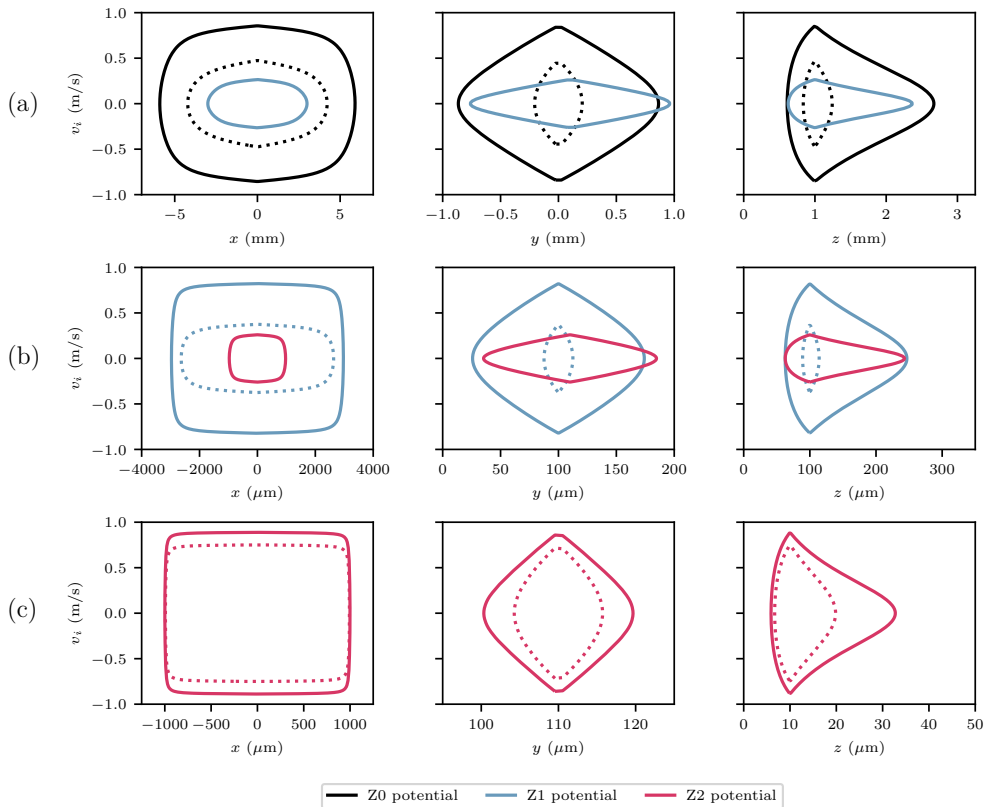


Figure 4.11: The acceptance (solid) and expected occupation (dashed) of each Z-wire trap. This is calculated by finding the acceptance in the weak (x) trapping direction. Row (a) shows Z_{0f} , with occupation determined by the above simulation. Molecules will be adiabatically transferred to Z_{1i} , which will be fully occupied. Some particles will be lost due to the decrease in acceptance but this is to be expected, and phase-space density should not increase. In (b) we have the acceptance and occupation of Z_{1f} following adiabatic compression. Particles will be adiabatically transferred into Z_{2i} , resulting in similar losses to the previous step. Row (c) shows the final acceptance and occupation of Z_{2f} .

further reduce the final occupation. This confirms that we will need to produce a much higher initial phase-space density to load a sufficiently large number of molecules into the trap. However it is clear that this procedure can be applied to much higher density clouds, such as those which can be produced using optical dipole traps. Ongoing efforts to produce higher density clouds of CaF could improve this final molecule number even further.

4.5 Summary

In this chapter I have presented the design of the chip experiment, starting with the source of molecules up to the stage of confinement in a Z-trap $10\mu\text{m}$ from the chip surface. I have presented a loading procedure that will allow us to load this final trap through a series of wire traps of decreasing size. This is justified by simulation and phase-space analysis of the acceptance of the various trapping stages. The design leaves scope for the addition of microwave guides on a second layer above the trapping wires, as discussed in section 2.2.

Chapter 5

Microfabrication

This chapter details the production of our chip traps. Since we require features with dimensions on the scale of several micrometers, we have employed photolithography techniques, which were undertaken in cleanroom facilities at the London Centre for Nanotechnology (LCN) cleanroom.

5.1 Overview of the fabrication procedure

As discussed in section 3.2, our trap has been designed so that the size of the wires is small compared to the size and height of the trapped cloud. As such trapping wires on the chip are as small as $6\text{ }\mu\text{m}$ in width. Such small features can be produced using standard photolithography techniques [138] however, the maximum height of features produced in these procedures is usually of the order 100 nm. The approximate height required for our wires can be calculated using a typical current density achieved on atom chips, such as that reported in Ref. [46], where this value is $j = 6 \times 10^{10} \text{ A m}^{-2}$. Using the wire widths and currents in Table 3.3, it is clear that the height required for our wires is $h \sim Iw/j = 1 \text{ A} \times 10 \text{ }\mu\text{m}/6 \times 10^{10} \text{ A m}^{-2} \sim 1 \text{ }\mu\text{m}$.

Such tall wires can be achieved by through-mask electroplating [139]. First a substrate is coated with a thin seed layer of gold, then photolithography is used to produce a thick (several micrometer high) mould. The mould covers regions where no further deposition is required. The substrate can then be electroplated, with the seed layer acting as the anode, allowing thick wires to be deposited into the mould. After electroplating the seed layer can be etched away. This technique has been used previously for constructing atom chips and is described in Refs. [108, 140, 141].

Our fabrication process begins with a 100 mm diameter silicon with a 300 nm silicon dioxide layer on the polished surface. These wafers are purchased from Pi-Kem, and are of nominal thickness 450 μm –600 μm and $\langle 100 \rangle$ orientation, although these are arbitrary choices for our purposes. The fabrication can then be summarised as follows:

1. Dice silicon wafer into 20 mm by 20 mm dies.
2. Evaporate adhesion layer of chromium ($\sim 10 \text{ nm}$).
3. Evaporate seed layer of gold ($\sim 50 \text{ nm}$).
4. Spin coat a thick (6 μm) layer of photoresist.
5. Expose photoresist to pattern the die.
6. Develop photoresist to create photoresist mould.
7. Electroplate the chip, such that wires are formed in the mould to the desired height.
8. Remove the photoresist mould.
9. Chemically etch the gold seed layer.
10. Chemically etch the chromium adhesion layer so as to electrically isolate the wires.

This process is illustrated in Fig. 5.1.

As discussed in chapter 1, a future aim of the molecule chip project is to integrate microwave guides on the chip. These guides must allow good overlap of the microwave fields and the molecule trapping region. Our design achieves this by positioning the microwave guides on a second layer, directly above the trapping wires. We have not yet attempted the following stages of fabrication, but we anticipate that they will be:

11. Spin coat chip with an insulating layer of polyimide.
12. Perform standard photolithography to lay down microwave guides on the chip.

These steps are discussed further in section 5.10.

We learned to use the cleanroom facilities and developed the chip design in parallel. An example of an early design for the chip is shown in Fig. 5.2. These early design choices were informed by some of the ideas discussed in section 3.2, but were overly complicated, and were based on the assumption that the traps should share an axial wire, so that all trap centres were in the same position in the $x y$ -plane. Later analysis using preliminary simulations similar showed that this was not necessary, and so a design more similar to that shown in Fig. 3.9 was adopted.

In this chapter I will present the development of the fabrication process in detail. At times I will present data for the early designs of the chip, which was useful to inform later fabrication of the final design. I will describe the various pitfalls we encountered and point out where limitations of the process have led to changes in the design of the chip.

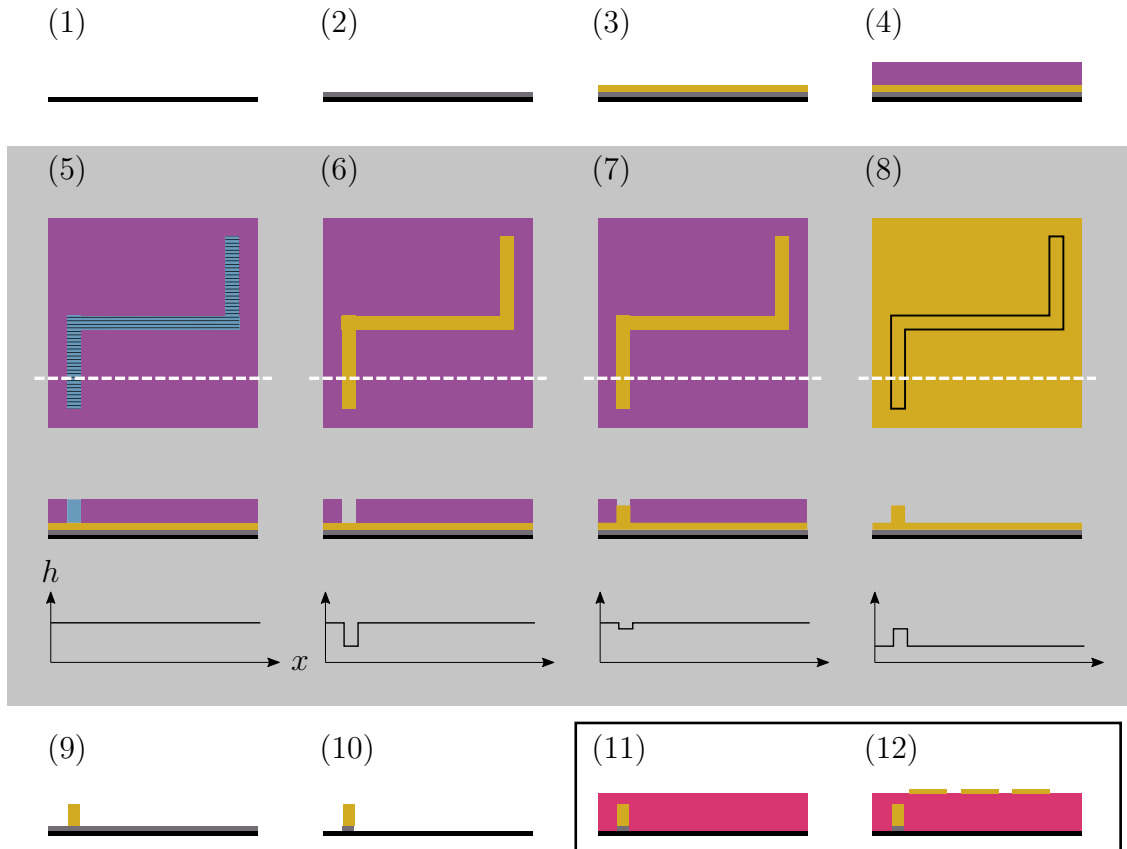


Figure 5.1: Illustration of the fabrication process. We begin with a bare silicon die (black) which has already been cut to the desired size, and is shown here in profile. We evaporate a chromium adhesion layer (2, grey) followed by the gold seed layer (3, gold). A thick ($\sim 6 \mu\text{m}$) layer of photoresist (purple) is spin coated (4).

Steps 5–8, highlighted in the grey box, include a more detailed overview of through-mask electroplating, with a top-down view (top row), profile view (second row) and profilometer scan (bottom row). The dashed line denotes the cross section for the profile view and profilometer scan. In (5) a region of photoresist (blue) is exposed to the ultraviolet light by scanning (black lines, not to scale) of the direct writer. The die is then developed (6) to create a photoresist mould, which can be electroplated to build tall wires (7). Removing the mould (8) leaves only the tall wires, and the initial metal layers.

The gold (9) and then chromium layers (10) are etched to separate the features. Planned further fabrication steps are shown in the lower right hand box. We intend to spin coat with polyimide (11, pink), allowing fabrication of features such as microwave guides on a second layer above the trapping wires (12).

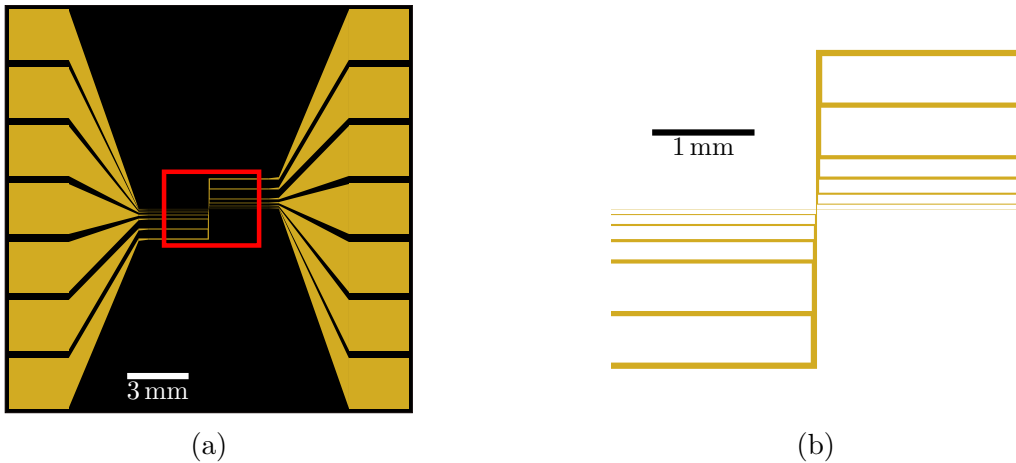


Figure 5.2: Wire layout for an early design used in initial testing of microfabrication procedures. The whole chip is shown in subfigure (a), with the central region marked by the black box shown in detail in subfigure (b). Note that the six Z-traps in this design share an overlapping axial wire, whose size tapers close to the centre. The wire widths range from $60\text{ }\mu\text{m}$ – $10\text{ }\mu\text{m}$, and the axis lengths are in the range $3000\text{ }\mu\text{m}$ – $90\text{ }\mu\text{m}$. There is also a central wire to form a dimple trap with width $3\text{ }\mu\text{m}$.

5.2 Metal evaporation of seed layer

Before any fabrication, the die must be cleaned and dehydrated to ensure that there will be good adhesion to the substrate. A solvent clean with acetone and isopropyl alcohol will remove any organic compounds. The die is then rinsed with deionised water and dehydrated in an oxygen plasma for ten minutes. The die is then ready for metalization, which here is done by metal evaporation. To further improve adhesion between the gold and silicon, a thin ($< 10\text{ nm}$) intermediary chrome layer is deposited first, followed by a nominal 50 nm of gold. These heights are recorded for later calculation of etching time.

We performed evaporation using an Edwards A306 bell jar evaporator. Typically we metalize four dies at a time. They are loaded into the bell jar, along with gold and chrome, using a boat and rod respectively. The dies are positioned with the polished side facing down towards the metal. This arrangement is shown in Fig. 5.3.

The bell jar is pumped down to pressures below 10^{-6} mbar over a few hours. The metal for deposition can be selected from a carousel, and heated by electric current inducing evaporation. A shutter is used to block deposition onto the substrate until the desired current has been reached. It is then opened to begin deposition. The Edwards bell jar evaporator incorporates a FTM7 deposition monitor, which reports the rate of deposition and automatically shuts off deposition once the desired thickness has been reached by closing the shutter. The current is then slowly decreased so that the vacuum can be lifted and the dies retrieved.

We typically achieve a deposition rate of 0.2 nm s^{-1} . As discussed above, a

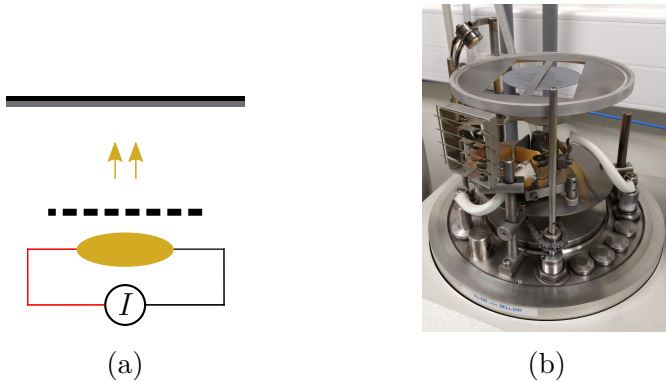


Figure 5.3: Subfigure (a) schematically shows evaporation of gold (yellow) onto a silicon (black) die with chromium (grey) adhesion layer. The shutter (dashed line) can block the evaporating gold from being deposited when the target height is reached. The Edwards bell jar evaporator is shown in (b), with the bell jar removed and a wafer mounted for deposition.

thickness of $5\text{ }\mu\text{m}$ is desirable for the chip's trapping wires. Achieving this with evaporation would take over an hour, and the bell jar would then require extensive cleaning after use. It is further unclear if the desired thickness would be possible due to limitations of the amount of gold that could be loaded into this machine. We therefore opt to use use through-mask electroplating to achieve the desired thickness.

5.3 Spin coating of photoresist

Spin coating is a procedure for distributing a uniform film such as a photoresist across a substrate [142]. It is typically followed by baking to solidify the layer. We use spin coating to apply Dupont SPR220-7 photoresist, which will form the mould for the wires.

The die is mounted in a spin coater, and approximately 1 mm of SPR220-7 is applied. The die undergoes a 2 s ramp to 500 rpm where it is held before a 1 s ramp to 4000 rpm and it is held for 30 s . This results in a nominal $6\text{ }\mu\text{m}$ high coating of photoresist, although it is possible to coat up to $9\text{ }\mu\text{m}$ if desired, which could be used for plating taller wires. SPR220-7 requires a post-application bake, first at 90°C for two minutes, then immediately afterwards at 120°C .

Spin coating the photoresist results in a bead at the edge of the die. This thick region of photoresist may not receive sufficient exposure to fully develop later which can cause defects in features near the edge. It is possible to remove the bead by inserting an initial exposure and development step before the lithography discussed in the next section. Using too much photoresist during coating can produce an unduly thick bead, which can further interfere with photolithography steps. We found that approximately half a millilitre of photoresist was sufficient, however the liquid

is very viscous and care must be taken not to introduce bubbles during pipetting as these cause a poor coat.

5.4 Lithography of the wire mould

The common and, perhaps, traditional way to perform photolithography is to use a mercury lamp and a chrome-on-glass mask to cast light onto the substrate, with the mask casting a shadow so as to illuminate only the desired region [138]. This was the method that we began using at the start of the project, however we found that it was easier to achieve reliable results by using the Heidelberg DWL 66, a direct writer [143].

Instead of using a mask to cast a shadow, the direct writer uses a tightly focused ultraviolet laser, whose beam is scanned across the surface. The beam is then switched on and off so as to produce the pattern that is required. This process is depicted for an example pattern in Fig. 5.1 (5). The Heidelberg DWL 66 is capable of producing features down to 300 nm in size, well below our smallest feature sizes on the order of a few micrometers.

Since designs can be directly uploaded to the direct writer, there is no need to wait for a third party to construct a mask. Hence the direct writer allows rapid prototyping. It also has the benefit of making alignment easier, since this can be performed automatically by the computer, and any issues with mask-die contact are avoided entirely.

The SPR220-7 is a positive photoresist, meaning that areas exposed to the light are those which will be removed on developing. An exposure energy of 140 mJ cm^{-2} is required, which is administered over three passes. The laser power is calibrated to achieve the correct exposure, operating at 70 mW. The whole scan for one die takes around twenty minutes.

Following exposure a rehydration step is required. The die is left at ambient temperature overnight before it is developed in Microposit MF-319 until it runs clear, and then for 30 s extra (usually about two minutes total). This produces the die with mould as depicted in Fig. 5.1 (6).

5.4.1 Troubleshooting

The photoresist bead commonly caused defects in the end product (for an example see Fig. 5.9), so we took additional photolithography steps to avoid this. Conventionally a bead can be removed by an initial exposure of the edge of the sample, followed by a short development to remove some of this photoresist. With the direct writer it is possible to perform targeted exposure of the affected features. We

performed a second exposure of features within 1 mm of the edge of the die. Since these features are all very large (feature size on the order of millimeters), they are not negatively impacted by the effects of overexposure of the photoresist.

A common problem that we faced early in development was underexposing the photoresist. This meant that some features were entirely missing from the mould, and others were incomplete, with photoresist remaining at the bottom of the mould after developing. This blocks the current during electroplating, and prevents the formation of wires. This can be seen with the microscope as shown in Fig. 5.4 (a). Electroplating such a mould will confirm that the wires cannot be formed, and that the mould is malformed.

If the die has not had sufficient exposure then it is very difficult to re-align the die to re-expose, however it is often the case that further developing time is required. Returning the die to the Microposit MF-319 solution can complete the development. These problems can be difficult to identify before plating, but a simple check is a visual inspection for any blockages in the moulds. Another indicator that the photoresist has been successfully removed is if there is good electrical contact through the seed layer at the wire bond pads, which can be checked with a multimeter.

5.5 Electroplating the tall wires

Next the chip is returned to CCM for through-mask electroplating. It is important that the dies are treated with great care during transport, and kept sealed until electroplating can begin. We found that the dies were surprisingly robust, and were able to be kept for several weeks between exposure and electroplating.

In electroplating, a conductive target (here the die) is connected to an electric circuit as an anode and placed into an electrolytic solution along with a cathode. Current is passed through the solution causing ions to be deposited onto the target. This is illustrated in Fig. 5.5 (a) and an overview of electroplating can be found in Ref. [144]. Reference [139] gives a more specific discussion of using electroplating for microfabrication.

Gold will be deposited in the regions that are not covered by the photoresist mould, as shown in Fig. 5.5 (see especially the grey box). This method allows us to produce wires up to the thickness of the photoresist height. Above this the wires will begin to ‘mushroom,’ [139] spreading out across the top of the photoresist and losing their shape. We will see here that we are able to reliably produce wires of height 6 μm . The results of the process are shown schematically in Fig. 5.1 (5–8).

The height h achieved in a deposition of duration t is given by the Faraday

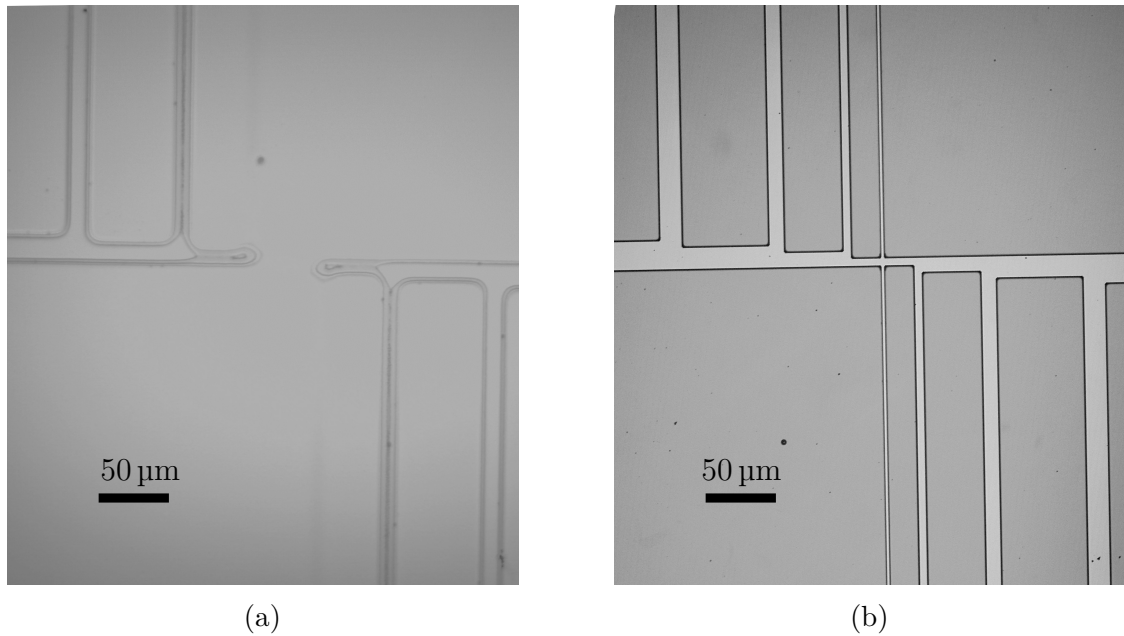


Figure 5.4: Photoresist moulds using the earlier design shown in Fig. 5.2. In (a) we see the effects of underexposure, features below $\sim 20\text{ }\mu\text{m}$ are completely absent. The $20\text{ }\mu\text{m}$ wire is present but has not been completely developed. Subfigure (b) shows a well-exposed die of the same design, with sharp features and clear trenches in which the wires can be plated.

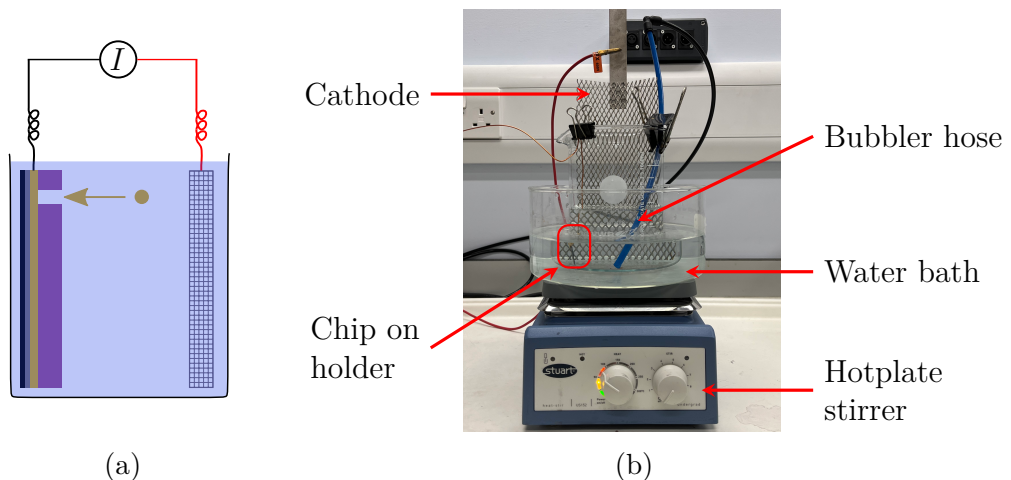


Figure 5.5: The electroplating scheme is shown schematically in (a). A die is submerged in a gold electrolyte (light blue) along with an electrode (grey mesh). These are connected to a current supply to enable current flow and deposition of gold ions (yellow circle) is depicted. The solution is held at 60°C and agitated by a stirrer and bubbler. A photograph of our apparatus is shown in (b). The beaker containing the electrolyte is submerged in a water bath and agitated with a stirrer and bubbler.

equation [139]

$$h = \left(\frac{\alpha I M}{n F S \rho} \right) t \quad (5.1)$$

where I is the current, $F = 96.5 \text{ kA s mol}^{-1}$ is the Faraday constant, S is the surface area and other parameters with values specific to our gold deposition are: plating efficiency $\alpha \sim 0.9$, the current efficiency; $M = 197 \text{ g mol}^{-1}$ the molar mass; $\rho = 19.32 \text{ g cm}^{-3}$, the density of the deposited metal; $n = 1$, the charge on the deposited ions in units of electron charge.

We therefore have a relationship between the current, the target height and the time,

$$h \sim \left(1 \times 10^{-10} \frac{\text{m}^3}{\text{As}} \right) \times \frac{It}{S}. \quad (5.2)$$

For our electrolytic solution, we have used Metakem Goldbath-SF because it produces very pure (99.99%) deposits, and will not react with our photoresist. The effectiveness of this product has been demonstrated for a similar design in Ref. [46]. Goldbath-SF is suitable for use with current densities in the range 1 mA cm^{-2} – 15 mA cm^{-2} . The final chip design has a plating surface area of 83 mm^2 , and there is an additional contribution to surface area from the clip with which we hold the die in place during plating. We therefore do not know the plating area exactly, but we place the entire clip in the solution every time to ensure the results are reproducible. Estimating the total plated surface area to be $S \approx 1 \text{ cm}^2$, we have an approximate plating rate of $1 \mu\text{m}/100\text{s}$, with the exact rate to be determined experimentally.

Our apparatus for the electroplating step is shown in Fig. 5.5 (b). The electrolytic solution is placed in a beaker, which itself is placed in a water bath held at 60°C . The bath is heated using a hotplate with magnetic stirrer. Some time is allowed for thermalisation, during which it is important that the Goldbath is covered to prevent loss by evaporation. We noted that using a foil cover would result in corrosion on the foil, which could potentially cause contamination of the solution. A glass lid should be used, and care should be taken to ensure that any material placed in the solution will not corrode.

When the Goldbath has reached 60°C the target chip and the cathode are submerged. The chip is held in position by a stiff insulated wire, which also carries current to the seed layer. A multimeter can be used to ensure that there is good electrical contact from the wire to the holder. We use the smallest clip possible so as to minimise additional plating area. The cathode is a grid of platinised titanium which has been cut to the size of our beaker. This was also purchased from Metakem.

A bubbler is placed to agitate the solution near to the chip surface. This in combination with gentle stirring ensures good circulation of the solution and hence

prevents localised depletion of the ions near to the chip surface [144, 145].

After electroplating, dies are rinsed with deionised water, and the photoresist is removed overnight with Dupont 1165 photoresist remover, as illustrated in Fig. 5.1 (8). Dies are then dried and stored for transport to the LCN cleanroom for the inspection and final fabrication steps.

5.5.1 Inspecting the wires

After plating it is useful to inspect the dies under a microscope. This can confirm that the wires have been formed successfully, and that there is continuity along them, but it cannot tell us the height that was achieved during plating. To measure the plating height we use the Bruker DektakXT stylus profilometer.

The stylus profilometer operates by positioning a gold stylus onto the surface of the die and dragging it in one direction. As the stylus comes into contact with features its height will change, allowing a profile of the surface to be measured. Profiling of a surface is illustrated in Fig. 5.1 and is also useful for examining the features after plating.

We determined experimentally that electroplating at 15 mA for duration 400 s reliably produced wires of height 5 μm above the seed layer. A typical example is shown in Fig. 5.6, where we also show a profile of the photoresist mould used to fabricate these wires.

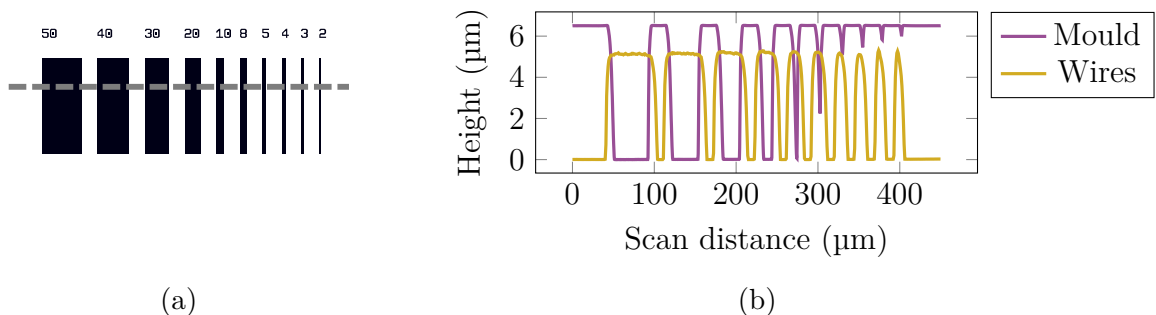


Figure 5.6: Stylus profiling of the characterisation features. In (a) the characterisation lines feature of the chip is shown in detail (c.f. Fig. 3.9) the grey dashed line denoting the profile. Typical profiles are shown in (b), for both the photoresist mould and the plated wires. Stylus size limits the size of the trenches that can be fully profiled, and can make both trenches and hills appear narrower and wider respectively.

Note that when examining the trenches of the mould with the profilometer, we must account for the finite size of the stylus. The profilometer available at LCN is fitted with a gold stylus of radius 5 μm . This limits the resolution of the profile, hence why the trenches in Fig. 5.6 become distorted at and below 10 μm . This

also means that the wires can appear to be wider, and the trenches narrower than actuality, accounting for the overlap in the figure.

5.5.2 Troubleshooting

The electroplating procedure was initially unreliable, but we have developed it into a robust process. It is of use to note some of the complications that we experienced and how they were overcome.

Our first attempt at electroplating was with the underexposed early design photoresist mould shown in Fig. 5.4 (a), meaning that the full wires could not have been formed. These were nonetheless suitable targets for practice. We manually agitated the electroplating solution during plating and were successful in laying down the larger features such as the wire bond pads, but sub $\sim 100\text{ }\mu\text{m}$ features were not formed, as could be seen after removing the photoresist mould. This is shown in Fig. 5.7 (a).

We attempted to improve the adhesion with manual agitation in combination with a bubbler, but eventually found that we achieved the best results with a combination of gentle stirring by a magnetic stirrer in combination with bubbling of the Goldbath. This allowed us to fabricate the smallest features resolvable in the mould. For later attempts at electroplating we ensured the mould had been exposed and developed correctly, such as the one shown in Fig. 5.4 (b). With these moulds we were able to reliably fabricate features below the $10\text{ }\mu\text{m}$ scale.

Next, the photoresist must be removed. We initially attempted this by sonicating in acetone for twenty minutes, however this resulted in the debris visible in Fig. 5.7 (b). It was resolved that acetone was unsuitable and Dow Electronic Materials Microposit Remover 1165 heated to 65°C was used instead. Examples of photoresist removal by this procedure are shown in Fig. 5.7 (c) and (d). Here it can be seen that clear wires have been achieved, but the small wires have been damaged by sonicating. Sonicating can be avoided by instead soaking the dies in the Microposit Remover 1165 overnight at room temperature.

After several iterations of electroplating we found that the larger wires were not uniformly plated, with some areas near the edge seemingly shadowed by the mould as shown in Fig. 5.8. This phenomenon was also noted in Ref. [46], where it is suggested that the only solution is to change to a new batch of Goldbath-SF. Indeed doing this and following the same procedure produced results without this shadowing effect. We noted that the plating rate with the new batch of solution was not consistent with what we had seen previously, suggesting some variation in plating efficiency between batches.

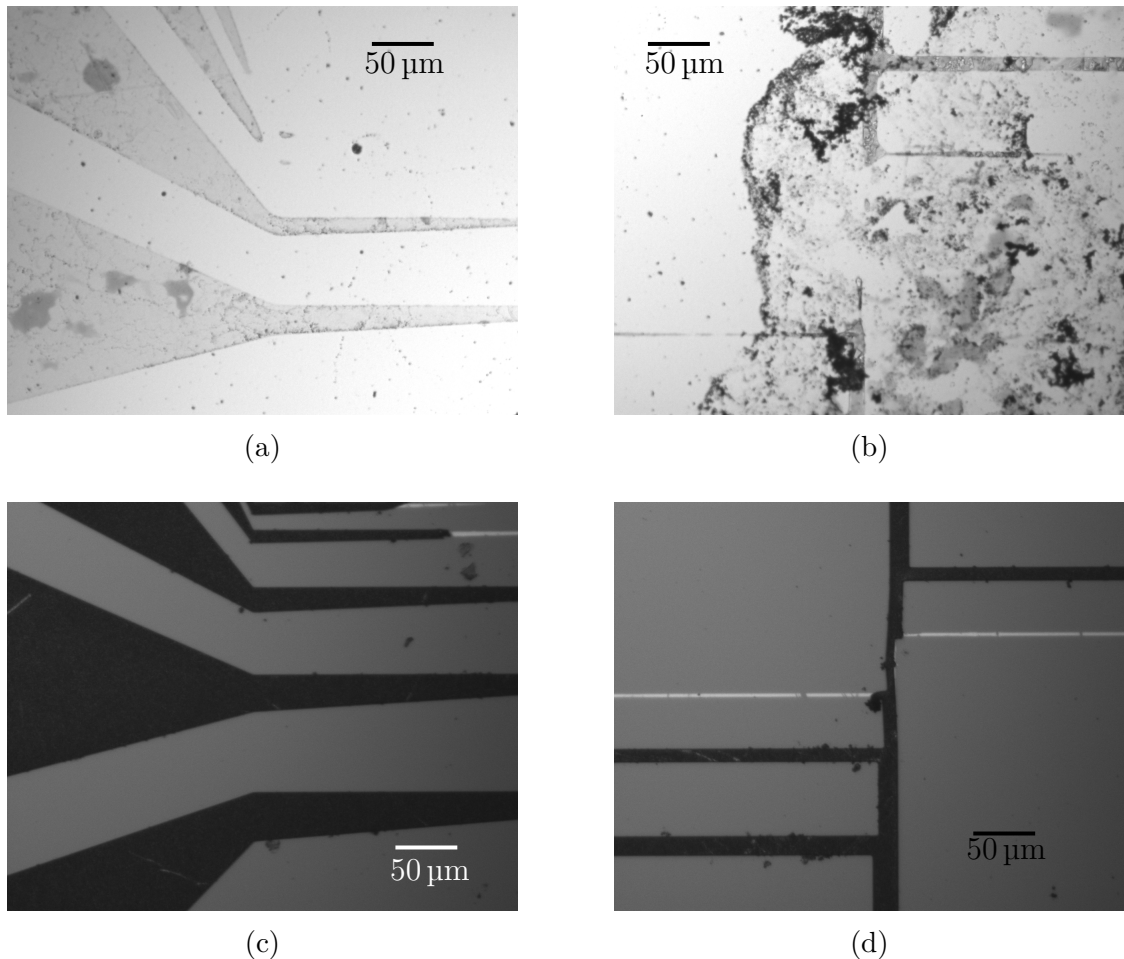


Figure 5.7: Electroplating problems and solutions. Microscope images showing the effects of insufficient agitation (a) and removal of the photoresist with solvents (b) can be compared to later results, where the solution is well agitated during electroplating (c) and the photoresist is removed with Microposit Remover 1165. Subfigure (d) shows the central features of the die same shown in (c), highlighting the damage caused by sonicating. All three dies here have been electroplated at 10 mA for 200 s, and use the early iteration of the design shown in Fig. 5.2.

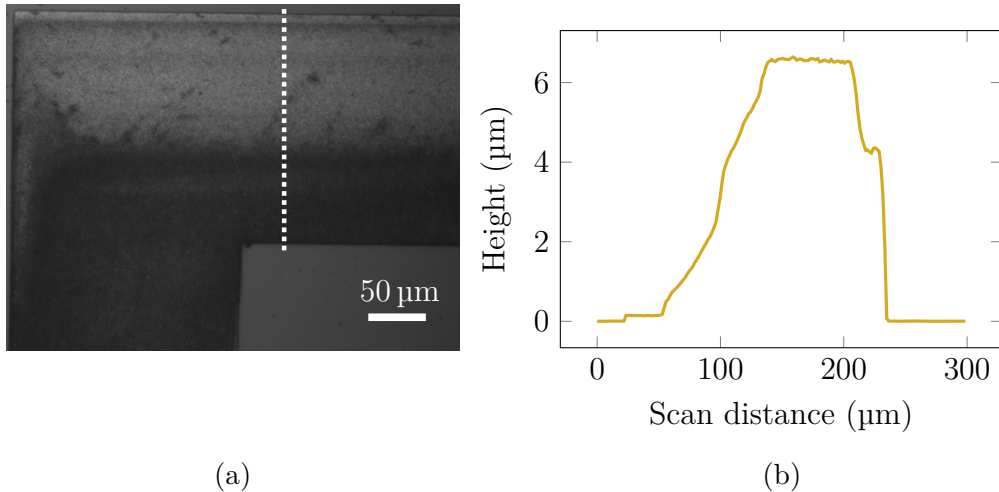


Figure 5.8: The importance of a fresh bath. For large features ($> 50 \mu\text{m}$) we sometimes observe this ‘shadowing’ effect, shown here on the $200 \mu\text{m}$ wire. This can be seen as a gradual gradient on the microscope (a), and confirmed with stylus profiling (b). The profile is taken in the direction and position of the white dotted line shown in (a). Changing to fresh goldbath solution resolves this problem.

5.6 Etching

The seed layer electrically connects the trapping wires, which is essential for electroplating, but it must be removed to separate the wires during operation. We do this by etching the chip to remove the height of the seed layer from the entire surface. Since the seed layer is only a few tens of nanometres and the wires are on the scale of micrometers, the effect of the etch on the wires is negligible.

Any thin films or other debris left on the die can become stuck to the chip during etching, so it is essential to ensure that the die is very well cleaned having been electroplated outside the cleanroom. We found that a solvent clean on its own was insufficient, and would leave some debris on the die after the etch that we could not remove, shown in Fig. 5.9. This was resolved by also cleaning for ten minutes in an oxygen plasma, suggesting that this debris may have been caused by residual photoresist.

After cleaning, the gold is etched away by placing the chip into a beaker of etchant. We used a pre-mixed etchant made up of 50% potassium iodide and 10–20% iodine made by Sigma-Aldrich. This etches gold at a rate of 5 nm s^{-1} , so an etch of duration 5 s–10 s will remove the seed layer. After this the chip is immediately transferred to a beaker of deionised water and then rinsed. Visual inspection of the die will clearly show if the seed layer has been removed.

To complete the separation of the wires, the chromium layer must also be etched in the same way. For this we use another Sigma-Aldrich pre-mixed etchant of 20–25% diammonium hexanitritratocerate and 5–10% nitric acid. The process is the



Figure 5.9: Debris left on the die after etching. It was found that this can be avoided by cleaning with an oxygen plasma for ten minutes prior to etching. Macroscopic view of the entire chip is shown in subfigure (a), where the red box also highlights malformed features due to the photoresist bead. Detail of debris near the wires is shown in the microscope image in subfigure (b).

same as for the gold etch: the chip is submerged in a beaker of the etchant and after 2 s–5 s it is transferred to deionised water and then rinsed. This stage of the fabrication is represented in Fig. 5.1 (10).

We occasionally found that etching could cause some of the smaller features to become detached from the chip, see Fig. 5.10. This could be due to over-etching, or poor adhesion from electroplating. To overcome this we made changes to the chip design, making the central wire larger (the Z2 wire was originally only 4 μm in width) and adding the anchoring pads shown in Fig. 3.9. It is helpful when etching to be very careful with the chip, and hold it in the etchant with tweezers as opposed to dropping it. This ensures that the die can be removed and placed into water without delay – particularly important when the etching time is only a few seconds.

5.7 Inspecting the finished die

To ensure that the etches have been successful, stylus profiling is once again performed. We ensure that the wires are of a sufficient height and width to achieve the required currents as detailed in section 3.2. Visual inspection under an optical microscope is also useful to ensure that the silicon dioxide has been completely exposed. A multimeter is used to confirm that there is continuity across the wires.

5.8 Connection to subchip

To be used in the molecule experiment, the die must be mounted on the subchip described in section 3.2 and electrical connections made. We attempted two meth-

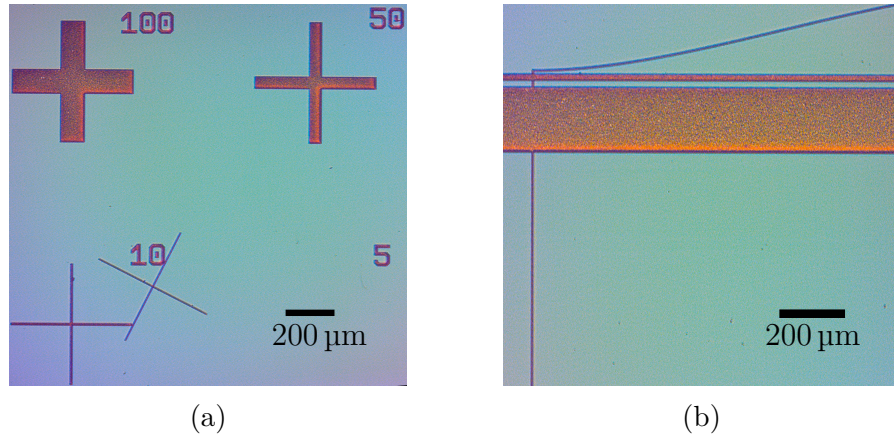


Figure 5.10: Microscope images showing features detached from the chip after etching. In subfigure (a) we can see that a $5\text{ }\mu\text{m}$ characterisation cross has become detached and drifted on to the $10\text{ }\mu\text{m}$ cross. Similarly, the small wire has become detached from the substrate in subfigure (b). This could be due to over-etching or poor adhesion at an earlier stage of the process.

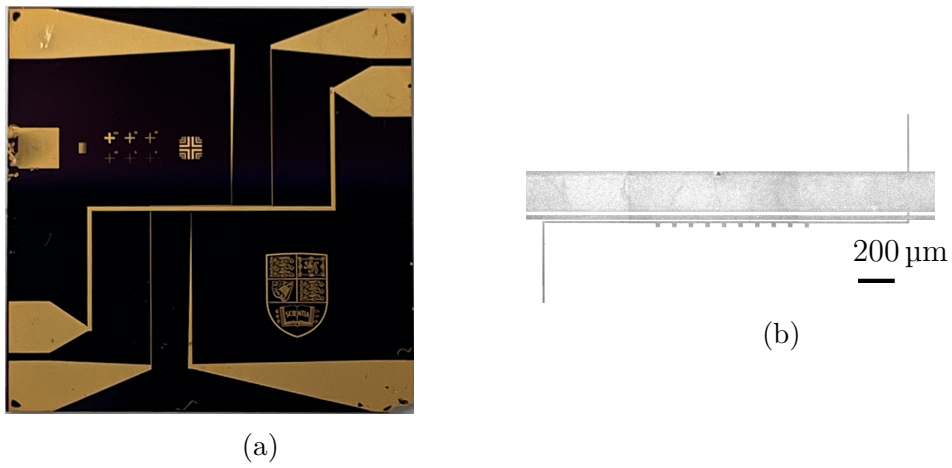


Figure 5.11: Macroscopic (a) and microscopic (b) images of a completed chip. The wires are plated to a height of $5\text{ }\mu\text{m}$ and the profile of the characterisation lines is shown in Fig. 5.6

ods of doing this, first we tried a combination of gluing the die into the subchip and making connections with wirebonds. We later found that the wirebonds failed before reaching the required current, and therefore were unsuitable (see section 6.3). Alternatively it is possible to solder directly between the die and the subchip, in this case gluing is not required to hold the chip in place.

5.8.1 Gluing and wirebonding

For the glue, we use Epoxy Technology H77, a two-component UHV compatible epoxy with good thermal conduction. The two parts of the epoxy are mixed in a five to one ratio by weight using a mass balance, and then a tiny amount is applied to the subchip. Only enough epoxy is required that when the die is pressed onto the surface there will be a meniscus between the surfaces of the die and the subchip.

The epoxy is pipetted into the mounting hole, and the die placed on top. This is followed by pressing in a vacuum bag, evenly pushing the die into the epoxy and helping to remove air pockets in the epoxy, which could result in virtual leaks under vacuum conditions. Finally the chip and subchip are removed from the bag for baking at 115 °C for an hour and left to cool. Vacuum testing of the glue is described in section 6.2.

After gluing the chip into place, an electrical connection can be formed by wirebonding. In this process a thin wire is attached between the subchip and the chip by ultrasonic bonding. An overview of the process is available in Ref. [146]. In our case we used gold wires with 25 µm diameter wires and the Kulicke and Soffa 4523 wedge bonder at LCN. It was possible to reliably produce eight bonds on each pad, which was limited by the width of the pad and the size of the bonding head.

5.8.2 Soldering connections

The second method of connection was to place the die into the subchip and then solder the connection between the traces on the subchip and the wirebond pads on the chip. This was initially attempted with a UHV compatible soldering method. We used colophony-free flux made by Accu-Glass Products, and gold-tin wire from Goodfellow Cambridge Ltd. (80% Au, 20% Sn) as solder. The idea is that the UHV compatible flux can be removed by sonicating in isopropyl alcohol, removing any components that may outgas under vacuum.

We found that using this method it was possible to create good bonds between the chip and the subchip, however doing so was highly unreliable. The solder does not easily flow onto the subchip traces, seemingly because a soldering iron will not heat it sufficiently. We attributed this to the aluminium-core PCB acting as a heat sink, and overcame the issue by using a hotplate to heat the PCB in addition to

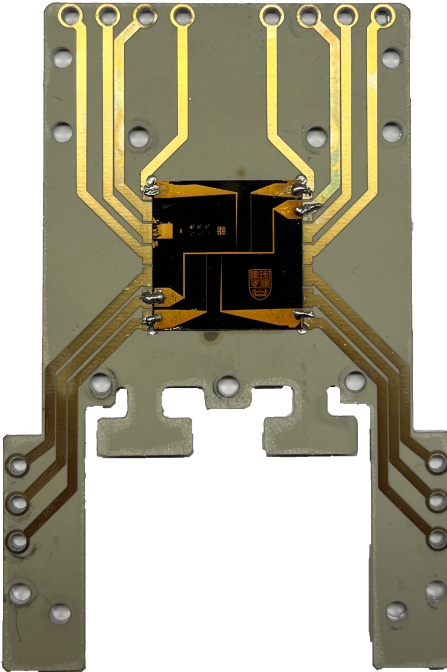


Figure 5.12: The chip mounted and soldered into the subchip.

using a soldering iron. This allowed us to reach sufficiently high local temperatures at the solder joint. However, this had the detrimental effect of causing the wirebond pads on the chip to come loose upon soldering. This only occurred when soldering with the hotplate, so we assume that it was the high temperatures that led to the features detaching from the chip.

Since this was unsuccessful, it was decided to attempt soldering with standard solder from RS Components (60% Pb, 40% Sn with colophony free flux). This was successful, and useful for our initial current testing (see section 6.3). We found that we were able to achieve sufficiently low vacuum without using the special UHV compatible method. Simply soldering with the RS Components solder and cleaning the subchip assembly with IPA was sufficient to reach pressures on the order of 1×10^{-10} mbar, as we will see in section 6.2. The completed chip mounted to the subchip is shown in Fig. 5.12.

5.9 Scaling fabrication

In future design iterations it may be useful to scale the fabrication process up by fabricating on the wafer scale rather than the scale of an individual die. An entire wafer can be metallised, spin coated and exposed to produce the photoresist mask. Electroplating on the wafer scale will take longer, scaling linearly with the number of chips on the wafer. It may therefore be beneficial to use a smaller wafer, and fabricate a few chips at a time. Alternatively, the design could be changed so that

the traps and chips are smaller. Etching would be performed on the entire wafer before dicing into the individual dies.

5.10 Planned fabrication of microwave layer

In chapter 1, we described how a molecule chip could allow strong coupling between CaF molecules and a microwave field, however for this to be possible there must be good overlap between the microwave field and the trapped molecules [2].

This overlap has previously been achieved for atoms in a magnetic trap [46]. An insulating layer is spin coated on to the trapping wires, upon which a CPW can be fabricated by photolithography. The trap centre can be positioned at a resonator antinode, where the microwave field is strongest.

Our fabrication scheme can be extended in a similar fashion. The first stage will be to spin coat the insulating layer on top of an etched chip, as shown in Fig. 5.1 (11). Again taking our lead from Ref. [46], we will use polyimide. Polyimide is chosen due to its low dielectric loss tangent ($\tan \delta_e = 0.016$) which will be discussed further in section 7.1.

When spin coating the polyimide it is essential that we are able to produce a flat surface onto which we can fabricate the microwave layer. We can do this by applying multiple layers of polyimide on the spin coater, so that any bumps are smoothed out. This is known as planarization and is discussed further in Ref. [138]. We expect this coating to have a thickness between 1 and 10 μm .

After the application of a planarized polyimide layer it will be possible to fabricate microwave guides on the surface by lithography. The end result is shown in Fig. 5.1 (12). We will undertake further work to determine the required height of the CPW features and where they must be positioned relative to the wires to achieve the strongest coupling. We will discuss in chapter 7 that for a microwave resonator we must fabricate the CPW with a superconducting material, or else the quality factor will be too low due to resistive losses. The fabrication of superconducting CPWs is a well developed field, and is discussed in for example Ref. [147].

Chapter 6

Preliminary experiments

The chip apparatus was assembled for preliminary tests, but isolated from the main CaF experiment. This setup was useful for a variety of measurements, which will be discussed below, including vacuum compatibility, current testing under vacuum, and looking at the amount of background scatter from the apparatus during imaging. We anticipate background scatter to be a significant challenge in an experiment close to a surface, and discuss possibilities for a background-free imaging scheme in section 6.5.

6.1 Experiment assembly

In this section I give details of the apparatus, especially the chip flange assembly, which was introduced in section 3.2. The flange assembly is designed to hold the chip in position for loading CaF, whilst also providing current delivery and heat sinking. Considerations have been made for future experiments using microwaves, with two high-frequency microwave feedthroughs incorporated as well. The flange was manufactured by Allectra GmbH, and the heat sink was machined in the CCM workshop; I was responsible for the assembly of the apparatus. A detailed view is shown in Fig. 3.10.

The copper heat sink is mounted to the flange using screws where the thread has been partially removed. This is done to prevent any trapped gas causing virtual leaks inside the chamber. The heat sink supports the subchip and also incorporates the large U-trap, which is recessed beneath the chip. It is electrically isolated from the heat sink by AlN plates. This material is chosen since it is an electrical insulator, but a good heat conductor, allowing the conduction of heat away from the U-wire whilst being UHV compatible. The subchip is attached to the heat sink with metal screws. For the PCB we choose an aluminium-core PCB to ensure good heat transfer away from the chip. This initial version, shown in Fig. 3.11, does not include microwave guides. A future version incorporating these should be made of a material suitable

for use as a waveguide dielectric (see chapter 7). Since the conductor tracks come very close to the mounting holes, we isolate the screws from the surface using washers made from polyimide (another UHV compatible insulator) which were manufactured in the CCM workshop.

The current is delivered to the U-wire through two high-current feedthroughs. For the chip currents, the 16-pin feedthrough is used, and is connected to the subchip by kapton-coated wires from LewVac. When connecting the wires to the subchip we use polyimide bushings (also made in the CCM workshop) to ensure that they are electrically isolated from the aluminium core of the PCB.

The flange is mounted in the chip chamber, which is a DN63 cube chamber from Kurt J. Lesker Co. (KJL) and whose configuration is shown in Fig. 6.1. The assembly is designed so that molecules will enter the chamber along an axis that is 3 mm from the surface of the chip. A tee is installed to allow for additional vacuum ports whilst still allowing a clear line of sight across the chip surface. The direction of the line of sight is shown in the figure by the pink arrow, and passes through the anti-reflection coated viewports which also from KJL. This provides optical access across the surface of the chip for illumination. Onto the tee we attach a Agilent TwissTorr 84 FS turbo pump, backed by a scroll pump (not pictured). There is also a DN63-DN40 adapter opposite the chip flange. This will be where the chamber is attached to the CaF experiment in the future, but for testing purposes a pirani gauge or Leybold residual gas analyzer (RGA) is attached instead.

The optical access allows for two main styles of imaging experiment. In both, a laser beam will enter through the viewports as shown in Fig. 6.1 (a). Light-induced fluorescence can then be imaged by collecting the light along this axis. This would allow measurement of the changing height of molecules that are released from the trap as they fall under gravity. An alternative arrangement is shown in Fig. 6.1 (b), where light is collected from a viewport beneath the chip and imaged onto a CCD. This may be useful since it avoids imaging along the path of the light driving the transitions and could reduce background scatter. We anticipate background scatter to be a significant problem for an experiment that is conducted close to a surface, and this issue will be discussed further in section 6.4.

6.2 Vacuum testing

For testing the vacuum compatibility of the components, the RGA is attached to the chamber. This is useful for diagnosing leaks and outgassing in the chamber. To reach UHV pressures, it is required to bake the experiment. Heater tape is applied and the chamber is wrapped in foil, the temperature is then raised over the course of a few hours to just over 100 degrees Celsius. It is held at this temperature for at

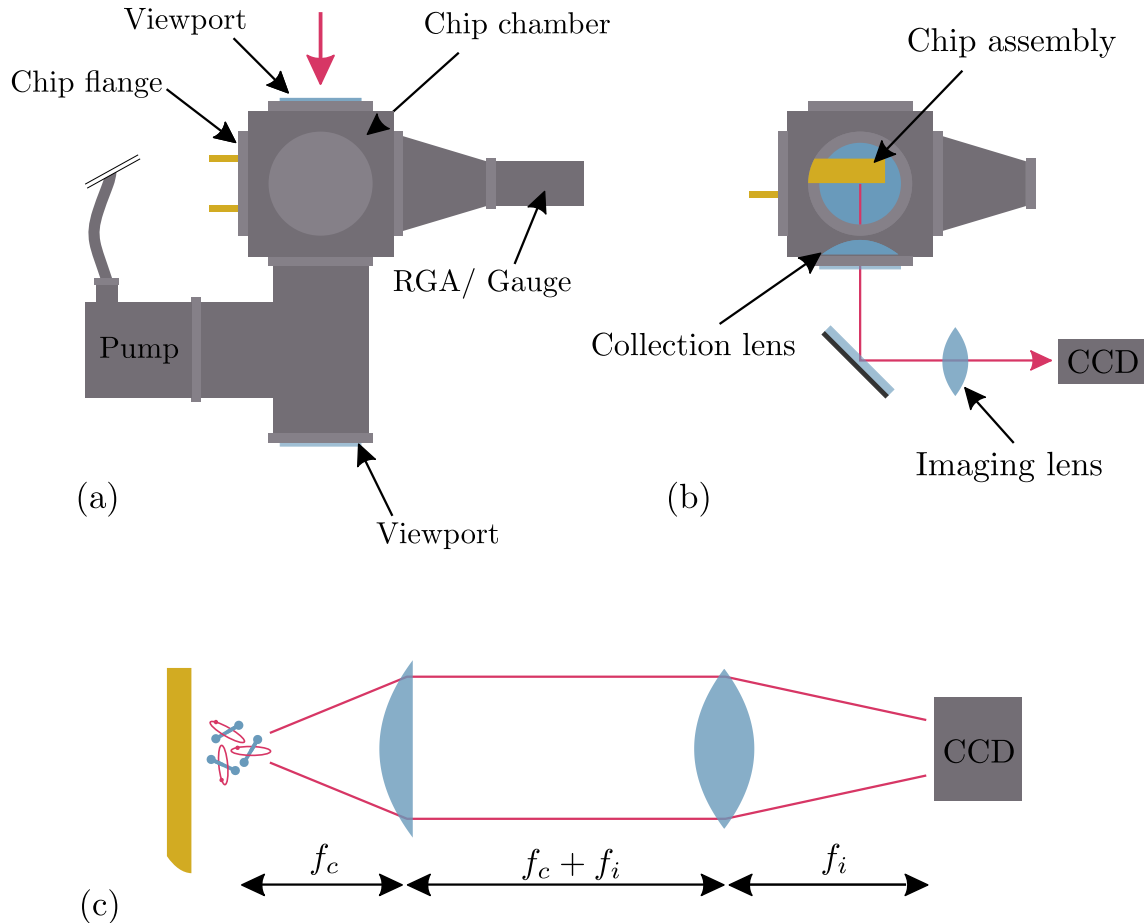


Figure 6.1: A top-down (a) and profile (b) view of the chip experiment. In (a) we show the line of sight through the chamber by the pink arrow. In (b) we show a view as if looking through the viewport on the tee, and also highlight the position of the collection lens inside the chamber. Here the pink arrow denotes the path of light collected for imaging from beneath the chip. The imaging system is shown unfolded (without the mirror) in subfigure (c), with f_c (f_i) denoting the focal length of the collection (imaging) lens.

least 48 hours, before being ramped back down. This removes excess water vapour from inside the chamber, and expels any water that has been absorbed into the chamber walls. The exact parameters of the bake are recorded, but it was found that following this approximate procedure was sufficient for our purposes.

The chamber was first leak checked [148] and then brought to UHV pressure with the chip flange assembly replaced with a blank. This provided a baseline pressure for the chamber. We then swapped in the flange assembly, and repeated the bakeout process with various iterations of our design. In our design process we were careful to choose materials that are UHV compatible but it was important to check that the assembly could reach the pressures required. In particular we were concerned with the Epoxy Technology glue, since any errors in the mixing and application procedure could cause outgassing, and the solder, which was not rated for UHV uses.

To measure the pressure of the chamber an RGA scan is undertaken, with the resulting partial pressures shown with and without the chip assembly in Fig. 6.2. The total pressure (the sum of the partial pressures) is 5.0×10^{-10} mbar in the first case and 8.8×10^{-10} mbar in the second. The scan with the chip assembly has a similar shape to the empty chamber scan, but with slightly higher values. In both, we see the typical peaks for H₂ (2), water (18) and N₂ (28), which dominate the spectrum. This is typical of a scan through a UHV system [148], and suggests that the chip assembly does not introduce any sources of contamination or outgassing into the experiment. Further tests were conducted when using a chip with wirebonds rather than solder, and the microwave barrel connectors and launchers (see section 7.2.3) which will be required for future experiments. These yielded similar results to those discussed above, with no discernible change in the pressure. It is likely that lower pressures could be reached using a longer or hotter bake. However, the pressure obtained here is already sufficient for trapping molecules for several seconds. At this point, the lifetime becomes limited by vibrational heating of the molecules from black-body radiation at room temperature.

6.3 Current testing

It was also important to test the currents that can be achieved through the chip trapping wires. These tests were conducted with the chip under vacuum ($P < 10^{-6}$ mbar) and using the setup shown in Fig. 6.3, which was used since our custom current drivers were not ready at this stage (although I will describe the concept behind them at the end of this section). It is important to test the current in the wires in pulses, with a duty cycle resembling what will be required in the trapping experiment where the trapping wires will be switched on for a few hundred milliseconds, a few times every minute. This repetition rate being limited by the speed of the

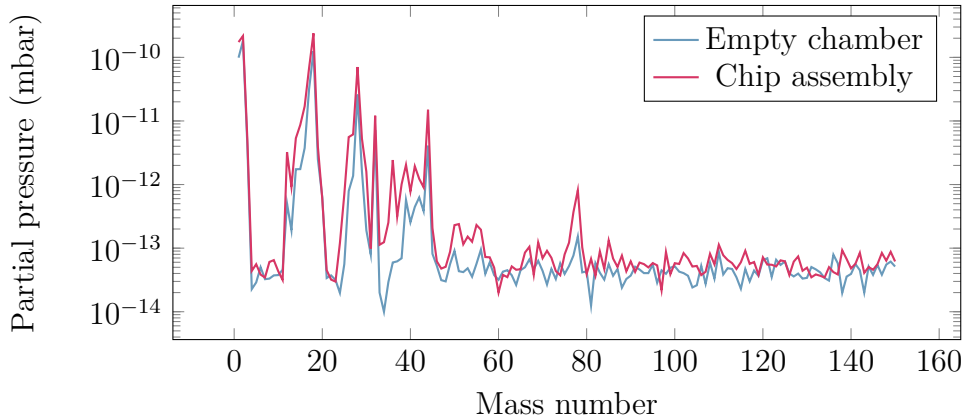


Figure 6.2: RGA scan of the chip chamber assembly when empty, and when loaded with the chip flange assembly.

transport coils. For this reason, a regulated power supply at voltage V_{PSU} is used to induce a current in the chip wires, with this current is controlled by the FET circuit that is in turn switched by a signal generator. This allows control over the pulse length, and for the delivery a voltage drop of V_{PSU} up to 30 V across the chip, since the sense resistance (R_{sense}) is much larger than the load resistance from the wires (R_{load}).

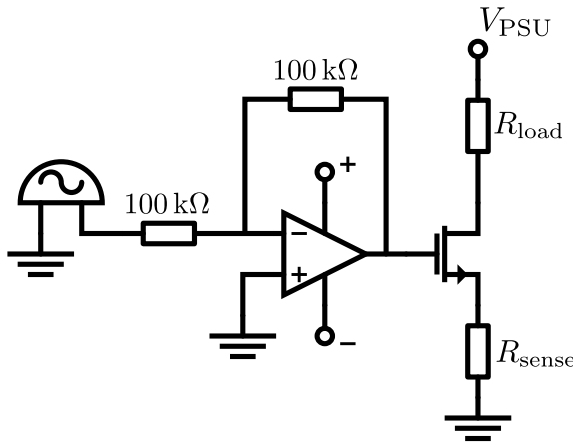


Figure 6.3: The electronic circuit used to test the chip wires. The chip is represented by resistor R_{load} . The operational amplifier is powered by a separate power supply. This figure was produced using the assets from Ref. [149].

6.3.1 Wirebond tests

We originally tested a number of designs where the chip was connected to the subchip with wirebonds using the method described in section 5.8.1. In these cases it was found that the wirebonds were unreliable at high currents. It was possible to achieve pulses of several amperes through even the small wires, but these were not reliably repeatable, and often resulted in the wirebonds being broken.

These tests were conducted using a 200 ms pulse of current, repeating every 10 s. The supply voltage was ramped up gradually, and the current through the chip was measured via the potential difference across the FET controller's sense resistor (see Fig. 6.3). Several iterations of chips (with varying wire heights) were tested, using all trapping wires. However no meaningful results for maximum attainable current were found, as invariably the wirebonds would fail. This was established by a visual inspection of the chip, and checking the electrical continuity across the trapping wires and from the subchip to the chip.

We attempted to improve the maximum current by increasing the number of wirebonds on each pad, and by improving the quality of the wirebond joints. We found that the former yielded an improvement to the maximum current capacity, but the quality of the wirebond joints was difficult to quantify. As a rule of thumb, the wirebonds were re-done if they could not withstand a light tug from a pair of tweezers. Ultimately the number of wirebonds that it was possible to produce was limited by the width of the wirebond pad, and the width of the wirebonder head. We could achieve approximately ten wirebonds per pad somewhat reliably.

There are various options that could be used to increase the maximum current of the wirebonds. We considered using a ribbon wirebond, which promises larger current throughput by using a ribbon-shaped wire rather than a round one. This was not possible due to the unavailability of the hardware at LCN. Another option was to use higher-diameter wire, but this was unavailable so instead we attempted to directly solder the chip, as described in the next section.

6.3.2 Solder tests

An alternative to wirebonding is to directly solder the chip to the subchip. This must be done carefully, as described in section 5.8.2 but if done correctly it yields a highly stable electrical connection. In the next section I will demonstrate that this method is compatible with UHV. Current tests were performed with the same apparatus as for the wirebonded chips, as shown in Fig. 6.3. For solder joints, the results were reliably repeatable, and we were able to observe sufficient current densities for trapping (comparable to those laid out in section 3.2).

We consider a typical example of testing using the small wire (width 9 μm), on a chip where the wire height achieved was 9 μm . Again, the current was pulsed on for 200 ms once every 10 s, which we imagine to be representative of a typical experiment. We show the current through the chip as a function of supply voltage in Fig. 6.4 (a). Also shown is a linear fit to the first ten data points. We observe here that for low voltages, the current obeys Ohm's law, as we would expect, but this diverges for higher voltages, suggesting that heating occurs in the device.

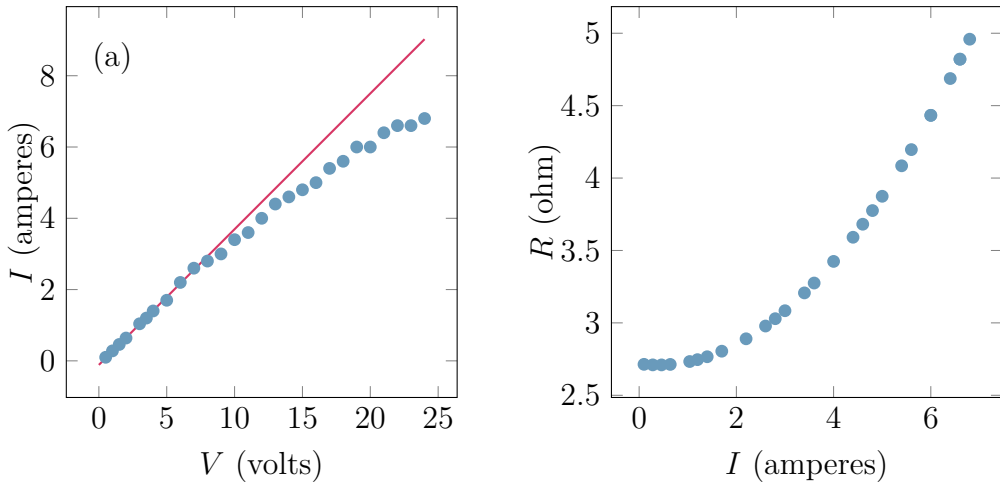


Figure 6.4: Increasing current in the small chip wire. The current is shown as a function of supply voltage in (a). The pink line shows a linear fit to the first ten points. In (b) this is converted into a resistance (as described in the main text), which increases for higher currents.

Nonetheless, with sufficient voltage it is possible to achieve currents of 6.8 A, which corresponds to a current density of $j = 6.8 \text{ A}/(9 \mu\text{m} \times 9 \mu\text{m}) = 8.4 \times 10^{10} \text{ A m}^{-2}$. This is slightly higher than was expected (see again section 3.2), and potentially not the maximum current density achievable. This is probably because the current was not continuous but instead pulsed with a low (but realistic) duty cycle. We did not test this chip to the point of failure as we wanted to preserve it and the required current for trapping had already been met.

Further, the resistance of the chip as a function of current can be found by fitting a third order polynomial to the IV curve in Fig. 6.4 (a), and taking its derivative. This derivative approximates the chip's conductance at that voltage and current, the resistance is found by taking the reciprocal of this conductance, and the result is shown in Fig. 6.4 (b). The resistivity scales proportionally to the temperature, and so it can be deduced that the doubling of the resistance corresponds to a doubling of the temperature from room temperature to around 550 K. This suggests that the wire is operating below the point of failure, which we might anticipate to occur when the operating temperature reaches the melting point of gold (1300 K).

6.3.3 Wire failure

During testing of another chip, we were able to pass sufficient current to destroy the small wire, although this was during an early stage of the tests and so the current at which this occurred was not properly recorded. However it is useful to be able to distinguish a good wire from one that has been destroyed by heating. These are shown in Fig. 6.5 (a) and (b) respectively.

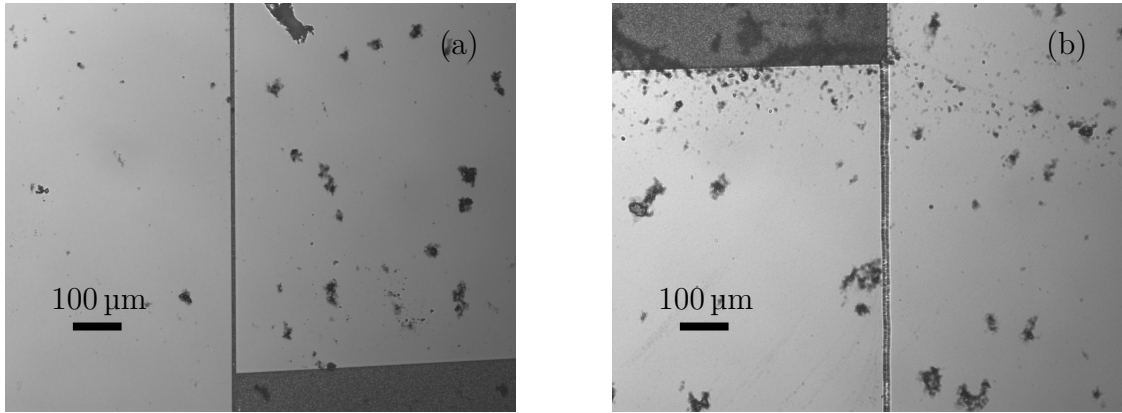


Figure 6.5: A wire before (a) and after (b) destruction due to fusing under extreme current load. Note that the clearly defined edges and solid colour have changed to a wobbly and poorly-defined region. In both subfigures , part of a fanout is also visible.

6.3.4 Current driver concept

One problem that I have not yet expanded on is how exactly we intend to control the currents on the surface of the chip in the main experiment. There is not an obvious solution to this since, as we have explained above, the trapping wires are fabricated on a single level and are all electrically connected to each other. The challenge is to regulate the trapping currents so that any two wires can be ramped on and off independently of each other. A solution was developed by Ben Sauer and Noah Fitch of CCM, and is illustrated in Fig. 6.6. One unwanted path of higher resistance is allowed, and should be eliminated in a future design.

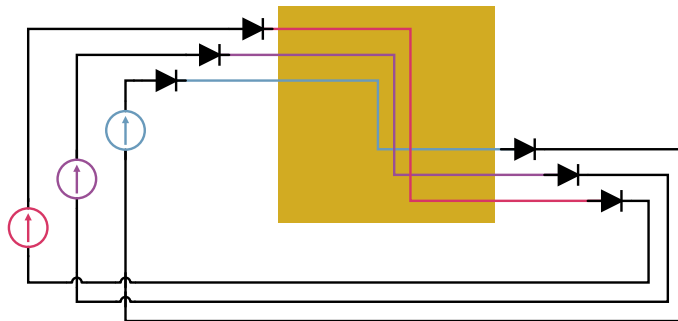


Figure 6.6: A circuit diagram showing the concept for controlling currents in electrically connected chip wires. The current in each trapping wire (blue, pink and purple) is controlled by its own dedicated current driver (correspondingly coloured), and isolated from the others by diodes. The gold square denotes the chip, where the wires will be electrically connected.

In this concept, the current in each wire is controlled by a dedicated current driver. Each of these current drivers is isolated from the other wires by the use of diodes positioned at either end of the trapping wire. This system is represented in the figure by a series of Z-trapping wires colour coded to match their respective

current driver. The wires are connected on the chip, denoted here by the gold square. The current drivers themselves can be configured for arbitrary usage, but should be controlled via an input voltage for use with the existing CaF experiment control software.

6.4 Scatter testing

In the existing CaF experiment, the molecules can be imaged by light-induced fluorescence. The $X(v = 0) \rightarrow A(v = 0)$ transition is driven by \mathcal{L}_{00} along with the vibrational repumps, and light is emitted as the molecules spontaneously decay from A back to X . Most molecules will decay back to $X(v = 0)$, releasing a photon at the same wavelength as the laser, which can be collected and imaged on a CCD camera. Since the laser and fluorescence are at the same frequency, any light scattered from the viewports or from nearby objects, such as the quadrupole coils, will create a background that must be accounted for in post-processing. Various steps are taken to reduce this background, which would otherwise obscure any signal. Most notably the internals of the chamber are painted black to reduce reflections. However it is not clear whether it will be possible to blacken the chip without compromising its capacity to operate. We also anticipate that scatter will be worse near the chip than in existing experiments since it is highly reflective.

To investigate this issue, the imaging scheme shown in Fig. 6.1 (b) was configured in the same way that will later be used to image molecules. A plano-convex collection lens with a focal length of 26 mm and diameter of 2 inch was installed inside the chamber. This high numerical aperture lens was chosen to collect as much light from the molecules as possible. This is then imaged onto a Hamamatsu ImagEM X2 EM-CCD camera C9100-23B using a second biconvex 100 mm-focal length imaging lens, in the configuration detailed in Fig. 6.1 (c). The EM-CCD camera is chosen to be able to achieve large gain for small signals on individual pixels. We use 100 ms exposure and 2×2 binning of the pixels.

Although we do not have access to molecules, we can still shine the laser across the chip and observe the background scatter. We do this for various positions of the beam with respect to the chip surface, controlling the height with a micrometer screw gauge. Five images were taken at each beam position, from which we subtracted a background image taken with the laser light off, and then calculate the number of laser photons scattered onto the EM-CCD using the equation

$$\text{photon number} = \frac{N_{\text{px}} k}{G_a G_{\text{EM}} \eta}, \quad (6.1)$$

where N_{px} is the pixel value, $k = 2.2$ is the conversion factor in CCD mode for our

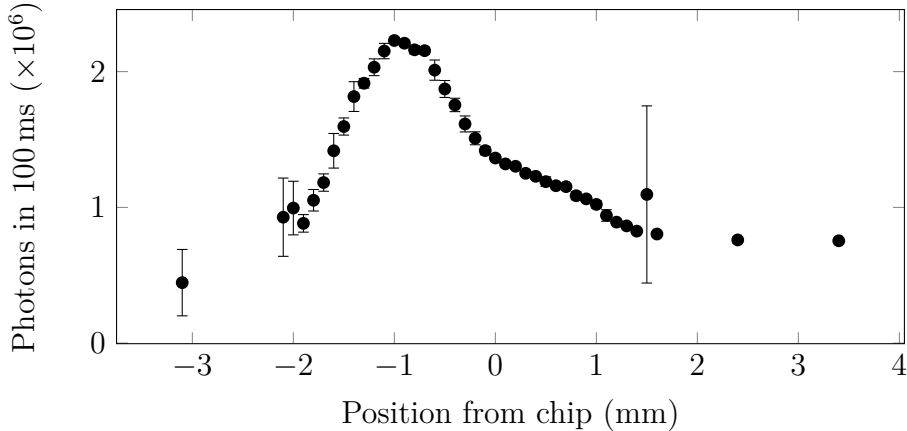


Figure 6.7: Background scatter normalised for a 10 mW beam for various distances from the chip surface. Positive is away from the chip, negative is into the heatsink.

camera, $G_a = 1$ is the analogue gain, $G_{EM} = 1$ is the EM gain and $\eta = 0.95$ is the quantum efficiency of the detector¹.

The beam $1/e^2$ diameter is chosen to be 500 μm , and we normalise the number of scattered photons produced for a beam with power 10 mW, such as may typically be used in an experiment. The results are shown in Fig. 6.7, where we have defined the positive direction to be below the chip’s surface. The shape of the curve indicates that the most scattering occurs when the laser strikes the heat sink, but of most interest to us is that the scatter is significantly higher than we would observe when imaging in, for example, the existing MOT chamber.

In the existing experiment, the number of background photons detected in 100 ms due to the scatter from a 10 mW beam is about 10^3 . To reduce the number of background photons, a background-free imaging scheme has been investigated, as is discussed in the next section.

6.5 Background-free imaging

One possible method of reducing background whilst imaging molecules is Raman Resonance Optical Cycling (RROC), a background-free imaging scheme recently proposed and demonstrated using SrF in Ref. [150]. In this scheme, off-diagonal ($v \neq v'$) vibrational transitions are driven to excite the molecule, which will decay primarily on the diagonal ($v = v'$) transitions. The off-diagonal transitions are separated from the diagonal ones by > 10 THz, and so it is possible to use a bandpass filter to exclude the imaging light from any measurement. For an ideal bandpass filter this would remove any background from imaging light scattered by the apparatus.

¹The dark value offset of the camera is accounted for by the background subtraction.

This scheme is shown for CaF in Fig. 6.8, where the \mathcal{L}_{01} and \mathcal{L}_{10} light is used to drive the transitions at 585 nm and 628 nm respectively (see Table 3.1). Fluorescence from the decay on the 606 nm transitions $v' = 0 \rightarrow v = 0$ and $v' = 1 \rightarrow v = 1$ is isolated by a bandpass filter, and can be imaged without the usual background scatter. The filter used here is a Semrock FF01-605/15-25, which allows light of wavelength 605 ± 15 nm to pass through it with 95% efficiency.

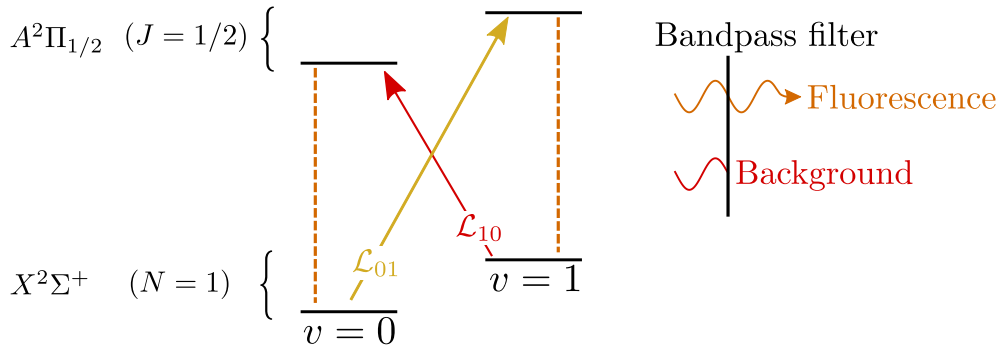


Figure 6.8: The RROC scheme for CaF. An optical cycle is established, with pumping on the $v = 0 \rightarrow v' = 1$ (gold) and $v = 1 \rightarrow v' = 0$ (red) transitions. Fluorescence from the $v = v'$ transitions (orange) is distinguished from the background by a bandpass filter before imaging.

Reference [150] reports a suppression of scattered light by a factor of $\sim 10^6$, and an average emission of 20 photons per molecule. In this experiment, a beam of molecules was imaged, and this emission is limited by the interaction time during travel. For imaging a stationary cloud of molecules we would expect instead to be limited by the reduced scattering rate in the off-diagonal transitions. In this section I will describe the technique, and describe experiments conducted in a beam and in the MOT chamber.

6.5.1 Scattering rate and power requirements

We saw in section 2.1 that the scattering rate for a molecular transition is saturated for sufficiently high intensity $I > I_s$, where the saturation intensity

$$I_s \propto |\langle g | \mathbf{d} \cdot \boldsymbol{\epsilon} | e \rangle|^{-2}. \quad (6.2)$$

We further note that this matrix element is proportional to the square root of the Franck-Condon factor of the transition (this will be discussed further in the following paragraphs), so that

$$I_s \propto \frac{1}{q_{v',v}}. \quad (6.3)$$

The relevant Franck-Condon factors in CaF are

$$q_{0,1} = 0.03, \quad (6.4)$$

$$q_{1,0} = 0.015, \quad (6.5)$$

$$q_{0,0} \approx q_{1,1} \approx 1. \quad (6.6)$$

This means that the saturation intensity for the off-diagonal transitions is a factor of approximately 100 higher for these off-diagonal transitions. It is noted in Ref. [150] that corresponding higher laser power is required to implement the RROC scheme than the usual direct imaging scheme.

Hence, our initial experiments take place in the regime where the scattering rate is given in the $s \ll 1$ limit,

$$R = \frac{\Omega^2}{\Gamma}. \quad (6.7)$$

To calculate this scattering rate we must evaluate Ω , which was defined in eqn (2.4), and is reproduced here for clarity

$$\hbar\Omega = \langle g | \mathbf{d} \cdot \mathbf{E} | e \rangle. \quad (6.8)$$

This evaluation can be performed as follows, first take the orientation of the molecule to be random with respect to the light field, so that the dot product averages across the ensemble to give $dE/3$. Next, we consider the matrix element $\langle g | d | e \rangle$ as was discussed in section 2.3.2. For our transition this term will consist of three factors, an electronic factor ($d_e = 6 \text{ D}$), a vibrational factor (the square root Franck-Condon factor $q_{v',v}$) and a rotational part (approximately $1/\sqrt{3}$), so that

$$\langle g | d | e \rangle \approx d_e \sqrt{\frac{q_{v',v}}{3}}. \quad (6.9)$$

Additionally we use eqn (2.8), to find that the excitation rate is

$$R \approx \frac{d_e^2 q_{v',v}}{81 \hbar^2 c \epsilon_0 \Gamma} I. \quad (6.10)$$

For the $0 \rightarrow 1$ transition, eqn (6.10) yields $R \approx 100 I \text{ s}^{-1}$, with I in W m^{-2} . For the $1 \rightarrow 0$ transition, the coefficient is half of this. To saturate the transition, the excitation rate should be close to the decay rate Γ , so we need an intensity of about 10^6 W m^{-2} . Taking a beam with a radius of about 0.3 mm, which would be needed to detect molecules released from the chip, we see that a laser power of about 300 mW is needed

I will now discuss two preliminary experiments to investigate the RROC scheme in CaF: identifying the transition in the CaF beam using a narrow laser beam waist,

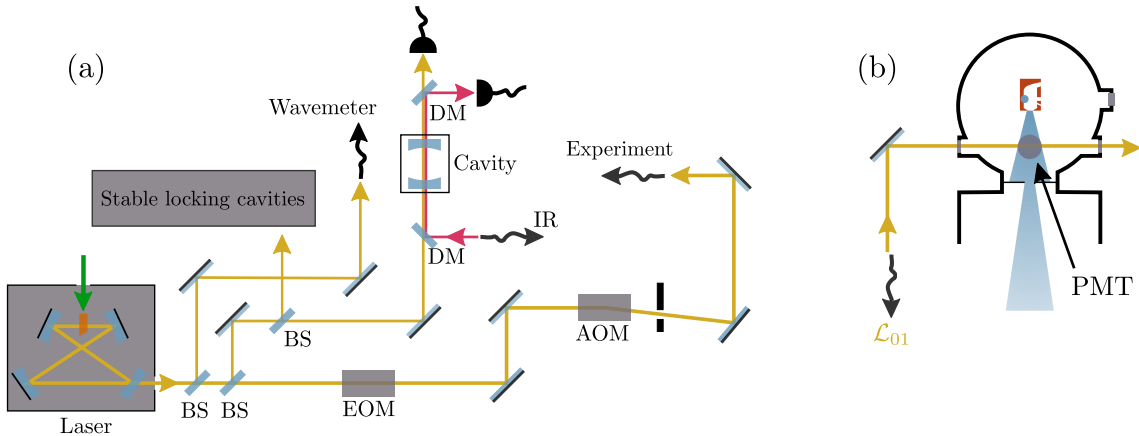


Figure 6.9: The optical (a) and vacuum (b) setup for the spectroscopy experiments. The dye jet (orange) is pumped (green arrow) to produce \mathcal{L}_{01} (yellow arrow). Beam-splitters (BS) are used to generate pick offs from the main beam. These are used for locking to the reference cavities, analysis with the wavemeter and comparison to IR light (pink arrow). The latter of these is achieved using the dichroic mirrors (DM) and the scanning cavity as described in the main text. In (b) the buffer-gas source and CaF beam are shown (c.f. Fig. 3.1). The \mathcal{L}_{01} light is incident on the beam to induce fluorescence, which is detected with a PMT, mounted above the beam (out of the page).

and imaging the CaF cloud in the MOT chamber with a 5 mm $1/e^2$ diameter waist.

6.5.2 Identifying the transition frequency

In this first experiment \mathcal{L}_{01} was used to identify the $X(v=0) \rightarrow A(v=1)$ transition frequency. A pulsed beam of CaF was addressed with \mathcal{L}_{01} , with the laser frequency scanned between pulses. When the laser is at resonance it drives the transition and light-induced fluorescence can be observed. The apparatus is shown in Fig. 6.9, with subfigure (a) showing the layout of the \mathcal{L}_{01} laser system. The light passes through an electro-optic modulator, which is used to add the sidebands for addressing the hyperfine structure of the $X(v=0)$ state, and an acousto-optic modulator (AOM) which is used for switching the light on and off. In this experiment the EOM is switched off, and the AOM is not installed as switching is not required. There are various pickoffs for measuring the frequency of the light, as will be detailed below.

The \mathcal{L}_{01} laser used for the following experiments is the Spectra Physics 380D, a single frequency ring dye laser, using Rhodamine 6G dye and pumped by a Spectra Physics Millenia EV, a continuous wave diode-pumped solid state laser. The power output from the 380D at 585 nm is approximately 300 mW.

The laser frequency is locked by the Spectra stable lock cavities. These consist of one reference cavity and one scanning cavity. The light passes through these and is measured on a photodiode. This signal is fed back to the laser to control

the cavity length and the laser frequency. This provides stabilisation down to the 10 MHz level. For more precise locking of the laser frequency, we reference \mathcal{L}_{01} to a 780 nm laser, which is in turn locked to a saturated absorption feature in a Rb vapour cell, specifically the $F = 2 \rightarrow F' = 2, 3$ cross-over feature of the $^{87}\text{Rb} D_2$ line. The frequency offset lock used to achieve this is described in Ref. [97]. This infrared (IR) reference light is combined with the \mathcal{L}_{01} beam using a dichroic mirror (DM). This beam is then passed through a scanning cavity, before being split into the two frequency components on a second DM. We then observe the relative location of the transmission peaks across the cavity scan, and can use a feedback loop to lock the dye laser to the reference laser. This method keeps the laser stable to within 1 MHz. The absolute frequency can be read from a wavemeter with 600 MHz precision.

A buffer-gas source was used to produce the pulsed CaF beam. This experiment was undertaken on a separate CaF source to the one used on the main beamline that was described in section 3.1, but it is functionally identical. The beam was driven by \mathcal{L}_{01} with $1/e^2$ diameter 500 μm and power 100 mW. Light-induced fluorescence was collected by a lens onto a photo-multiplier tube (PMT) mounted above the beamline, as shown in Fig. 6.9 (b).

The laser frequency was scanned from 512.0725 THz to 512.0750 THz in 25 MHz intervals. At each frequency the total signal on the PMT is measured, using the Semrock bandpass filter to remove background signal. This is shown in figure 6.10, where we can see that there are two clear peaks. We interpret the large peak to be due to resonance with the $F = 0, 1^+$ and 2 hyperfine levels, which we cannot resolve individually (see Fig. 3.2). We attribute the second peak to the $F = 1^-$ hyperfine level. This confirms that we are capable of resolving the new transition that is required for the RROC scheme.

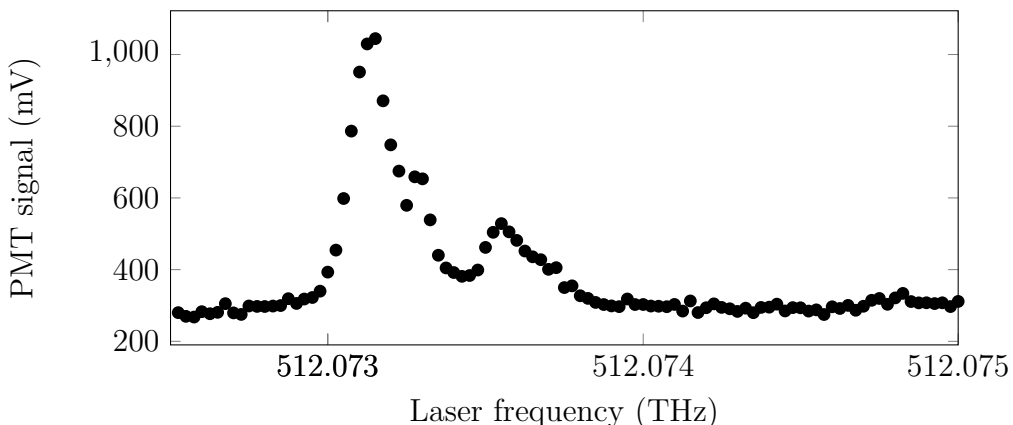


Figure 6.10: Laser-induced fluorescence signal from \mathcal{L}_{01} incident on a CaF beam. The signal is measured by a PMT.

6.5.3 Attempt to image the CaF cloud

Having identified the $X(v = 0) \rightarrow A(= 1)$ transition frequency, we attempted to use the RROC scheme to image a cloud of CaF molecules in the MOT chamber which was described in section 3.1. The molecules underwent the usual slowing procedures, also described above, to create a $50 \mu\text{K}$ cloud with $1/e^2$ diameter of approximately 3 mm. The cloud is then imaged by using a combination of the \mathcal{L}_{01} and \mathcal{L}_{10} light.

We again use the \mathcal{L}_{01} system described above and shown in Fig. 6.9 (a), but with the EOM now turned on and overdriven. This produces the required sidebands to address each hyperfine state of $X(v = 0)$ (see chapter 3 and for example Ref. [83]). In addition the AOM is installed and used to switch the beam on and off. When powered, the majority of the beam is deflected into the first order mode of the AOM, which is coupled into a fibre and brought to the experiment for imaging. Otherwise the beam passes straight through the centre of the AOM and is blocked. At the chamber, the beam is expanded to 5 mm $1/e^2$ diameter and passes through the centre of the chamber before being retro-reflected to increase the power delivery and avoid pushing molecules with the beam. The \mathcal{L}_{10} light is provided by the molasses beams.

In this experiment we create a MOT, and then switch off the magnetic field to create a molasses. We hold the molecules in the molasses for 20 ms, during which time an image of the fluorescence is taken using a Hamamatsu Orca R2 CCD camera. The exposure time is 10 ms, following which \mathcal{L}_{00} is switched off, and \mathcal{L}_{01} is switched on along with a 1 G magnetic bias field. The direction of the field is chosen to ensure that the molecules are not pumped into a state that is dark to \mathcal{L}_{01} , which could otherwise occur due to the light's polarisation. A second 10 ms exposure is then taken with the camera to image the fluorescence in the RROC scheme.

Due to expanding the beam to a much larger diameter (5 mm as opposed to 500 μm), the intensity of the light is a factor of 100 lower than in the previous experiment. Despite scanning the frequency of \mathcal{L}_{01} across the same range as before, it was not possible to drive the transition sufficiently for imaging. This result was somewhat anticipated since, as was reported in Ref. [150], much higher laser power is required for the RROC scheme than in conventional fluorescence imaging. However it was not clear before starting whether the background would be sufficiently reduced to observe the transition in this experiment.

6.6 Summary

To summarise the results of this chapter, I have shown that the molecule chip experiment is compatible with ultra-high vacuum conditions required for the CaF experiment, the small wires on the chip can handle the currents needed to create

the traps that were described and simulated in chapter 4. The chip trap is therefore ready for loading with CaF molecules. These molecules could be imaged with an optical cycling scheme to reduce background scatter. I have tested such a scheme in a CaF beam where it was possible to resolve the required $X(v = 0) \rightarrow A(v = 1)$ transition, but due to the limited power of the laser used it was not possible to successfully implement the scheme for a cloud of cold molecules.

Chapter 7

Coupling CaF to on-chip microwaves

One of the key motivations for developing a molecule chip is the ability to integrate microwave guides for strong coupling between microwave photons and the rotational transitions in molecules. In this chapter I will present how such a scheme can be realised. I will begin with a summary of the coplanar waveguide (CPW), which can be used to guide microwaves across a dielectric surface. I will then move on to discuss the logistics of integrating a CPW into the experiment, and especially on the delivery of microwaves to the chip. I will then present two uses of single CaF molecules coupled to microwave guides: sideband cooling and state readout.

7.1 The coplanar waveguide

The CPW was originally proposed by Cheng P. Wen as a means of guiding microwaves across the surface of a dielectric substrate [124]. It consists of a central conductor with a ground plane on either side, as pictured in Fig. 7.1 (a). CPWs have become prolific, since they allow the creation of robust microwave devices, and offer some benefits over other waveguide architectures, such as the stripline waveguide, because they can provide circularly polarised fields, and also provide easy access to the ground plane for shunt connections.

The CPW's geometry is defined by the centre conductor width (S) and the channel width (W). The height of the conductor is t and the dielectric height is h . The geometry of the CPW determines the region the microwave field occupies, as illustrated in Fig. 7.1 (b). The CPW can therefore be designed to maximise overlap between the microwave field and a cloud of molecules trapped nearby. As a rough approximation, this is achieved when the molecules are trapped above the centre of the CPW, at a distance on the same length scale as S [47]. The electric field

surrounding the CPW is shown in Fig. 7.1 (b). The equations defining this field can be found analytically [151], or the field can be determined by a finite-element simulation.

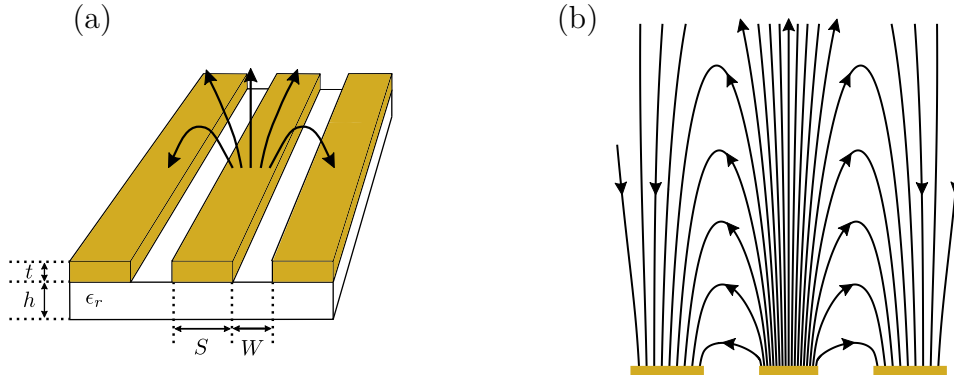


Figure 7.1: Subfigure (a) shows a perspective view of a segment of CPW on dielectric substrate, with pertinent geometry and dielectric constants labeled. The field lines are sketched, and shown in detail in the cut-through in (b). Here the field lines are calculated analytically for arbitrary parameters. In both subfigures the even mode of the CPW is shown.

7.1.1 CPW properties

We will now consider the electric properties of a CPW. These will largely depend on the planar geometry of the waveguide, which we express in terms of the ratio [124, 151]

$$k_0 = \frac{S}{S + 2W}. \quad (7.1)$$

For convenience, we also define the value

$$k'_0 = \sqrt{1 - k_0^2}. \quad (7.2)$$

For a waveguide made of a material with conductivity σ and permeability μ and propagating field with frequency ω there is a skin depth [151]

$$\delta = \sqrt{\frac{2}{\omega \mu \sigma}} \quad (7.3)$$

and skin effect surface resistance [151]

$$R_s = \frac{1}{\sigma \delta}. \quad (7.4)$$

Since the field of the CPW will pass through both the dielectric and the surrounding air, the CPW's capacitance is the sum of the capacitance of each of these

two parts

$$C_{\text{CPW}} = C_{\text{dielectric}} + C_{\text{air}}. \quad (7.5)$$

The method of finding these individual contributions is somewhat involved, so we simply state the results here in terms of the elliptic integral of the first kind, $K(k)$ [151]. The capacitance due to the dielectric is

$$C_{\text{dielectric}} = 2\epsilon_0(\epsilon_r - 1) \frac{K(k_0)}{K(k'_0)} \quad (7.6)$$

and the capacitance of the air region is

$$C_{\text{air}} = 4\epsilon_0 \frac{K(k_0)}{K(k'_0)}. \quad (7.7)$$

We can use this to find the effective permittivity [151]

$$\epsilon_{\text{eff}} = \frac{C_{\text{dielectric}}}{C_{\text{air}}} \quad (7.8)$$

$$= \frac{1 + \epsilon_r}{2}, \quad (7.9)$$

where we have assumed that we are in the limit of a thick dielectric layer ($h \gg W$) so that most of the field density below the surface is inside the dielectric. The phase velocity is [151]

$$v_{\text{ph}} = \frac{c}{\sqrt{\epsilon_{\text{eff}}}} \quad (7.10)$$

$$= \frac{c}{\sqrt{(1 + \epsilon_r)/2}}. \quad (7.11)$$

Now using the approximation [152] $\sqrt{\mu_0/\epsilon_0} \approx 120\pi$ ohm we have the line impedance [151]

$$Z_0 = \frac{1}{C_{\text{air}} v_{\text{ph}}} \quad (7.12)$$

$$= \frac{30\pi}{\sqrt{(\epsilon_r + 1)/2}} \frac{K(k_0)}{K(k'_0)} \text{ ohm}. \quad (7.13)$$

Note that the impedance of the waveguide has dependence only on the geometry in the form of the ratio k_0 , and the relative permittivity of the substrate [151]. This means that for any substrate we choose, the value of k_0 can be chosen to fix the impedance at the standard $Z_0 = 50\Omega$, which is useful for impedance matching to external components. It is also possible to match between macroscopic and microscopic components by tapering the CPW scale whilst holding k_0 constant. This allows the building of macroscopic input ports to the CPW, and then tapering

for a highly localised field near the molecule trap.

7.1.2 CPW attenuation

It is important to understand the level of attenuation through a CPW. Not only is it important that we can transmit enough signal to the molecules to drive rotational transitions, but the attenuation in a resonator will be the dominant factor in determining its quality factor, and hence whether we are in the strong coupling regime. Begin by considering the electric field inside a CPW. Say that the field at a position z along the axis of the guide is $E(z)$. This amplitude attenuates according to

$$E(z) = E(0)e^{-\alpha z}, \quad (7.14)$$

where we call α the attenuation constant.

There are two contributing terms to the attenuation constant

$$\alpha = \alpha_d + \alpha_c, \quad (7.15)$$

which are the contributions from the dielectric and the conductor respectively. We neglect small contributions from radiative losses [153]. Bending losses can also be ignored as long as the radii of the bends are much larger than the wavelength of the propagating wave. We must be mindful of this during design, since the typical wavelengths for rotational transitions are on the order of millimeters. We also do not consider the insertion loss of the resonator, since this does not affect the quality factor [147].

Dielectric losses

Dielectric losses in the thick dielectric limit are described by [152]

$$\alpha_d = \frac{\omega_0 \epsilon_r}{4c\sqrt{\epsilon_{\text{eff}}}} \tan \delta_e, \quad (7.16)$$

where $\tan \delta_e$ is the dielectric loss tangent. Common dielectrics for microwave guides include aluminium nitride (AlN) and high-resistivity silicon. For our purposes we wish to consider waveguides situated on dielectric layers that can be easily deposited above the trapping wires. Following the work in Ref. [46], we primarily consider polyimide, which can be deposited by spin-coating. Other options are available, such as polyethylene naphthalate (PEN) [154].

Typical values of dielectric constants and α_d are shown in Table 7.1. Note that these parameters depend on the frequency of the microwave field, and to some extent the temperature of the dielectric, and so are presented to illustrate the amount of

Table 7.1: Dielectric constants and loss for various substrates in the 10 GHz regime at room temperature

Material	ϵ_r	$\tan \delta_e$	α_d (m $^{-1}$)	Ref.
Polyimide	3.4	1.8×10^{-2}	0.45	[155]
PEN	2.56	0.003	0.63	[154]
Silicon (high resistivity)	~ 12	2×10^{-4}	0.02	[151, 156, 157]
Sapphire	~ 10	2×10^{-5}	10^{-3}	[158]
Aluminium nitride	8.9	5×10^{-4}	0.22	[158]
Arlon AD1000	10.2	0.0023	1.0	[159]

Table 7.2: Electrical constants for various conductors in the 10 GHz regime at room temperature

Material	σ ($\times 10^6$ S m $^{-1}$)	μ_r	Ref.
Gold	44.2	1.0	[158]
Silver	62.1	1.0	[158]

loss that can typically be expected for our experiment at room temperature and frequencies in the 10 GHz regime.

Conductor losses

Conductor losses arise due to dissipation in the centre conductor and ground plane of the CPW [151]. The conductor attenuation constant is

$$\alpha_c = \frac{R_c + R_g}{2Z_0} \text{ m}^{-1}, \quad (7.17)$$

where R_c and R_g are the series resistances per unit length of the centre conductor and the ground plane respectively. For a waveguide with height t , these are given by

$$R_c = \frac{R_s}{4S(1 - k_0^2)K^2(k_0)} \left[\pi + \log\left(\frac{4\pi S}{t}\right) - k_0 \log\left(\frac{1 + k_0}{1 - k_0}\right) \right], \quad (7.18)$$

and

$$R_g = \frac{k_0 R_s}{4S(1 - k_0^2)K^2(k_0)} \left[\pi + \log\left(\frac{4\pi(S + 2W)}{t}\right) - \frac{1}{k_0} \log\left(\frac{1 + k_0}{1 - k_0}\right) \right]. \quad (7.19)$$

The electrical properties of silver and gold are given in Table 7.2, and the computed conductor attenuations are shown in Fig. 7.2. The latter of these shows the conductor losses for varying conductor thickness (a) and centre conductor width (b). Each of these are shown for gold on sapphire, silver on sapphire and gold on polyimide CPWs. In (a) we take $S = 10 \mu\text{m}$ and in (b) we take $t = 5 \mu\text{m}$. In both the free parameters are chosen to match an impedance of $Z_0 = 50 \Omega$.

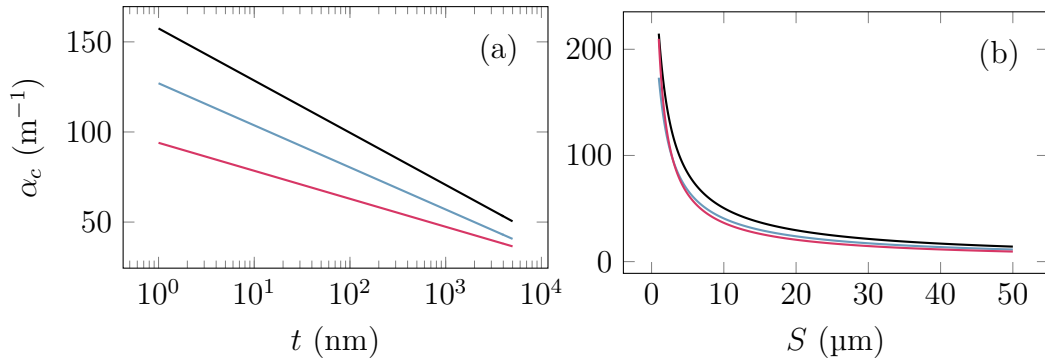


Figure 7.2: Conductor losses are plotted for (a) varying the conductor height of the CPW and (b) varying the centre conductor width. Losses are shown for gold on sapphire (black), silver on sapphire (blue) and gold on polyimide (pink). In (a) a typical conductor width of $S = 10 \mu\text{m}$ is assumed, and in (b) the thickness of the conductors is taken to be $t = 5 \mu\text{m}$. In both cases the impedance is set to $Z_0 = 50 \Omega$ by choosing k_0 , according to eqn (7.13).

As can be seen by comparing the values in Table 7.1 and Fig. 7.2, the conductor losses clearly dominate over the dielectric losses. With loss of $\alpha \approx \alpha_c$, and waveguides of lengths on the scale of a few centimeter, we can expect a total loss of around 35 dB. This should be sufficiently small that microwaves of the required power to drive rotational transitions will be able to reach molecules trapped on the chip. [46] However, such high conductor losses will prevent the implementation of a high- Q microwave resonator on the chip, as we will discuss in the next section.

7.1.3 CPW resonators

A microwave resonator can be formed from a section of CPW that is capacitively coupled to another driving segment [160]. The resonant frequency is determined by the resonator's length, L , and the waveguide's phase velocity [151]

$$\omega_0 = \frac{\pi v_{\text{ph}}}{L} = \frac{\pi c}{\sqrt{\epsilon_{\text{eff}}} L} \quad (7.20)$$

Microwaves can be coupled to the resonator by positioning the resonator inline with a microwave guide, or in parallel as shown in Fig. 7.3. The strength of the coupling can be controlled by the shape of the interface between the resonator and the waveguide [147].

The quality factors for CPW resonators can be expressed in terms of an attenuation constant

$$Q = \frac{\omega_0}{2c\alpha}. \quad (7.21)$$

From Fig. 7.2 and Table 7.1 we find that using conventional materials, the attenuation will be dominated by conductor losses, and $Q \sim 10$. It will be shown in

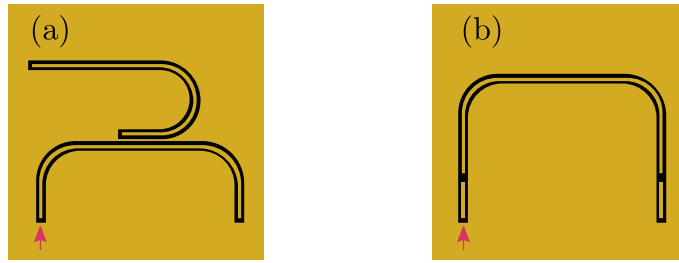


Figure 7.3: Different schemes for capacitive coupling into a microwave resonator. Gold represents conductor and black a dielectric substrate. In (a) the resonator runs parallel to a waveguide that feeds in microwaves. The input port is denoted by the arrow. In (b) the resonator is in series with the input port, and is also coupled to an output port.

section 7.2 that we require $Q > 1.7 \times 10^5$ for our purposes.

Conductor losses can be eliminated by use of a superconducting CPW. Such devices are a developed technology, which have been used for coupling to solid-state qubits [161]. Operating at the cryogenic temperatures required for superconductors allows the achievement of very high quality factors of order 10^6 [160, 162]. For such devices the quality factor is dominated by the dielectric losses, and as such a low-loss dielectric is usually chosen for the substrate (sapphire being a common choice). An alternative method to produce a multi-layer resonator could potentially be etching the polyimide in the slot gaps, as in Ref. [163]. Otherwise, a single-layer superconducting design such as that shown in Ref. [52] could be adopted. Regardless, the multilayer design remains a useful tool for microwave-molecule interactions, and investigating lower quality resonators coupled to molecules.

7.2 How to couple a molecule to a coplanar waveguide

Having established the principles of the CPW, and that such a device can operate on a polyimide substrate, we can now consider the logistics of implementing such a device with our design. In this section we will consider the details of the how the coupling of molecules to a CPW can work in practice, including the coupling Hamiltonian, tuning the molecular rotational frequency using the Stark shift, the delivery of microwaves to the chip, and schemes for sideband cooling and state readout with the microwaves.

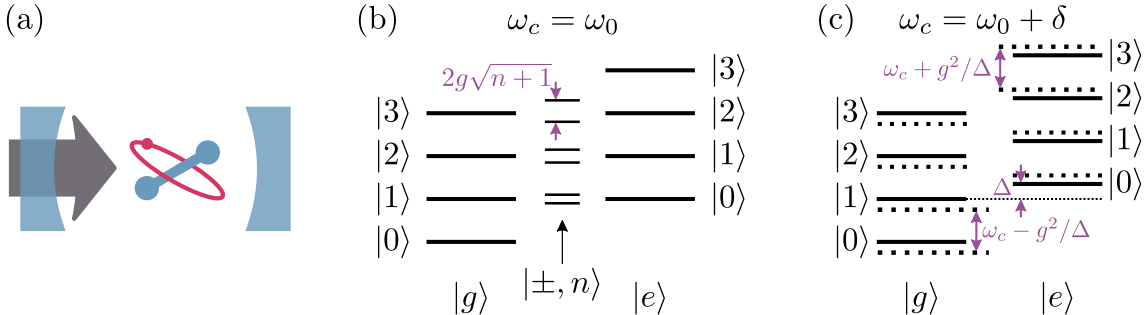


Figure 7.4: A two-level cavity QED system. Subfigure (a) shows a schematic of the system, where microwaves interact with a rotational transition in CaF. This implements the JCH, whose energy levels are shown both on (b) and off (c) resonance. Energy spacings are highlighted in purple. This figure is inspired by one in Ref. [57].

7.2.1 Cavity quantum electrodynamics

For our purposes, the coupling of a single molecule and the microwave field can be treated as the coupling of a two-level system to a quantum mode of a cavity field. The canonical description of such a system is given by the familiar Jaynes-Cummings Hamiltonian (JCH) in the rotating wave approximation [164], which we will now briefly review. The relevant Hamiltonian is

$$H_{JC} = \hbar\omega_c a^\dagger a + \frac{\hbar\omega_0}{2}\sigma_z + \frac{\hbar\Omega}{2}(a^\dagger\sigma_- + a\sigma_+), \quad (7.22)$$

where a (a^\dagger) is the annihilation (creation) operator of the photons, Ω is the Rabi frequency of the interaction, σ_i with $i \in x, y, z$ are the Pauli matrices, and $\sigma_\pm = (\sigma_x \pm i\sigma_y)/2$ are the raising and lowering operators of the molecule state. The detuning of the cavity resonance from that of the spin is $\Delta = \omega_0 - \omega_c$. The system is shown in Fig. 7.4 (a).

We denote the ground (excited) state of the molecule as $|g\rangle$ ($|e\rangle$). The light field state can be taken to be a Fock state ($|n\rangle$ with $n \in \mathbb{Z}$). Note that the final term in equation 7.22 has the effect of exciting the ground state while absorbing a photon ($|g\rangle|n\rangle \leftrightarrow |e\rangle|n-1\rangle$) or lowering the excited state and releasing a photon ($|e\rangle|n\rangle \leftrightarrow |g\rangle|n+1\rangle$).

Following the procedure in Ref. [164], we can see that this mixing of the states results in a shift of the energy levels to create the dressed states

$$|+, n\rangle = \cos\Phi_n |g\rangle|n\rangle + \sin\Phi_n |e\rangle|n+1\rangle \quad (7.23)$$

$$|-, n\rangle = -\sin\Phi_n |g\rangle|n\rangle + \cos\Phi_n |e\rangle|n+1\rangle \quad (7.24)$$

with

$$\tan(2\Phi_n) = \frac{\Omega\sqrt{n+1}}{\Delta} \quad (7.25)$$

and having shifted energies

$$E_{\pm,n} = (n + 1)\hbar\omega_c \pm \frac{\hbar}{2}\sqrt{\Omega^2(n + 1) + \Delta^2}. \quad (7.26)$$

It is useful to consider the manifold of states as depicted in Fig. 7.4. Note that in the limit of no coupling ($\Omega = 0$) and no detuning ($\Delta = 0$) the energies are those of the bare states, and $|g\rangle|n+1\rangle$ is degenerate with $|e\rangle|n\rangle$, as in part (b) of the subfigure. Introducing coupling ($\Omega \neq 0$) lifts this degeneracy, as in part (c). When the detuning is non-zero ($\Delta \neq 0$) there is additional offset due to the second term in eqn (7.26), see part (d) of the figure.

The strong coupling regime is reached when the coupling $g = 2\Omega$ is greater than the rate of decay from the cavity $\kappa = \omega_0/Q$, where Q is called the quality factor of the cavity. The coupling parameter is related to the transition dipole moment d and the amplitude of the electric field E_0 by

$$\hbar g = \frac{dE_0}{2}. \quad (7.27)$$

For the resonator, the amplitude of the electric field can be expressed in terms of the cavity parameters by considering the electric field density

$$\frac{1}{2}\epsilon_0 E_0 = \frac{\hbar\omega_0}{V}, \quad (7.28)$$

where V is the volume of the mode in the cavity. The idea is to confine the molecules in a trap that is on the $w = 10 \mu\text{m}$ scale (see section 3.2) and the resonator will necessarily have a length on the scale of $\lambda_0 = 2\pi c/\omega_0$, therefore $V \approx w^2\lambda_0$. Hence we have that

$$g = \sqrt{\frac{2\pi cd^2}{\hbar\epsilon_0 w^2 \lambda_0^2}}. \quad (7.29)$$

For the rotational CaF transitions that we introduced above, in section 2.3 $d = \mu/\sqrt{3}$ with $\mu = 31 \text{ D}$. The coupling strength is therefore expected to be

$$\frac{g}{2\pi} = 20 \text{ kHz} \quad (7.30)$$

and for strong coupling a cavity quality of

$$Q = \frac{\omega_0}{g} > 1.7 \times 10^5 \quad (7.31)$$

is required.

7.2.2 Stark shift

Since the resonant frequency of the resonator is fixed by its length, it will be useful to be able to tune the frequency of the molecule transition, bringing the molecules into or out of resonance with the microwaves. We will see that this is key for state readout in section 7.4.1. We propose that the detuning can be controlled by the Stark shift due to a d.c. field. By positioning voltage-biased pads near to the molecule trap, the d.c. field can be used to shift the transition frequency.

When the shift is sufficiently small compared to the unperturbed energy, the Stark shift can be found by second-order perturbation theory. We start with the rotational eigenstates $|N, m_N\rangle$ whose energies are $E_{\text{rot}}(N) = BN(N + 1)$, and add the perturbation $H' = \mu_e E \cos(\theta)$, where μ_e is the dipole moment in the frame of the molecule, E is the electric field applied along z , and θ is the angle between the dipole moment and the z -axis. Recognizing that $\cos(\theta)$ is the reduced spherical harmonic $C_0^{(1)}$, and applying second-order perturbation theory, we find that the energy shift of $|N, m_N\rangle$ is

$$\Delta_{N, m_N} = \sum_{N', m'_N} \frac{(\mu_e E)^2}{E_{\text{rot}}(N) - E_{\text{rot}}(N')} |\langle N', m'_N | C_0^{(1)} | N, m_N \rangle|^2. \quad (7.32)$$

It can be helpful to express the matrix element by rewriting the integrals over spherical harmonics in terms of 3- j symbols [165],

$$\begin{aligned} \langle N', m'_N | C_0^{(1)} | N, m_N \rangle = \\ (-1)^{m'_N} \sqrt{(2N+1)(2N'+1)} \begin{pmatrix} N' & 1 & N \\ -m'_N & 0 & m_N \end{pmatrix} \begin{pmatrix} N' & 1 & N \\ 0 & 0 & 0 \end{pmatrix}. \end{aligned} \quad (7.33)$$

The summation in eqn (7.32) can be simplified when we note that the 3- j symbols are only non-zero when $m'_N = m_N$ and $N = N' \pm 1$. It is simple to compute the resulting energy shift for arbitrary states, and the results are shown for the $N = 0, 1, 2$ states of CaF in Fig. 7.5. We note that it is possible to induce shifts of several gigahertz with a modest electric field strength. We anticipate that only shifts of < 10 MHz will be required in an experiment, and for such small perturbations, any additional effects of mixing hyperfine states, or effects due to the magnetic field can be ignored.

7.2.3 Integrating microwave components

The chip flange (shown in Fig. 3.10) has been designed to incorporate MDC Precision's SMA45-GS-WELD 2.92 mm high-frequency SMA feedthroughs. These welded connectors can be used to bring microwaves inside the chip chamber, where they can

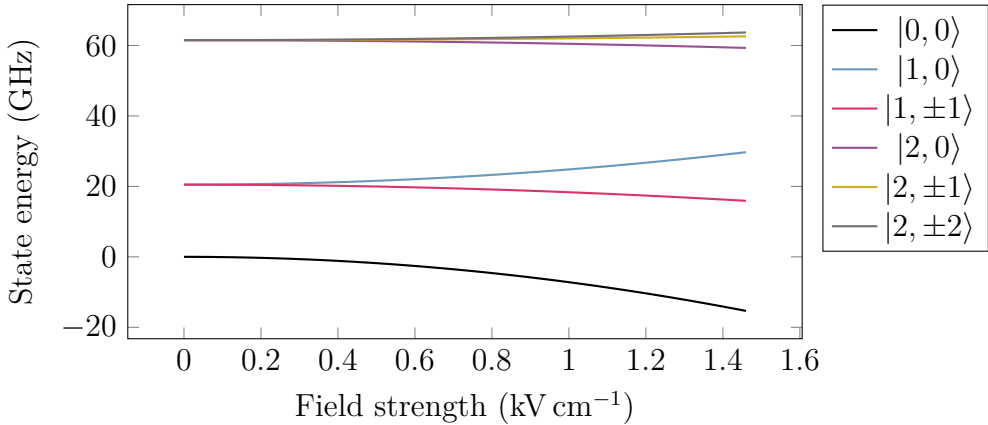


Figure 7.5: The Stark effect for low-lying rotational states of the CaF molecule $|N, m_N\rangle$ found by second order perturbation theory.

be launched onto a CPW on the subchip. Microwaves will be transferred through from the feedthrough to the subchip using a SMA male-male barrel adapter from Pasternak, and a female-clamp PCB launcher from Pasternack. The launching assembly can be seen in Fig. 7.6 (a). These components have been tested for UHV compatibility, as discussed in section 6.2. The flange assembly has been designed to allow microwaves to exit the chamber, where they can be terminated or measured.

Once launched onto the subchip, the microwaves will be delivered by CPW to the subchip. In future iterations of the experiment the aluminium-core PCB can be replaced with, for example, an Arlon AD1000 board, which will be a suitable carrier for both trapping currents and microwaves [166]. The subchip CPW will be connected to the chip CPW by wire-bonds. At the point where the wire-bonds connect, the CPW can be chosen to be large enough so that it is easy to make good connection with the wire bonds. The CPW can then tapered down to reduce the field size while maintaining the same k_0 and hence the same impedance. This CPW can be capacitively coupled to a microwave resonator, but for a simple example we show a multi-layer design for a single CPW in Fig. 7.6. Note that the orientation of the waveguide relative to the trapping wires is not critical. Although the magnetic dipole moment of the molecule is oriented relative to the magnetic field of the trap, the molecule frame electric dipole moment is not oriented because there is no applied electric field. It is only necessary to ensure that the polarization of the microwave field propagating in the waveguide is suitable for driving the desired transition. The relative orientation of waveguide and wires was chosen with the hope that any bumps caused by the wires will not unduly affect the waveguide properties.

To form an even smaller trap than discussed above, the CPW centre conductor can be biased, to create a dimple trap along with the underlying axis of the Z-wire, as was done in Ref. [46]. For a resonator it would also be possible to introduce a bias field, but this would have to be done on-chip with a band stop filter [167]. This

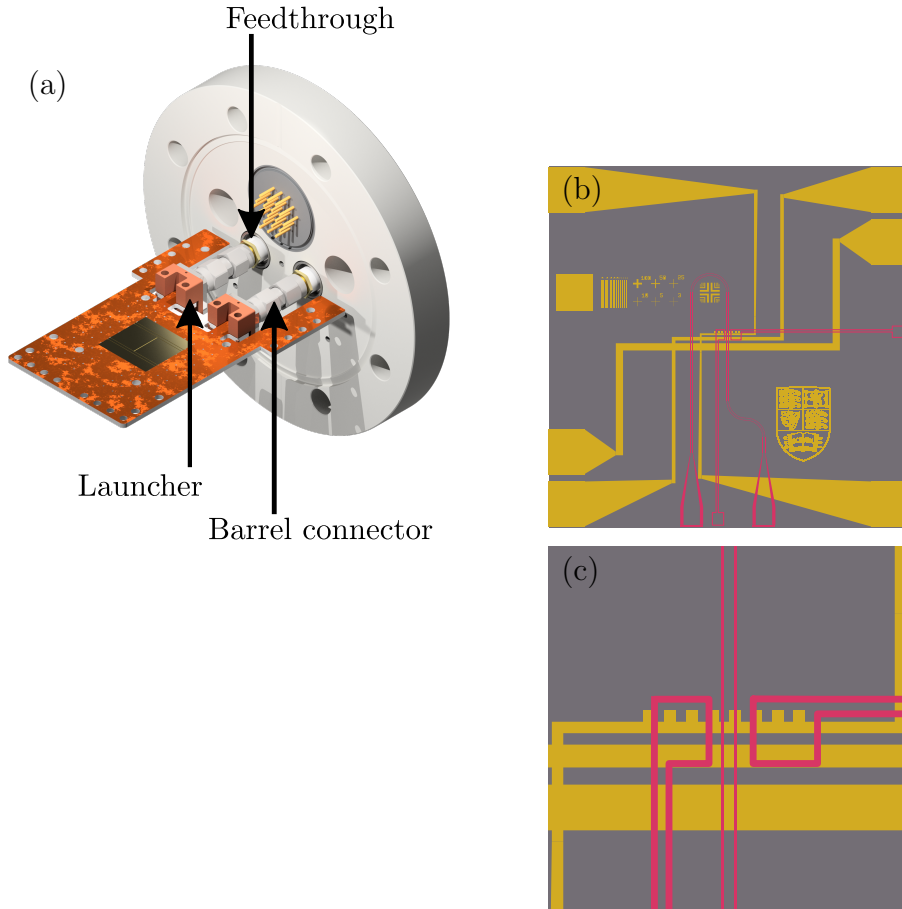


Figure 7.6: The microwave components of the flange assembly (flange, feedthroughs, barrel connectors, launchers, PCB and chip) are shown in (a). In (b) we have the chip design from Fig. 3.10 (not to scale) with the additional microwave guide layer overlaid (red). Conversely to the lower layer, the microwave layer shows areas where the dielectric is exposed, so regions that aren't pink are covered with conductor. Example voltage pads for Stark-shifting the molecules are also shown. Subfigure (c) shows a detailed view of the trapping region.

could also be used to implement the electrostatic traps described in Ref. [2].

7.3 Sideband cooling

This subsection summarises the sideband cooling scheme presented in Ref. [2] and presents cooling rates for our trapping scheme with CaF. Throughout the section we assume that we operate with a single molecule coupled to a high-quality cavity ($Q \sim 10^6$, $\kappa \approx 2\pi \times 20$ kHz) in the strong coupling regime ($g \sim 10^5$). We take the molecule to act as a two-level system in the stretched state, which we introduced in section 3.1. For our example we choose $|g\rangle = |0\rangle_{\text{str}}$ and $|e\rangle = |1\rangle_{\text{str}}$.

In the macroscopic magnetic trap, the $|e\rangle \rightarrow |g\rangle$ decay is very slow ($\Gamma \sim 10^{-5}$ Hz), but when a molecule is in close proximity to a microwave resonator at the transition

frequency, the decay rate is strongly enhanced with rate

$$\Gamma_c = \frac{\kappa}{2}. \quad (7.34)$$

This enhanced decay rate opens the door to sideband cooling into the motional ground state of the trap.

We write the state of the molecule as $|i, m\rangle$ where $i \in \{e, g\}$ is the state of the molecule, and m is the quantum number of the motion in the trap. For any ground state $|g, m\rangle$ there is a carrier frequency transition to $|e, m\rangle$ at the resonant frequency ω_0 , and sidebands to the $|e, m + m'\rangle$ states at frequency $\omega_0 + m'\omega_t$, where ω_t is the trap frequency and $m' \in \mathbb{Z}$. There are similar carrier and sideband transitions for $|e, m\rangle \rightarrow |g, m + m'\rangle$.

We imagine that an external driving field is applied on the $|g, m\rangle \rightarrow |e, m - 1\rangle$ sideband as pictured in Fig. 7.7. Combined with the enhanced decay, this allows sideband cooling into low motional ground states of the trap. The molecule will be transferred by the driving field into a lower motional state, and will rapidly decay into the ground state by releasing a photon into the resonator. Each time this happens the molecule's energy is reduced by $\hbar\omega_t$. This results in a cooling rate

$$R_{\text{sbc}} = \frac{\hbar\Gamma_c\omega_t}{k_B}. \quad (7.35)$$

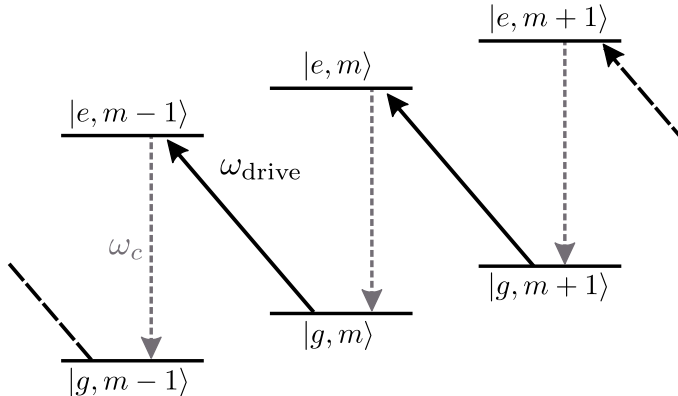


Figure 7.7: The sideband cooling scheme is shown, with an external driving field applied to the $|g, m\rangle \rightarrow |e, m - 1\rangle$ transition. Decay on $|e, m\rangle \rightarrow |g, m\rangle$ is strongly enhanced by the resonator, allowing sideband cooling to low motional states.

As per the discussion in section 2.2, we expect typical trap frequencies $\omega_t \sim \times 10^5 \text{ s}^{-1}$ and therefore the cooling rate will be of order 10 mK s^{-1} . This is shown for a molecule in a dimple trap at various trapping currents in Fig. 7.8 (a).

The lowest motional state that can be reached is determined by the background photon number in the resonator. A typical high- Q cavity will operate at a few tens of millikelvin [147] but these temperatures require a dilution fridge, and high-

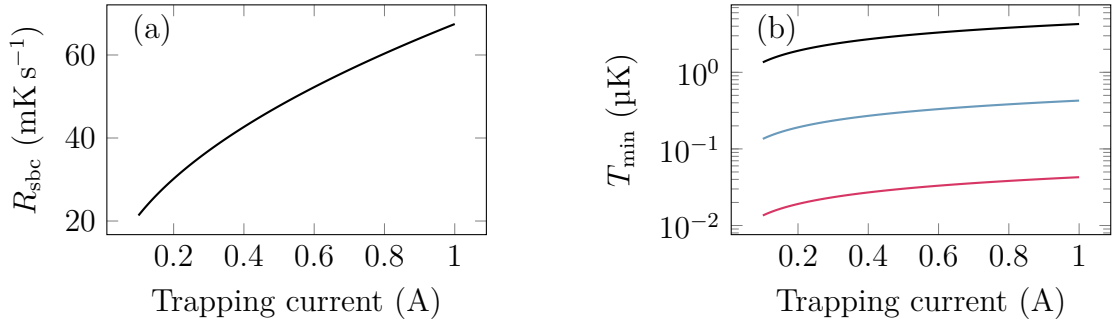


Figure 7.8: Subfigure (a) shows the cooling rate for varying trapping current for a $Q = 10^6$ resonator and dimple trap (see section 2.2.1). Subfigure (b) shows the minimum temperature that can be achieved as a function of trapping current for different resonator temperatures: 4 K (black), 400 mK (blue) and 40 mK (red).

temperature superconductors can operate at typical cryocooler temperatures of $T_c = 4$ K. This corresponds to a background photon number of

$$\bar{m} = \frac{k_B T_c}{\hbar \omega_0}. \quad (7.36)$$

It has been commonly shown that other sources of background photons can be eliminated [161], in particular it can be useful to filter high-frequency photons that can enter from the input ports [168].

We expect the minimum temperature achievable by sideband cooling to be reached when the molecule motion and photon energy are in thermal equilibrium, so that

$$T_{\min} = \frac{\hbar \omega_t \bar{m}}{k_B} \quad (7.37)$$

$$= \frac{\omega_t}{\omega_0} T_c \quad (7.38)$$

which is shown as a function of the trapping current for various resonator temperatures in Fig. 7.8 (b).

7.4 Entangling light and photon states

Reference [2] also proposes entangling the molecule state with the quantum state of photons in the resonator. This is inspired by the methodology of Ref. [57] where the state of a Cooper-pair box is entangled with a resonator state. This entanglement can be used to perform state readout, state preparation and coupling to neighbouring qubits. In this section we will mainly discuss state readout, since this framework will be useful in chapter 8.

We again assume that the molecule is trapped in the $N = 0$ or $N = 1$ stretched

states. In this case the resonator is driven by a microwave field, so that the molecule-resonator coupling is described by the Jaynes-Cummings Hamiltonian that was discussed in section 7.2.1. Entangling of the light and molecule state can be achieved in the dispersive regime, where the transition frequency is tuned so that $|\Delta| \gg g$. Reference [57] tells us that we can gain insight into the dispersive behaviour by applying the unitary transformation

$$U = \exp \left[\frac{g}{\Delta} (a\sigma_+ - a^\dagger\sigma_-) \right]. \quad (7.39)$$

With expansion up to second order in g/Δ , we obtain

$$H = U H_{\text{JC}} U^\dagger \approx \hbar\omega_c a^\dagger a + \frac{\hbar}{2} \left(\omega_c + \frac{g^2}{\Delta} \right) s_z + \frac{\hbar g^2}{\Delta} s_z a^\dagger a. \quad (7.40)$$

Here we have introduced the spin operator $s_i = \sigma_i/2$ for convenience.

The three terms of H describe the oscillation of light in the cavity, the energy of the spin and the interaction of the photons with the spin. Note that the interaction of the photons and the spins induces the usual AC Stark shift proportional to $(n + \frac{1}{2})$. The last term can be used to make a quantum non-demolition (QND) measurement, since it will enable exchange of information between the z-component of the spin with the photons.

We take the state of the photons in the resonator to be in a canonical coherent state [169]

$$|\alpha\rangle = e^{-\frac{|\alpha|^2}{2}} \sum_{n=0}^{\infty} \frac{\alpha^n}{\sqrt{n!}} |n\rangle \quad (7.41)$$

with $\alpha \in \mathbb{C}$, and $|n\rangle$ representing the n^{th} Fock state of the light [170]. For such a state $|\alpha|^2$ is the average photon number, with $a^\dagger a$ being the number operator such that $\langle \alpha | a^\dagger a | \alpha \rangle = |\alpha|^2$.

The interaction of the light with the molecule is described by the last term in H , so for an interaction over time T , we have

$$|\Psi(T)\rangle = \exp(-iH_{\text{int}}T/\hbar) |\Psi(0)\rangle, \quad (7.42)$$

where

$$H_{\text{int}} = \hbar \frac{g^2}{\Delta} s_z a^\dagger a \quad (7.43)$$

and $|\Psi(0)\rangle = |\psi\rangle |\alpha\rangle$ is the state of the system at the time of measurement. This can be expanded by inserting the definition of the coherent state and expanding the molecule state,

$$|\Psi(T)\rangle = e^{-\frac{|\alpha|^2}{2}} \sum_{n=0}^{\infty} \frac{\alpha^n}{\sqrt{n!}} e^{-i\nu T s_z a^\dagger a} |n\rangle (\cos \theta |g\rangle + e^{i\phi} \sin \theta |e\rangle), \quad (7.44)$$

where $\nu = g^2/\Delta$. Now the number operator in the exponent acts on the light state ($|n\rangle$) and the spin operator acts on the molecule state ($|g\rangle$ or $|e\rangle$) for

$$|\Psi(T)\rangle = e^{-\frac{|\alpha|^2}{2}} \sum_{n=0}^{\infty} \frac{\alpha^n}{\sqrt{n!}} (e^{i\nu T n \hbar/2} \cos \theta |n\rangle |g\rangle + e^{-i\nu T n \hbar/2} e^{i\phi} \sin \theta |n\rangle |e\rangle). \quad (7.45)$$

Collecting the coefficients of the molecule states yields

$$|\Psi(T)\rangle = \cos \theta \left(e^{-\frac{|\alpha|^2}{2}} \sum_{n=0}^{\infty} \frac{(\alpha e^{i\nu T \hbar/2})^n}{\sqrt{n!}} |n\rangle \right) |g\rangle + e^{i\phi} \sin \theta \left(e^{-\frac{|\alpha|^2}{2}} \sum_{n=0}^{\infty} \frac{(\alpha e^{-i\nu T \hbar/2})^n}{\sqrt{n!}} |n\rangle \right) |e\rangle. \quad (7.46)$$

Finally, note that each of the photon states (in parentheses) defines a coherent state, so the resulting state after interaction is

$$|\Psi(T)\rangle = \cos \theta |\alpha_+\rangle |g\rangle + e^{i\phi} \sin \theta |\alpha_-\rangle |e\rangle, \quad (7.47)$$

where $\alpha_{\pm} = \alpha \exp(\pm i\nu T \hbar/2)$.

7.4.1 State readout

The state of the molecule is now entangled with the state of the light in such a way that measuring the phase of the light will perform a readout of the molecule state. In this subsection I will present the homodyne measurement [170] technique in the context of performing a measurement of our molecule state.

The homodyne measurement is illustrated in Fig. 7.9. The light to be measured, here labelled $|\Psi_a\rangle$, is incident on one port (a) of a beam splitter. On the other port (b) we have a strong local oscillator in a coherent state $|\beta\rangle$, with large amplitude, in this case meaning that $|\beta| \gg |\alpha|$. We set the relative phases of $|\alpha\rangle$ and $|\beta\rangle$ so that $\arg(\alpha) = 0$ and $\arg(\beta) = -\varphi$.

The annihilation operators associated with the input ports are related to those of the output ports (c and d) by the usual relation for a balanced beam splitter [170]

$$\begin{pmatrix} c \\ d \end{pmatrix} = \frac{1}{\sqrt{2}} \begin{pmatrix} 1 & i \\ i & 1 \end{pmatrix} \begin{pmatrix} a \\ b \end{pmatrix}. \quad (7.48)$$

The difference in the expected photon numbers arriving at each detector is therefore

$$\langle c^\dagger c - d^\dagger d \rangle = i \langle a^\dagger b - ab^\dagger \rangle \quad (7.49)$$

$$= i \langle \Psi_a | \langle \beta | (a^\dagger b - ab^\dagger) | \beta \rangle | \Psi_a \rangle \quad (7.50)$$

$$= i |\beta| \langle \Psi_a | (a^\dagger e^{i\varphi} - a e^{-i\varphi}) | \Psi_a \rangle. \quad (7.51)$$

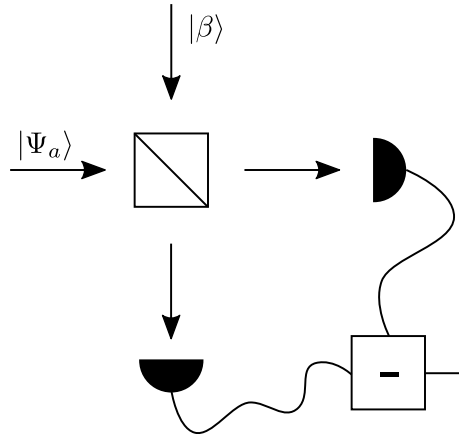


Figure 7.9: Schematic of a homodyne measurement. The state to be measured $|\Psi_a\rangle$ is incident on port (a) of the beamsplitter, and the local oscillator $|\beta\rangle$ is incident on port (b). The signal from photodiodes at the output ports is summed to produce a homodyne measurement.

Note that in the last equality we have used $b|\beta\rangle = \beta|\beta\rangle$, and also the equivalent conjugate expression $\langle\beta|b^\dagger = \beta^*\langle\beta|$ to remove the b and b^\dagger operators and replace them with their eigenvalues. We now introduce the canonical quadratures of the light field, corresponding to its real and imaginary parts. They are defined by [164]

$$X = \frac{a + a^\dagger}{2} \quad Y = \frac{a - a^\dagger}{2i}. \quad (7.52)$$

The expected photon difference is now

$$\langle c^\dagger c - d^\dagger d \rangle = 2|\beta| \langle \Psi_a | (Y \cos \varphi - X \sin \varphi) |\Psi_a \rangle. \quad (7.53)$$

Hence measuring the intensity of each output of the beamsplitter can give us information on the phase of the light. We choose $\varphi = 0$ so that the measurement is of the Y quadrature, i.e. we measure the imaginary part of $|\Psi_a\rangle$

$$\langle c^\dagger c - d^\dagger d \rangle = 2|\alpha||\beta| \langle \sin(\nu T s_z) \rangle. \quad (7.54)$$

For a short pulse of light, the interrogation time will be the lifetime of the photons in the cavity, $T = \kappa^{-1}$. In this regime we can expand sine to first order, so that

$$\langle c^\dagger c - d^\dagger d \rangle = 2|\alpha||\beta| \frac{g^2}{\Delta\kappa} \langle s_z \rangle. \quad (7.55)$$

In other words, the expectation value of the photon measurement is linked directly to that of the molecule's state. A measurement of $\langle c^\dagger c - d^\dagger d \rangle$ will also measure s_z . This allows for readout of the spin state via the microwave ports.

For this readout procedure, we have made the assumptions that we are operating

in the dispersive regime ($|\Delta| \gg g$) but in the final step (eqn (7.55)) the expansion of sine require a stricter condition, that

$$\frac{g^2}{\Delta\kappa} \ll 1. \quad (7.56)$$

The detuning required for our g and Q is therefore $\Delta \gg 2\pi \times 5 \text{ MHz}$, which is within the bounds achievable with the Stark shift.

7.4.2 State preparation

The entangling of the molecule and light state will produce a powerful system with applications beyond simple state readout. First, the system can be used to produce Schrödinger cat states in the light field [2]. This can be achieved by pulsing the microwaves to produce the entangled state in eqn (7.47). Expressing the molecule state in the x basis $|\pm\rangle = (|g\rangle \pm |e\rangle)/2$, this becomes

$$|\Psi(T)\rangle = |A_+(\theta, \phi)\rangle |+\rangle + |A_-(\theta, \phi)\rangle |-\rangle \quad (7.57)$$

with

$$|A_{\pm}(\theta, \phi)\rangle = \cos \theta |\alpha_+\rangle \pm e^{i\phi} \sin \theta |\alpha_-\rangle. \quad (7.58)$$

Now independent measurement of the molecule state in the x basis will yield $|\pm\rangle$, heralding the creation of the $|A_{\pm}(\theta, \phi)\rangle$ Schrödinger cat state in the light field. This is an attractive method for producing such states in the microwave regime, in analogy to what has previously been achieved using visible light [171].

7.4.3 Coupling between molecules

As reported in Ref. [2], the entanglement can also be used to couple between molecules trapped near the same resonator. We write the state of the two molecules as $|\Psi\rangle_i$, $i \in \{1, 2\}$, with the detunings individually controlled labelled Δ_i . Molecule 1 can be addressed independently of 2 by setting $\Delta_2 \gg \Delta_1$ and visa versa.

When $\Delta_1 = \Delta_2$ the interaction Hamiltonian between the two molecules can be found by adiabatic elimination of the photon state to be [2]

$$H_{\text{int}} = \hbar \frac{g^2}{\Delta} (\sigma_+^1 \sigma_-^2 + \sigma_-^1 \sigma_+^2), \quad (7.59)$$

where σ_k^i is the σ_k operator acting on the i^{th} molecule. Such an interaction can be used to implement a two-qubit operation on a chip [2, 57].

Chapter 8

A method to create non-classical spin states

In the previous chapter I described the interaction of a single molecule with a microwave resonator, but for some experiments a large number of molecules is desirable. This is particularly true in the field of precise measurement. Naively we can say that for a measurement of N particles, the signal to noise ratio (SNR) goes like \sqrt{N} , ergo increasing the number of particles will increase SNR. This result holds for uncorrelated particles. When the particles are entangled, the scaling can be better than \sqrt{N} , and in the ideal case can instead scale as N . When N is large, this offers a huge potential benefit for the precision of a measurement. Such states are typically referred to as spin-squeezed states (SSS) because the improvement in precision comes from reducing (squeezing) the uncertainty in one spin component at the expense of a different one [172, 173]. A useful review of squeezing and some of its applications is found in Ref. [174]. In this chapter I will present a proposal for how large ensembles of CaF molecules trapped on a chip could be used to create SSSs with potential application in quantum measurement. I will also suggest how this technique can be adapted to produce Schrödinger cat states, or applied in other architectures.

8.1 Spin states of an ensemble

We begin with an overview of the quantum states of a non-interacting ensemble of spin-half particles. In the first sub-section I will introduce the coherent spin state (CSS), where all spins in the ensemble are aligned. I will then explain how such a state can be converted into a SSS by quantum non-demolition measurement and why the SSS is a useful tool for precise quantum measurement.

8.1.1 Coherent spin states

For an ensemble of N spin-half particles, we label the Pauli matrices and the ladder operators for the i^{th} spin as σ_*^i . The spin operator for this particle is then

$$\mathbf{s}^i = \frac{1}{2} \begin{bmatrix} \sigma_x^i \\ \sigma_y^i \\ \sigma_z^i \end{bmatrix}. \quad (8.1)$$

We now define the collective spin operator

$$\mathbf{S} = \sum_{i=1}^N \mathbf{s}^i. \quad (8.2)$$

The common eigenstates of S^2 and S_z are the familiar angular momentum eigenstates, which we label $|S, m\rangle$, so that $S^2 |S, m\rangle = S(S+1) |S, m\rangle$ and $S_z |S, m\rangle = m |S, m\rangle$. These are the so-called Dicke states [175], which we will see shortly are entangled states of the spin system. The ladder operators for such a state are correspondingly [103]

$$S_\pm = \sum_{i=1}^N \sigma_\pm^i, \quad (8.3)$$

where we recall that σ_\pm^i represents the usual raising and lower operators for the i^{th} spin.

Consider how we can write down the total state of the system. For an individual spin, the state can be written as

$$|\psi(\theta, \phi)\rangle_i = \cos\left(\frac{\theta_i}{2}\right) |e\rangle_i + e^{i\phi_i} \sin\left(\frac{\theta_i}{2}\right) |g\rangle_i. \quad (8.4)$$

It is common to represent such a state visually by the Bloch sphere. The angles θ_i and ϕ_i define a point on a unit sphere with $|e\rangle_i$ and $|g\rangle_i$ at the poles. The Cartesian representation is given by the expectation value $\langle \mathbf{s}_i \rangle$. The state of the ensemble is then

$$|\Psi\rangle = \bigotimes_{i=1}^N |\psi\rangle_i \quad (8.5)$$

and the Bloch sphere representation is given by the sum of the individual spin vectors.

An important case is that of the coherent spin state (CSS), that is a state when all the spins are aligned, so that for all i , $\theta_i = \theta$ and $\phi_i = \phi$ [169, 176]. It is useful to consider a system where all spins are initially in, for example, the ground state. They then undergo the same uniform rotation into the desired state $|\psi(\theta, \phi)\rangle_i$, which

we write as

$$|\Psi(\theta, \phi)\rangle = \mathcal{R}(\theta, \phi) |G\rangle, \quad (8.6)$$

where $|G\rangle = \bigotimes_{i=1}^N |g\rangle_i$ and similarly for $|E\rangle$. We represent this visually on the Bloch sphere, now with radius $S = N/2$, in analogy with the single spin case, as illustrated in Fig. 8.1. Again we can represent the vector in a Cartesian form as the expectation value $\langle \mathbf{S} \rangle$. We note now that $|g\rangle = |S, -S\rangle$ and $|e\rangle = |S, S\rangle$ [103].

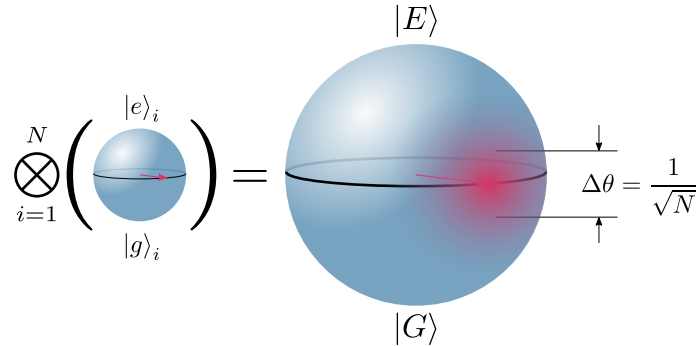


Figure 8.1: Graphical representation of a CSS formed by the combined state of N spins in the same state. In this case the spin states all lie on the equator of the Bloch sphere. The uncertainty in the CSS is represented by the patch, having a width $\Delta\theta$ (patch width is a guide to the eye and not to scale).

In the next section, we will make particular use of the state

$$|+\rangle = \bigotimes_{i=1}^N \left(\frac{|g\rangle_i + |e\rangle_i}{\sqrt{2}} \right). \quad (8.7)$$

Such a state can be represented on the Bloch sphere as a line pointing along the x axis ($\theta = \pi/2, \phi = 0$), as in Fig. 8.1, or can be found in terms of $|S, m\rangle$. A CSS can be written in the form

$$|\Psi\rangle = \sum_{m=-S}^S a_m |S, m\rangle \quad (8.8)$$

with the general form of a_m given in Ref. [177]. We will consider only $|+\rangle$, where the probability amplitudes can be understood as a probability of measuring m to be some value \tilde{m} . For any individual spin, the chances of measuring it to be in $|e\rangle_i$ or $|g\rangle_i$ are equal. Measuring the state to be in the state $|S, \tilde{m}\rangle$ is equivalent to measuring N_e molecules in the excited state, and $N_g = N - N_e$ in the ground state such that $2\tilde{m} = N_e - N_g$ (although note that we do not determine which spin is in which state). It follows that the probability of measuring the state to be $|S, \tilde{m}\rangle$ will occur with a binomial probability [169]

$$P(m) = \frac{1}{2^N} \binom{N}{m + N/2} \quad (8.9)$$

or for large N , the binomial is approximated by the Gaussian

$$P(m) \approx \frac{1}{\sqrt{2\pi\Delta_N^2}} e^{-m^2/(2\Delta_N^2)}, \quad (8.10)$$

where the variance is $\Delta_N^2 = N/4$. Note that Δ_N is an uncertainty in this probabilistic measurement, and has N as a parameter. It is not an uncertainty in the number of spins. We therefore rewrite the probability amplitudes of $|+\rangle$ so that

$$|+\rangle = \sum_{m=-S}^S \sqrt{P(m)} |S, m\rangle. \quad (8.11)$$

Such a state has expectation values $\langle S_z \rangle = 0$, $\langle S_z^2 \rangle = \Delta_N^2$, and the uncertainty in S_z is consistent with the usual formula $\Delta_N^2 = \langle S_z^2 \rangle - \langle S_z \rangle^2$. This uncertainty is the projection noise of a CSS, arising from the uncertainty in the measurement of the individual spins. We can understand this in terms of an uncertainty in the Cartesian Bloch vector $\langle \mathbf{S} \rangle$, or as an uncertainty in θ [172].

$$\Delta_{\theta,\text{SQL}} = \frac{1}{\sqrt{N}} \quad (8.12)$$

which is known as the standard quantum limit (SQL) or the shot-noise. By symmetry $\Delta\phi = \Delta\theta$ (corresponding to uncertainty in S_y). Note that these uncertainties hold only for $|+\rangle$ and other states where $\theta = \pi/2$ (states on the equator of the Bloch sphere). For example in the cases of $|E\rangle$ and $|G\rangle$, $\Delta\theta = 0$ [172].

8.1.2 Spin-squeezed states

The uncertainty in S_z ($\Delta_m \sim \Delta_\theta$) can be reduced at the expense of increasing uncertainty in other components of \mathbf{S} , so that the Heisenberg uncertainty principle is obeyed [172]. The resulting state is a spin-squeezed state (SSS), represented on the Bloch sphere in Fig. 8.2 (a) as a patch with reduced extent in the θ direction, and increased extent around the equator. The SSS can be manipulated by standard microwave spectroscopy techniques, for example by being rotated onto an axis of interest, such as is shown in Fig. 8.2 (b). Such states have been created and utilised for measurements below the SQL for example in atomic clocks [178]. Note that for a CSS, $\Delta_m = \Delta_N$, but for a SSS we can have $\Delta_m < \Delta_N$. This can also be thought of as reducing the uncertainty in θ , so we have uncertainty $\Delta_\theta < \Delta_{\theta,\text{SQL}}$.

One method of preparing a SSS is to implement a system with a one-axis twisting Hamiltonian [179], where the SSS is induced by, for example, collisions between particles [180]. Here, I propose a method to produce a spin-squeezed state of molecules. In this scheme, measurement of m is performed in such a way that the coherence of

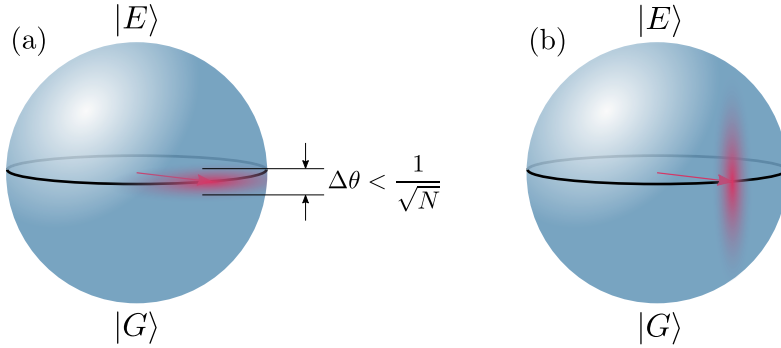


Figure 8.2: Graphical representations of SSSs. In (a) the state is squeezed along the S_z component, reducing $\Delta\theta$ beneath the SQL. In (b) a similar state has been rotated by a microwave pulse to move the reduced uncertainty into ϕ .

the quantum state of the spin ensemble is preserved, thus reducing the uncertainty Δ_θ (and hence also Δ_N). Similar experiments to our proposal have been performed for atoms trapped in optical cavities [181, 182], however our proposal will make use of the CPW microwave cavity for readout, similar to the method for a single molecule described in section 7.4.1.

Our scheme is readily exemplified by the creation of a maximally-squeezed state where the uncertainty is reduced as far as possible. Continuing the discussion from the previous section, suppose that we are able to prepare the CSS $|+\rangle$ and we then measure S_z . As previously described, we will measure $|S, \tilde{m}\rangle$ with some probability $P(\tilde{m})$. It is useful to frame such a measurement in a projector formalism. In general, the state of a system in state $|\Psi\rangle$ following a measurement is [164]

$$|\text{result}\rangle = \frac{\Upsilon |\Psi\rangle}{\sqrt{P_{\text{result}}}}, \quad (8.13)$$

where Υ is a projector into the measured state, and

$$P_{\text{result}} = \langle \Psi | \Upsilon | \Psi \rangle \quad (8.14)$$

is the probability of determining this result, ensuring that $|\text{result}\rangle$ is normalised. In the case of measuring S_z perfectly to be \tilde{m} the projector is

$$\Upsilon_0(\tilde{m}) = |S, \tilde{m}\rangle \langle S, \tilde{m}|. \quad (8.15)$$

which, as discussed already, yields $|S, \tilde{m}\rangle$ with probability $P(\tilde{m})$.

At this point it is worth pointing out that if we can realise such a measurement then we are done. The Dicke states are entangled states with a reduced uncertainty (except for $|G\rangle$ and $|E\rangle$) [183]. The Dicke states can be found by repeated application of the ladder operators [103], and are the superposition of all possible states

with N_e atoms in $|e\rangle$ and $N_g = N - N_e$ atoms in $|g\rangle$. We can therefore write in general that

$$\left| \frac{N}{2}, m \right\rangle = \binom{N}{N_e}^{-\frac{1}{2}} \sum_{\pi \in \Pi} \bigotimes_{i=1}^{N_e} \sigma_x^{\pi_i} |G\rangle \quad (8.16)$$

with $N_e = (N/2) + m$ and Π as the set of all possible combinations of N_e numbers chosen from $[1, N] \cap \mathbb{Z}$. This is perhaps more easily explored by example, which we can borrow from Ref. [181]. Consider the case where $N = 4$ and $\tilde{m} = 0$. This results in the state $|2, 0\rangle$ which is

$$|2, 0\rangle = \frac{1}{\sqrt{6}}(|eegg\rangle + |egeg\rangle + |egge\rangle + |geeg\rangle + |gege\rangle + |ggee\rangle). \quad (8.17)$$

Note that every possible combination of two excited, and two ground state spins appear in equal superposition. We can now see that this state is a maximally entangled state, and would be represented on the Bloch sphere as a ring around the equator [181]. Such a state necessarily has zero uncertainty in S_z , since this is the operator that has been measured. The state is therefore maximally squeezed and also has maximum uncertainty in S_x . Hence we have demonstrated that a measurement of $|+\rangle$ can produce a SSS. Such a state is non-classical in the sense that it is entangled, and reduction in the uncertainty of S components can be attributed to correlations between individual spins [181].

Measuring m exactly produces a maximally squeezed state, but precise determination of this value is not always possible. Nevertheless, measuring m with some uncertainty $\Delta_m < \Delta_N$ will still produce a state with reduced uncertainty in S_z , as illustrated in Fig. 8.2 [172]. Here the measurement projector is [184, 185]

$$\Upsilon_{\Delta_m}(\tilde{m}) = \frac{1}{\sqrt{\pi \Delta_N^2}} \exp \left[-\frac{(S_z - \tilde{m})^2}{2\Delta_m^2} \right]. \quad (8.18)$$

representing a measurement where we have some Gaussian uncertainty (Δ_m) in the measured result. In the next section we will see how to implement this measurement in a CaF chip system to create squeezed states.

8.2 Spin ensemble coupled to a cavity

8.2.1 Spin Hamiltonian

We now turn to the case of $N \gg 1$ spins coupled strongly to a nearby microwave cavity. Assume that the coupling between each spin and the resonator photons is the same (that is, the coupling is homogeneous), then the ensemble is described by

the Tavis-Cummings Hamiltonian [186]

$$H_{\text{TC}} = \hbar\omega_c a^\dagger a + \sum_{i=1}^N \left[\frac{\hbar\omega_0}{2} \sigma_z^i + \frac{\hbar\Omega}{2\sqrt{N}} (a^\dagger \sigma_-^i + a \sigma_+^i) \right] \quad (8.19)$$

in direct analogy to eqn (7.22), and similar to optical cavity experiments [181, 182]. We can also write this Hamiltonian in terms of the collective spin operator

$$H_{\text{TC}} = \hbar\omega_c a^\dagger a + \hbar\omega_0 S_z + \frac{\hbar\Omega}{2\sqrt{N}} (a^\dagger S_- + a S_+). \quad (8.20)$$

Consider the dispersive regime ($|\Delta| \gg g$) and apply the transformation by unitary operator

$$U_E = \exp \left[\frac{g}{\Delta} (a S_+ - a^\dagger S_-) \right] \quad (8.21)$$

which results in the Hamiltonian

$$H_E = U_E H_{\text{TC}} U_E^\dagger \approx \hbar\omega_c a^\dagger a + \hbar \left(\omega_c + \frac{g^2}{\Delta} \right) S_z + \frac{\hbar g^2}{\Delta \sqrt{N}} S_z a^\dagger a. \quad (8.22)$$

This is an extension of the transformation (eqn (7.39)) and resulting Hamiltonian (eqn (7.40)) for the single-molecule case. This extension is valid since the mathematics of the transformation is exactly the same as for the single-spin case. The operator \mathbf{S} has the same commutation relations as the analogous \mathbf{s}^i . Once again, the final term will allow the information transfer for our QND measurements.

8.2.2 Quantum non-demolition measurement of the spin state

We now apply the readout method described for a single spin in section 7.4.1 to performing a quantum non-demolition (QND) measurement of the ensemble state. We will show that the state of the system can be entangled with light in the resonator, in exact analogy with the single-molecule case. Measurement of this light can then implement the squeezing projector in eqn (8.18).

The molecules can be prepared in the state $|+\rangle$ by the usual microwave spectroscopy techniques described in Ref. [85]. The state of the spin ensemble at time $t = 0$ is then

$$|\Psi(0)\rangle = \sum_{m=-S}^S \sqrt{P(m)} |S, m\rangle |\alpha\rangle, \quad (8.23)$$

where $|\alpha\rangle$ is the coherent state of light defined in eqn (7.41). The state evolves during the interaction with the resonator over a time T to

$$|\Psi(T)\rangle = \exp(-iH_{\text{int}}T/\hbar) |\Psi(0)\rangle, \quad (8.24)$$

where the interaction Hamiltonian is

$$H_{\text{int}} = \hbar \frac{g^2}{\Delta \sqrt{N}} S_z a^\dagger a. \quad (8.25)$$

After the pulse, we therefore have the state

$$|\Psi(T)\rangle = \sum_{m=-S}^S \sqrt{P(m)} e^{-i\nu_N T S_z a^\dagger a} |S, m\rangle |\alpha\rangle \quad (8.26)$$

with $\nu_N = g^2/(\Delta \sqrt{N})$. It is now straightforward to show that the state of the spin ensemble is entangled with the state of the light field, in analogy to equations 7.44–7.47

$$|\Psi(T)\rangle = e^{-\frac{|\alpha|^2}{2}} \sum_{m=-S}^S \sum_{n=0}^{\infty} \sqrt{P(m)} \frac{\alpha^n}{\sqrt{n!}} e^{-i\nu_N T S_z a^\dagger a} |S, m\rangle |n\rangle \quad (8.27)$$

$$= e^{-\frac{|\alpha|^2}{2}} \sum_{m=-S}^S \sum_{n=0}^{\infty} \sqrt{P(m)} \frac{\alpha^n}{\sqrt{n!}} e^{-i\nu_N T m n} |S, m\rangle |n\rangle \quad (8.28)$$

$$= \sum_{m=-S}^S \sqrt{P(m)} |S, m\rangle \left(e^{-\frac{|\alpha|^2}{2}} \sum_{n=0}^{\infty} \frac{(\alpha e^{-i\nu_N T m})^n}{\sqrt{n!}} |n\rangle \right) \quad (8.29)$$

$$= \sum_{m=-S}^S \sqrt{P(m)} |S, m\rangle \left| \alpha e^{-i\nu_N T m} \right\rangle. \quad (8.30)$$

Measuring the phase of the light leaving the cavity (for example with a homodyne detector) will therefore tell us something about the state of the ensemble. Notably, the information gained tells us only about the entire state of the ensemble, and not about any individual spins. Therefore the quantum coherence is preserved throughout this process [183, 184, 185].

The phase of the light is again extracted by the homodyne measurement, which was described in section 7.4.1. We will once again assume short interaction time so that $T \approx \kappa^{-1}$ and take the strong dispersive limit ($|\Delta| \gg g^2/\kappa$). The difference in photon numbers arriving at the homodyne detectors is therefore related to the spin ensemble by

$$\langle c^\dagger c - d^\dagger d \rangle = 2|\alpha||\beta| \frac{g^2}{\Delta\kappa} \langle S_z \rangle. \quad (8.31)$$

It is clear that performing the homodyne measurement is equivalent to performing a measurement of the S_z operator for the spins [185]. In order to distinguish between neighbouring S_z states, we must be able to resolve photon differences smaller than $2|\alpha||\beta|g^2/(\Delta\kappa)$. Since $|\beta|$ is large, this photon difference is amplified to make the measurement possible. In the event that neighbouring states are easily distinguishable, we can create states of the form $|S, m\rangle$. However if there is some

uncertainty in the homodyne measurement¹ Δ_m then the homodyne measurement realises the projector given in eqn (8.18). The result of the homodyne heralds the creation of a state

$$|\Phi(\tilde{m}, \Delta_m)\rangle = \frac{\Upsilon_{\Delta_m}(\tilde{m}) |+\rangle}{\sqrt{P_{\tilde{m}}}}, \quad (8.32)$$

where $P_{\tilde{m}}$ is the probability of obtaining the result \tilde{m} , and must be determined. At this point we have dropped the ket representing the state of the light. Although we have a QND measurement on the spins, this process destroys the light state, and so it is no longer relevant.

This resulting state can be found as follows. Begin by calculating the numerator, that is the homodyne projector acting on $|\Psi(T)\rangle$

$$\Upsilon_{\Delta_m}(\tilde{m}) |+\rangle = \sum_{m=-S}^S \sqrt{P(m)} \Upsilon(\tilde{m}) |S, m\rangle |\alpha e^{-i\nu_N T^m}\rangle \quad (8.33)$$

$$= \frac{1}{\sqrt{\pi \Delta_N^2}} \sum_{m=-S}^S \sqrt{P(m)} \exp\left[-\frac{(m-\tilde{m})^2}{2\Delta_N^2}\right] |S, m\rangle. \quad (8.34)$$

We can immediately this use to find the probability of measuring \tilde{m}

$$P_{\tilde{m}} = \langle \Psi(T) | \Upsilon(\tilde{m}) | \Psi(T) \rangle \quad (8.35)$$

$$= \sum_{m'=-S}^S \sum_{m=-S}^S \sqrt{P(m') P(m)} \langle S, m' | \Upsilon(\tilde{m}) | S, m \rangle \quad (8.36)$$

$$= \sum_{m'=-S}^S \sum_{m=-S}^S \sqrt{P(m') P(m)} \frac{1}{\sqrt{2\pi \Delta_m^2}} \exp\left[-\frac{(m-\tilde{m})^2}{2\Delta_m^2}\right] \langle S, m' | S, m \rangle \quad (8.37)$$

$$= \sum_{m=-S}^S P(m) \frac{1}{\sqrt{2\pi \Delta_{S_z}^2}} \exp\left[-\frac{(m-\tilde{m})^2}{2\Delta_m^2}\right]. \quad (8.38)$$

Taking the large N limit, and approximating the summation as an integral, this last equality becomes a convolution of two Gaussians, so that

$$P_{\tilde{m}} = \frac{1}{\sqrt{2\pi(\Delta_N^2 + \Delta_m^2)}} \exp\left[-\frac{\tilde{m}^2}{2(\Delta_N^2 + \Delta_m^2)}\right]. \quad (8.39)$$

This becomes eqn (8.10) in the limit that $\Delta_m \rightarrow 0$ i.e., when the uncertainty in the homodyne detection is small we measure the state m according to its expected distribution given previously in eqn (8.10). If we have some large uncertainty in our measurement then the distribution that we measure is not the same as the expected distribution.

Finally we calculate the state resulting from the measurement using eqn (8.13),

¹I suggest that there is some fundamental lower limit to the uncertainty achievable in the homodyne measurement, which arises due to the fact that the coherent states are not orthogonal.

again taking the approximation that we are in the limit of large N , and also that $\Delta_m^2 \ll \Delta_N^2$,

$$|\Phi(\tilde{m}, \Delta_m)\rangle = \sum_{m=-S}^S \left\{ \frac{1}{\sqrt{2\pi\Delta_m^2}} \exp\left[-\frac{(m-\tilde{m})^2}{2\Delta_m^2}\right] \right\}^{\frac{1}{2}} |S, m\rangle \quad (8.40)$$

which is a state that has been squeezed in comparison to the initial spin state. The S_z distribution now has a width Δ_m^2 rather than Δ_N^2 , as illustrated in Fig. 8.2. Since the Heisenberg uncertainty principle must be obeyed, the reduction of uncertainty in S_z increases the uncertainty in S_y [172].

The squeezing is parameterised by the quantity [187]

$$\chi^2 = \left(\frac{\sqrt{N}/2}{\Delta_m} \frac{|S|^2}{N/2} \right)^2, \quad (8.41)$$

where the first fraction inside the brackets is the ratio of the projection noise to the reduced uncertainty, and the second fraction accounts for any decoherence that occurs during the measurement. Decoherence or loss of particles will result in a decrease in the length of the Bloch vector $|S|$, and hence reduce the precision of a measurement. Hence any useful squeezing must reduce such effects. Squeezing occurs in the case that $\chi^2 > 1$, which is known as the Wineland criterion.

8.3 Implementation on CaF chip

For the CaF chip implementation of this squeezing procedure, we propose that the stretched-states can be used for the ground and excited states, as in the previous chapter. So $|g\rangle = |N=0, F=1, m_F=1\rangle$ and $|e\rangle = |1, 2, 2\rangle$. We assume that the resonator used is a high- Q ($Q \sim 10^6$) superconducting resonator, with a superconducting dimple trap, so that high trapping frequencies and trap depths are achievable. The values of g , Δ and κ from chapter 7 are assumed.

The squeezing that can be achieved on the chip is then dependent on three main factors:

1. The number of molecules that can be trapped, N
2. The uncertainty in the homodyne measurement.
3. The number of spins that decay during the interrogation time,

We have already addressed the number of molecules that it is possible to trap on a chip in detail in chapter 4. Maximising the phase-space density of molecules before trapping on the chip will increase N , but we can certainly expect to be working in

the regime of $N \gtrsim 10^3$. We also expect that the majority of these spins will remain trapped over an interrogation time of $T \sim \kappa^{-1}$, since superpositions of the stretched states have lifetimes in the trap on the order of several hundred milliseconds [85, 92].

The uncertainty in the homodyne measurement determines the uncertainty in S_z , and hence the extent of the squeezing. However, relating these two quantities analytically is non-trivial (although a more formal treatment can be found in Refs. [185] and [188]) and will largely depend on experimental factors, including thermal and electronic noise. However using eqn (8.31) we can make a good approximation that for squeezing of width Δ_m , we require measurement uncertainty in photon number

$$\Delta_\gamma < 2|\alpha||\beta| \frac{g^2}{\Delta\kappa\sqrt{N}} \Delta_m. \quad (8.42)$$

A naive approach to reducing the required uncertainty for squeezing might be to simply increase the LO amplitude ($|\beta|$) arbitrarily. Note however that the noise associated with the measurement of photons is Poissonian, and goes like the square root of the photon number, which is exactly $|\beta|$. Therefore increasing $|\beta|$ on the right side of the inequality makes reduction of Δ_γ on the left side harder.

It is therefore instructive to consider the quantity $\Delta_\gamma/|\beta|$ as a function of the probe amplitude ($|\alpha|$) and the other parameters of the cavity system. The requisite photon uncertainty to achieve a given squeezing can be found numerically. The results for a -50 dBm probe power and $N = 200$ are shown in Fig. 8.3. This figure shows that for sufficiently small uncertainty in the photon measurement (shown here in relation to pump power, $\Delta_\gamma/|\beta|$) the uncertainty in S_z (Δ_m) is reduced below the SQL. For our chosen probe power, the critical value to induce squeezing is $\Delta_\gamma/|\beta| = 36$. We also see the corresponding increase in the uncertainty in the other components of \mathbf{S} , which we parameterise as $\Delta_{S_{x,y}} = \sqrt{\Delta_{S_x}^2 + \Delta_{S_y}^2}$. This result demonstrates that the experiment operates in the regime where squeezing is certainly possible with conventional microwave detectors [189, 190], however this does not account for other sources of noise that may arise during the experiment.

Finally, we rephrase the squeezing in terms of the squeezing parameter eqn (8.41). We again anticipate from the free space microwave spectroscopy experiments [85] that there will be minimal dephasing and loss of spins over the timescale of our experiment. We present the squeezing parameter for various decreases of $|S|$ in Fig. 8.4. We anticipate an input power of $P \sim -50$ dBm, which is typical of that found in microwave resonator experiments [147].

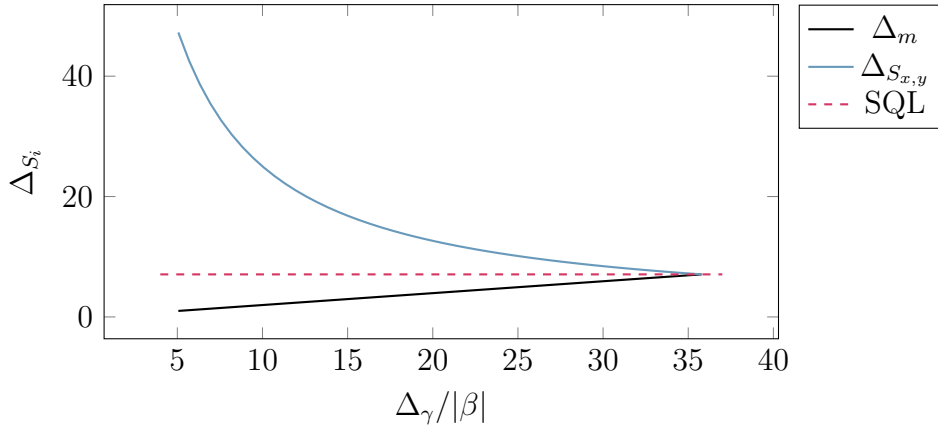


Figure 8.3: The squeezing (reduction in Δ_m) and anti-squeezing (increase in uncertainty in other components of \mathbf{S}) versus the uncertainty in homodyne photon detection. In this example we take $N = 200$, with SQL $\sqrt{N}/2 = 10/\sqrt{2}$ highlighted.

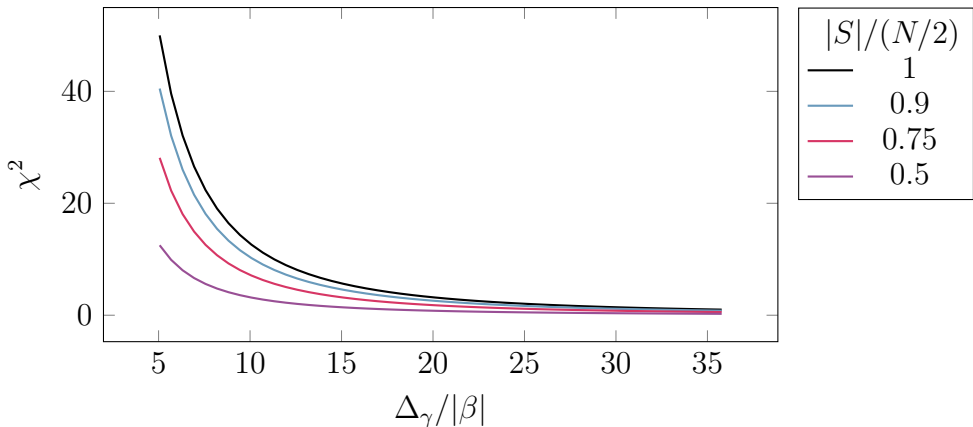


Figure 8.4: The squeezing parameter χ^2 is shown versus the homodyne measurement uncertainty to pump noise ratio $\Delta_\gamma/|\beta|$ for various spin losses $|S|/(N/2)$. We take $g/2\pi = 125$ kHz, $\kappa/2\pi = 21$ kHz, $P = -50$ dBm and $N = 200$.

8.4 Outlook

Although the main concept presented here has been to prepare non-classical SSS for measurement, this proposal has several possible routes for further development.

One example is to produce Schrödinger cat states, which have potential applications in understanding fundamental quantum physics, quantum information and communication [191] and were discussed in the context of light in section 7.4.2. Such states can be generated by performing the SSS creation procedure, except measuring the X quadrature of the light rather than the Y quadrature. This can be done by choosing the phase to be $\varphi = \pi/2$ (see eqn (7.53)). Since $X = |\alpha| \cos(\nu \langle S_z \rangle)$ and cosine is an even function, this prevents the gain on any information of the sign of the measured S_z value [188, 192]. The resulting state can be represented on the Bloch sphere as a pair of SSSs with equal widths, at $m = \pm \tilde{m}$, as illustrated in

Fig. 8.5.

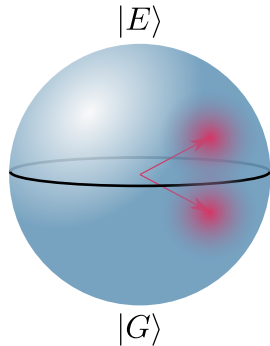


Figure 8.5: A Schrödinger cat spin state created by measurement of the X quadrature of cavity light is represented on the Bloch sphere.

Another possibility is to implement a maser system demonstrating superradiance. This idea was originally proposed in Ref. [175]. In a two-level system in population inversion it is possible to observe a rapid collective decay into the ground state. The decay rate scales as

$$\tau_{\text{Dicke}} \propto \frac{1}{N} \quad (8.43)$$

and can produce a bright pulse of light at the resonant frequency. The pulse will travel favourably in the longest dimension of the spin ensemble, which can be easily controlled by the shape of the trapping wires. A further idea is to investigate superradiance in close proximity to a microwave resonator, similar to what is discussed in Ref. [193].

A further possible development is using the coupling of two spin ensembles to a resonator to induce two-mode squeezing between those ensembles. Such a scheme has previously been implemented for nitrogen-vacancy ensembles in the dispersive regime [194]. As a related, final thought, it is possible the spin-squeezing proposal described above could be applied to a nitrogen-vacancy ensemble in close proximity to a CPW resonator. The same could be possible with other spin ensemble systems such as Rydberg atoms. These schemes are however beyond the scope of this discussion.

Chapter 9

Outlook

In this thesis I have outlined the work that has been undertaken to design and build a microfabricated chip trap for ultracold molecules. This device implements a series of magnetic traps for loading from the existing CaF experiment and bringing the molecules close to the chip surface by a series of current ramps. Molecules can be dropped from the chip for imaging with the RROC scheme described in chapter 6. The chip has been designed so that a second generation device can include an additional layer for microwave components which could be used to directly drive rotational transitions in the molecules. Such experiments will be useful in exploring the dynamics of cold molecules in the proximity of macroscopic bodies and in the microwave near field.

Future experiments could seek to implement a superconducting microwave cavity and realise the procedures described in chapters 7 and 8 for performing state readout, sideband cooling and preparation of non-classical states. There are various technical obstacles that must be overcome to achieve this, chiefly the requirement of high Q microwave cavities, which can only feasibly be implemented by the use of superconductors. This would require the installation of additional cooling for the superconductors, which would not be possible without significant changes to the existing apparatus. This remains a feasible long term goal for a third generation device, and a single level device with superconducting trapping wires could simultaneously simplify and enhance the experiment.

Along with the integration of superconducting microwave components, it may be useful to develop other tools for cold molecules to enable such an experiment. One example is the use of an optical dipole trap before the trapping stage to increase phase-space density before loading. Alternatively a mirror or grating MOT integrated with a chip, similar to those that were described in section 1.1 could be a convenient and effective way for forming a CaF MOT for loading into the chip trap. By loading such a MOT directly from a source this could avoid the losses that occur during molecular transport. Similarly, it would be useful to develop a method for

cooling the molecules on or near the chip, which is prohibited by the limited optical access in the experiment described here.

Another potential consideration is the implementation of transport or loading via an optical dipole trap, which could achieve efficient transport, or directly load a single molecule into an on-chip trap. Another idea is to use the dipole trap to contain the molecules in close proximity to a substrate with only microwave components. This could be a useful scheme for achieving strong coupling between rotational transitions and microwave photons, but would sacrifice some of the simplicity of an entirely integrated electronic device.

The molecule chip is a promising device for future experiments, with potential applications in quantum information and communications, as well as promising a robust platform for future experiments with ultracold molecules. This thesis has presented a prototype device with trapping capabilities that are ready to be demonstrated. It is the first step towards future generations of the experiment, bringing us closer to a fully-integrated electrical experiment for trapping and control of ultracold molecules.

Bibliography

- [1] N. Fitch and M. Tarbutt. “Chapter Three - Laser-cooled molecules”. In: ed. by L. F. Dimauro, H. Perrin and S. F. Yelin. Vol. 70. Advances In Atomic, Molecular, and Optical Physics. Academic Press, 2021, pp. 157–262.
- [2] A. André et al. “A coherent all-electrical interface between polar molecules and mesoscopic superconducting resonators”. In: *Nature Physics* 2 (Aug. 2006), pp. 636–642.
- [3] W. D. Phillips. “Nobel Lecture: Laser cooling and trapping of neutral atoms”. In: *Rev. Mod. Phys.* 70 (3 July 1998), pp. 721–741.
- [4] H. J. Metcalf and P. van der Straten. *Laser cooling and trapping*. 1st ed. Springer-Verlag New York, 1999.
- [5] D. J. Wineland, R. E. Drullinger and F. L. Walls. “Radiation-Pressure Cooling of Bound Resonant Absorbers”. In: *Phys. Rev. Lett.* 40 (25 June 1978), pp. 1639–1642.
- [6] S. Andreev et al. “Radiative slowing and reduction of the energy spread of a beam of sodium atoms to 1. 5 K in an oppositely directed laser beam”. In: *JETP Lett. (Engl. Transl.); (United States)* 34:8 (Oct. 1981).
- [7] W. D. Phillips and H. Metcalf. “Laser Deceleration of an Atomic Beam”. In: *Phys. Rev. Lett.* 48 (9 Mar. 1982), pp. 596–599.
- [8] J. V. Prodan and W. D. Phillips. “Chirping the light-fantastic? Recent NBS atom cooling experiments”. In: *Progress in Quantum Electronics* 8.3 (1984), pp. 231–235.
- [9] E. L. Raab et al. “Trapping of Neutral Sodium Atoms with Radiation Pressure”. In: *Phys. Rev. Lett.* 59 (23 Dec. 1987), pp. 2631–2634.
- [10] P. D. Lett et al. “Observation of Atoms Laser Cooled below the Doppler Limit”. In: *Phys. Rev. Lett.* 61 (2 July 1988), pp. 169–172.
- [11] J. Dalibard and C. Cohen-Tannoudji. “Laser cooling below the Doppler limit by polarization gradients: simple theoretical models”. In: *J. Opt. Soc. Am. B* 6.11 (Nov. 1989), pp. 2023–2045.
- [12] A. L. Migdall et al. “First Observation of Magnetically Trapped Neutral Atoms”. In: *Phys. Rev. Lett.* 54 (24 June 1985), pp. 2596–2599.
- [13] S. Chu et al. “Experimental Observation of Optically Trapped Atoms”. In: *Phys. Rev. Lett.* 57 (3 July 1986), pp. 314–317.
- [14] N. Schlosser et al. “Sub-poissonian loading of single atoms in a microscopic dipole trap”. In: *Nature* 411.6841 (June 2001), pp. 1024–1027.

- [15] M.-y. Wu et al. “Stable optical trapping and sensitive characterization of nanostructures using standing-wave Raman tweezers”. In: *Scientific Reports* 7.1 (Feb. 2017), p. 42930.
- [16] M. H. Anderson et al. “Observation of Bose-Einstein Condensation in a Dilute Atomic Vapor”. In: *Science* 269.5221 (1995), pp. 198–201.
- [17] K. B. Davis et al. “Bose-Einstein Condensation in a Gas of Sodium Atoms”. In: *Phys. Rev. Lett.* 75 (22 Nov. 1995), pp. 3969–3973.
- [18] F. Schäfer et al. “Tools for quantum simulation with ultracold atoms in optical lattices”. In: *Nature Reviews Physics* 2.8 (Aug. 2020), pp. 411–425.
- [19] M. A. Norcia et al. “Frequency Measurements of Superradiance from the Strontium Clock Transition”. In: *Phys. Rev. X* 8 (2 May 2018), p. 021036.
- [20] Y.-J. Chen et al. “Single-Source Multiaxis Cold-Atom Interferometer in a Centimeter-Scale Cell”. In: *Phys. Rev. Applied* 12 (1 July 2019), p. 014019.
- [21] B. Stray et al. “Quantum sensing for gravity cartography”. In: *Nature* 602.7898 (Feb. 2022), pp. 590–594.
- [22] P. Wcisło et al. “New bounds on dark matter coupling from a global network of optical atomic clocks”. In: *Science Advances* 4.12 (2018), eaau4869.
- [23] L. Badurina et al. “AION: an atom interferometer observatory and network”. In: *Journal of Cosmology and Astroparticle Physics* 2020.05 (May 2020), pp. 011–011.
- [24] K. I. Lee et al. “Single-beam atom trap in a pyramidal and conical hollow mirror”. In: *Opt. Lett.* 21.15 (Aug. 1996), pp. 1177–1179.
- [25] J. Reichel, W. Hänsel and T. W. Hänsch. “Atomic Micromanipulation with Magnetic Surface Traps”. In: *Phys. Rev. Lett.* 83 (17 Oct. 1999), pp. 3398–3401.
- [26] G. N. Lewis et al. “Fabrication of Magneto-optical Atom Traps on a Chip”. In: *Journal of Microelectromechanical Systems* 18.2 (Apr. 2009), pp. 347–353.
- [27] C. C. Nshii et al. “A surface-patterned chip as a strong source of ultracold atoms for quantum technologies”. In: *Nature Nanotechnology* 8 (Apr. 2013), p. 321.
- [28] J. D. Weinstein and K. G. Libbrecht. “Microscopic magnetic traps for neutral atoms”. In: *Phys. Rev. A* 52 (5 Nov. 1995), pp. 4004–4009.
- [29] V. Vuletic et al. “Microscopic Magnetic Quadrupole Trap for Neutral Atoms with Extreme Adiabatic Compression”. In: *Phys. Rev. Lett.* 80 (8 Feb. 1998), pp. 1634–1637.
- [30] J. Fortagh et al. “Miniaturized Wire Trap for Neutral Atoms”. In: *Phys. Rev. Lett.* 81 (24 Dec. 1998), pp. 5310–5313.
- [31] M. Drndić et al. “Micro-electromagnets for atom manipulation”. In: *Applied Physics Letters* 72.22 (1998), pp. 2906–2908.
- [32] J. Denschlag, D. Cassettari and J. Schmiedmayer. “Guiding Neutral Atoms with a Wire”. In: *Phys. Rev. Lett.* 82 (10 Mar. 1999), pp. 2014–2017.
- [33] R. Folman et al. “Controlling Cold Atoms using Nanofabricated Surfaces: Atom Chips”. In: *Phys. Rev. Lett.* 84 (20 May 2000), pp. 4749–4752.

- [34] W. Hänsel et al. “Bose–Einstein condensation on a microelectronic chip”. In: *Nature* 413.6855 (Oct. 2001), pp. 498–501.
- [35] H. Ott et al. “Bose-Einstein Condensation in a Surface Microtrap”. In: *Phys. Rev. Lett.* 87 (23 Nov. 2001), p. 230401.
- [36] B. Rauer et al. “Cooling of a One-Dimensional Bose Gas”. In: *Phys. Rev. Lett.* 116 (3 Jan. 2016), p. 030402.
- [37] S. Hofferberth et al. “Non-equilibrium coherence dynamics in one-dimensional Bose gases”. In: *Nature* 449.7160 (Sept. 2007), pp. 324–327.
- [38] B. Yuen et al. “Enhanced oscillation lifetime of a Bose–Einstein condensate in the 3D/1D crossover”. In: *New Journal of Physics* 17.9 (Sept. 2015), p. 093041.
- [39] M. H. Schleier-Smith, I. D. Leroux and V. Vuletić. “States of an Ensemble of Two-Level Atoms with Reduced Quantum Uncertainty”. In: *Phys. Rev. Lett.* 104 (7 Feb. 2010), p. 073604.
- [40] R. Gerritsma et al. “Lattice of microtraps for ultracold atoms based on patterned magnetic films”. In: *Phys. Rev. A* 76 (3 Sept. 2007), p. 033408.
- [41] Y.-J. Wang et al. “Atom Michelson Interferometer on a Chip Using a Bose-Einstein Condensate”. In: *Phys. Rev. Lett.* 94 (9 Mar. 2005), p. 090405.
- [42] S. Knappe et al. “A microfabricated atomic clock”. In: *Applied Physics Letters* 85.9 (2004), pp. 1460–1462.
- [43] F. Ramírez-Martínez et al. “Compact frequency standard using atoms trapped on a chip”. In: *Advances in Space Research* 47.2 (2011), pp. 247–252.
- [44] K. Frye et al. “The Bose-Einstein Condensate and Cold Atom Laboratory”. In: *EPJ Quantum Technology* 8.1 (Jan. 2021), p. 1.
- [45] P. Treutlein et al. “Coherence in Microchip Traps”. In: *Phys. Rev. Lett.* 92 (20 May 2004), p. 203005.
- [46] P. Treutlein. “Coherent manipulation of ultracold atoms on atom chips”. PhD thesis. Max-Planck-Institut für Quantenoptik, 2008.
- [47] P. Böhi et al. “Coherent manipulation of Bose-Einstein condensates with state-dependent microwave potentials on an atom chip”. In: *Nature Physics* 5 (July 2009), p. 592.
- [48] T. Nirrengarten et al. “Realization of a Superconducting Atom Chip”. In: *Phys. Rev. Lett.* 97 (20 Nov. 2006), p. 200405.
- [49] C. Roux et al. “Bose-Einstein condensation on a superconducting atom chip”. In: *EPL (Europhysics Letters)* 81.5 (Feb. 2008), p. 56004.
- [50] D. Cano et al. “Meissner Effect in Superconducting Microtraps”. In: *Phys. Rev. Lett.* 101 (18 Oct. 2008), p. 183006.
- [51] S. Bernon et al. “Manipulation and coherence of ultra-cold atoms on a superconducting atom chip”. In: *Nature Communications* 4 (Aug. 2013), p. 2380.
- [52] H. Hattermann et al. “Coupling ultracold atoms to a superconducting coplanar waveguide resonator”. In: *Nature Communications* 8.1 (Dec. 2017), p. 2254.

- [53] T. Aoki et al. “Observation of strong coupling between one atom and a monolithic microresonator”. In: *Nature* 443.7112 (Oct. 2006), pp. 671–674.
- [54] A. A. Morgan and S. D. Hogan. “Coupling Rydberg Atoms to Microwave Fields in a Superconducting Coplanar Waveguide Resonator”. In: *Phys. Rev. Lett.* 124 (19 May 2020), p. 193604.
- [55] R. Alarcon et al. *Electric dipole moments and the search for new physics*. 2022.
- [56] C. J. Foot. *Atomic Physics*. Oxford University press, 2005.
- [57] A. Blais et al. “Cavity quantum electrodynamics for superconducting electrical circuits: An architecture for quantum computation”. In: *Phys. Rev. A* 69 (6 June 2004), p. 062320.
- [58] S. Kim et al. “Enhanced coherence of all-nitride superconducting qubits epitaxially grown on silicon substrate”. In: *Communications Materials* 2.1 (Sept. 2021), p. 98.
- [59] M. P. Köppinger et al. “Production of optically trapped $^{87}\text{RbCs}$ Feshbach molecules”. In: *Phys. Rev. A* 89 (3 Mar. 2014), p. 033604.
- [60] J. D. Weinstein et al. “Magnetic trapping of calcium monohydride molecules at millikelvin temperatures”. In: *Nature* 395 (Sept. 1998), p. 148.
- [61] H. L. Bethlem, G. Berden and G. Meijer. “Decelerating Neutral Dipolar Molecules”. In: *Phys. Rev. Lett.* 83 (8 Aug. 1999), pp. 1558–1561.
- [62] H. L. Bethlem et al. “Electrostatic trapping of ammonia molecules”. In: *Nature* 406 (Aug. 2000), pp. 491–.
- [63] F. M. Crompvoets et al. “A prototype storage ring for neutral molecules”. In: *Nature* 411.6834 (May 2001), pp. 174–176.
- [64] F. M. H. Crompvoets. “A Storage Ring for Neutral Molecules”. PhD thesis. Radboud Universiteit Nijmegen., 2005.
- [65] S. E. Maxwell et al. “High-Flux Beam Source for Cold, Slow Atoms or Molecules”. In: *Phys. Rev. Lett.* 95 (17 Oct. 2005), p. 173201.
- [66] D. Patterson and J. M. Doyle. “Bright, guided molecular beam with hydrodynamic enhancement”. In: *The Journal of Chemical Physics* 126.15 (2007), p. 154307.
- [67] J. F. Barry, E. S. Shuman and D. DeMille. “A bright, slow cryogenic molecular beam source for free radicals”. In: *Phys. Chem. Chem. Phys.* 13 (42 2011), pp. 18936–18947.
- [68] E. S. Shuman et al. “Radiative Force from Optical Cycling on a Diatomic Molecule”. In: *Phys. Rev. Lett.* 103 (22 Nov. 2009), p. 223001.
- [69] J. F. Barry et al. “Laser Radiation Pressure Slowing of a Molecular Beam”. In: *Phys. Rev. Lett.* 108 (10 Mar. 2012), p. 103002.
- [70] J. F. Barry et al. “Magneto-optical trapping of a diatomic molecule”. In: *Nature* 512 (Aug. 2014), pp. 286–.
- [71] E. B. Norrgard et al. “Submillikelvin Dipolar Molecules in a Radio-Frequency Magneto-Optical Trap”. In: *Phys. Rev. Lett.* 116 (6 Feb. 2016), p. 063004.

- [72] Y. Wu et al. “High Phase-Space Density of Laser-Cooled Molecules in an Optical Lattice”. In: *Phys. Rev. Lett.* 127 (26 Dec. 2021), p. 263201.
- [73] J. J. Hudson et al. “Improved measurement of the shape of the electron”. In: *Nature* 473.7348 (May 2011), pp. 493–496.
- [74] N. J. Fitch et al. “Methods for measuring the electron’s electric dipole moment using ultracold YbF molecules”. In: *Quantum Science and Technology* 6.1 (Dec. 2020), p. 014006.
- [75] V. Zhelyazkova et al. “Laser cooling and slowing of CaF molecules”. In: *Phys. Rev. A* 89 (5 May 2014), p. 053416.
- [76] S. Truppe et al. “A buffer gas beam source for short, intense and slow molecular pulses”. In: *Journal of Modern Optics* 65.5-6 (2018), pp. 648–656.
- [77] S. Truppe et al. “An intense, cold, velocity-controlled molecular beam by frequency-chirped laser slowing”. In: *New Journal of Physics* 19.2 (2017), p. 022001.
- [78] B. Hemmerling et al. “Laser slowing of CaF molecules to near the capture velocity of a molecular MOT”. In: *Journal of Physics B: Atomic, Molecular and Optical Physics* 49.17 (2016), p. 174001.
- [79] H. J. Williams et al. “Characteristics of a magneto-optical trap of molecules”. In: *New Journal of Physics* 19.11 (2017), p. 113035.
- [80] L. Anderegg et al. “Radio Frequency Magneto-Optical Trapping of CaF with High Density”. In: *Phys. Rev. Lett.* 119 (10 Sept. 2017), p. 103201.
- [81] M. R. Tarbutt and T. C. Steimle. “Modeling magneto-optical trapping of CaF molecules”. In: *Phys. Rev. A* 92 (5 Nov. 2015), p. 053401.
- [82] M. T. Hummon et al. “2D Magneto-Optical Trapping of Diatomic Molecules”. In: *Phys. Rev. Lett.* 110 (14 Apr. 2013), p. 143001.
- [83] S. Truppe et al. “Molecules cooled below the Doppler limit”. In: *Nature Physics* 13 (Aug. 2017), pp. 1173–.
- [84] L. Caldwell et al. “Deep Laser Cooling and Efficient Magnetic Compression of Molecules”. In: *Phys. Rev. Lett.* 123 (3 July 2019), p. 033202.
- [85] H. J. Williams et al. “Magnetic Trapping and Coherent Control of Laser-Cooled Molecules”. In: *Phys. Rev. Lett.* 120 (16 Apr. 2018), p. 163201.
- [86] L. Anderegg. “Ultracold molecules in optical arrays: from laser cooling to molecular collisions”. PhD thesis. Harvard University, 2019.
- [87] X. Alauze et al. “An ultracold molecular beam for testing fundamental physics”. In: *Quantum Science and Technology* 6.4 (July 2021), p. 044005.
- [88] N. J. Fitch and M. R. Tarbutt. “Principles and Design of a Zeeman-Sisyphus Decelerator for Molecular Beams”. In: *ChemPhysChem* 17.22 (2016), pp. 3609–3623.
- [89] B. L. Augenbraun et al. “Zeeman-Sisyphus Deceleration of Molecular Beams”. In: *Phys. Rev. Lett.* 127 (26 Dec. 2021), p. 263002.
- [90] S. Jurgilas et al. “Collisions between Ultracold Molecules and Atoms in a Magnetic Trap”. In: *Phys. Rev. Lett.* 126 (15 Apr. 2021), p. 153401.

- [91] J. A. Blackmore et al. “Ultracold molecules for quantum simulation: rotational coherences in CaF and RbCs”. In: *Quantum Science and Technology* 4.1 (Dec. 2018), p. 014010.
- [92] L. Caldwell et al. “Long Rotational Coherence Times of Molecules in a Magnetic Trap”. In: *Phys. Rev. Lett.* 124 (6 Feb. 2020), p. 063001.
- [93] S. Burchesky et al. “Rotational Coherence Times of Polar Molecules in Optical Tweezers”. In: *Phys. Rev. Lett.* 127 (12 Sept. 2021), p. 123202.
- [94] A. Micheli, G. K. Brennen and P. Zoller. “A toolbox for lattice-spin models with polar molecules”. In: *Nature Physics* 2.5 (May 2006), pp. 341–347.
- [95] R. Sawant et al. “Ultracold polar molecules as qudits”. In: *New Journal of Physics* 22.1 (Jan. 2020), p. 013027.
- [96] H. Son et al. *Collisional Cooling of Ultracold Molecules*. 2019.
- [97] S. Jurgilas. “Collisions Between Laser-Cooled Atoms and Molecules”. PhD thesis. Imperial College London, 2021.
- [98] S. Jurgilas et al. “Collisions in a dual-species magneto-optical trap of molecules and atoms”. In: *New Journal of Physics* 23.7 (July 2021), p. 075004.
- [99] N. B. Vilas et al. *Magneto-Optical Trapping and Sub-Doppler Cooling of a Polyatomic Molecule*. 2021.
- [100] Z. D. Romaszko et al. “Engineering of microfabricated ion traps and integration of advanced on-chip features”. In: *Nature Reviews Physics* 2.6 (June 2020), pp. 285–299.
- [101] S. A. Meek et al. “Trapping Molecules on a Chip in Traveling Potential Wells”. In: *Phys. Rev. Lett.* 100 (15 Apr. 2008), p. 153003.
- [102] S. A. Meek, H. Conrad and G. Meijer. “Trapping Molecules on a Chip”. In: *Science* 324.5935 (2009), pp. 1699–1702.
- [103] J. Binney and D. Skinner. *The Physics of Quantum Mechanics*. OUP Oxford, 2013.
- [104] J. P. Cotter et al. “Design and fabrication of diffractive atom chips for laser cooling and trapping”. In: *Applied Physics B* 122.6 (June 2016), p. 172.
- [105] D. Müller et al. “Guiding Neutral Atoms Around Curves with Lithographically Patterned Current-Carrying Wires”. In: *Phys. Rev. Lett.* 83 (25 Dec. 1999), pp. 5194–5197.
- [106] K. Nakagawa et al. “Simple and efficient magnetic transport of cold atoms using moving coils for the production of Bose-Einstein condensation”. In: *Applied Physics B* 81.6 (Oct. 2005), pp. 791–794.
- [107] D. M. Brink and C. V. Sukumar. “Majorana spin-flip transitions in a magnetic trap”. In: *Phys. Rev. A* 74 (3 Sept. 2006), p. 035401.
- [108] J. Reichel and V. Vuletić. *Atom chips*. Wiley-VCH, 2011.
- [109] S. Du and E. Oh. “Three-wire magnetic trap for direct forced evaporative cooling”. In: *Phys. Rev. A* 79 (1 Jan. 2009), p. 013407.
- [110] J. M. Brown and A. Carrington. *Rotational Spectroscopy of Diatomic Molecules*. Cambridge Molecular Science. Cambridge University Press, 2003.

- [111] E. Zak. *Normal modes. The true story.* en. 2015.
- [112] B. Bransden and C. Joachain. *Physics of Atoms and Molecules*. Prentice Hall, 2003.
- [113] A. G. Tobin et al. “Evaluation of charcoal sorbents for helium cryopumping in fusion reactors”. In: *Journal of Vacuum Science & Technology A* 5.1 (1987), pp. 101–105.
- [114] S. C. Mathavan et al. “Deceleration of a Supersonic Beam of SrF Molecules to 120 meter per second”. In: *ChemPhysChem* 17.22 (2016), pp. 3709–3713.
- [115] L. Anderegg et al. “An optical tweezer array of ultracold molecules”. In: *Science* 365.6458 (2019), pp. 1156–1158.
- [116] J. A. Devlin and M. R. Tarbutt. “Three-dimensional Doppler, polarization-gradient, and magneto-optical forces for atoms and molecules with dark states”. In: *New Journal of Physics* 18.12 (2016), p. 123017.
- [117] H. Williams. “Producing, trapping and controlling ultracold CaF molecules”. PhD thesis. Imperial College London, 2018.
- [118] M. Weidemüller et al. “A Novel Scheme for Efficient Cooling below the Photon Recoil Limit”. In: *Europhysics Letters (EPL)* 27.2 (July 1994), pp. 109–114.
- [119] D. J. McCarron et al. “Magnetic Trapping of an Ultracold Gas of Polar Molecules”. In: *Phys. Rev. Lett.* 121 (1 July 2018), p. 013202.
- [120] S. Jurgilas et al. “Collisions in a dual-species magneto-optical trap of molecules and atoms”. In: *New Journal of Physics* 23.7 (July 2021), p. 075004.
- [121] H. J. Lewandowski et al. “Simplified System for Creating a Bose-Einstein Condensate”. In: *Journal of Low Temperature Physics* 132.5 (Sept. 2003), pp. 309–367.
- [122] S. C. Wright, T. E. Wall and M. R. Tarbutt. “Microwave trap for atoms and molecules”. In: *Phys. Rev. Research* 1 (3 Oct. 2019), p. 033035.
- [123] S. Y. Buhmann et al. “Surface-induced heating of cold polar molecules”. In: *Phys. Rev. A* 78 (5 Nov. 2008), p. 052901.
- [124] C. P. Wen. “Coplanar Waveguide: A Surface Strip Transmission Line Suitable for Nonreciprocal Gyromagnetic Device Applications”. In: *IEEE Transactions on Microwave Theory and Techniques* 17.12 (Dec. 1969), pp. 1087–1090.
- [125] C. McGarry. *USP*. <https://github.com/mcgarc/USP>. 2022.
- [126] A. Lichtenberg. *Phase-space Dynamics of Particles*. Wiley Series in Probability and Mathematical Statistics. Wiley, 1969.
- [127] L. Hand and J. Finch. *Analytical Mechanics*. Cambridge University Press, 1998.
- [128] S. Blundell and K. Blundell. *Concepts in Thermal Physics*. OUP Oxford, 2009.
- [129] C. G. Townsend et al. “Phase-space density in the magneto-optical trap”. In: *Phys. Rev. A* 52 (2 Aug. 1995), pp. 1423–1440.

- [130] L. Landau and E. Lifshitz. *Mechanics: Volume 1*. Vol. 1. Elsevier Science, 1982.
- [131] L. W. Cheuk et al. “ Λ -Enhanced Imaging of Molecules in an Optical Trap”. In: *Phys. Rev. Lett.* 121 (8 Aug. 2018), p. 083201.
- [132] G. Van Rossum and F. L. Drake Jr. *Python reference manual*. Centrum voor Wiskunde en Informatica Amsterdam, 1995.
- [133] E. Hairer and G. Wanner. “Euler Methods, Explicit, Implicit, Symplectic”. In: *Encyclopedia of Applied and Computational Mathematics*. Ed. by B. Engquist. Berlin, Heidelberg: Springer Berlin Heidelberg, 2015, pp. 451–455.
- [134] D. Donnelly and E. Rogers. “Symplectic integrators: An introduction”. In: *American Journal of Physics* 73.10 (2005), pp. 938–945.
- [135] E. Ozturk. *Desolver*. 2019.
- [136] D. Griffiths. *Introduction to Electrodynamics*. Cambridge University Press, 2017.
- [137] J. Reichel. “Microchip traps and Bose–Einstein condensation”. In: *Applied Physics B* 74.6 (Apr. 2002), pp. 469–487.
- [138] M. Madou. *Fundamentals of Microfabrication: The Science of Miniaturization, Second Edition*. Taylor & Francis, 2002.
- [139] W. Ruythooren et al. “Electrodeposition for the synthesis of microsystems”. In: *Journal of Micromechanics and Microengineering* 10.2 (May 2000), pp. 101–107.
- [140] B. Lev. “Fabrication of Micro-Magnetic Traps for Cold Neutral Atoms”. In: *Quantum Info. Comput.* 3.5 (Sept. 2003), pp. 450–464.
- [141] E. Koukharenko et al. “Microfabrication of gold wires for atom guides”. In: *Sensors and Actuators A: Physical* 115.2 (2004), pp. 600–607.
- [142] E. Cohen and E. J. Lightfoot. “Coating Processes”. In: *Kirk-Othmer Encyclopedia of Chemical Technology*. American Cancer Society, 2011, pp. 1–68.
- [143] *Heidelberg Instruments*. 2020. URL: <https://heidelberg-instruments.com> (visited on 23/07/2020).
- [144] M. Schlesinger and M. Paunovic. *Modern Electroplating*. The ECS Series of Texts and Monographs. Wiley, 2011.
- [145] S. Etienne. private communication. Feb. 2020.
- [146] G. Harman. *Wire Bonding in Microelectronics*. McGraw-Hill Education, 2009.
- [147] M. Göppel et al. “Coplanar waveguide resonators for circuit quantum electrodynamics”. In: *Journal of Applied Physics* 104.11 (2008), p. 113904.
- [148] Pfeiffer Vacuum GmbH. *The Vacuum Technology Book*. Vol. 2. Pfeiffer Vacuum GmbH, Apr. 2013.
- [149] *Electronic Symbols Library*. 8th Apr. 2022.
- [150] J. C. Shaw, J. C. Schnaubelt and D. J. McCarron. “Resonance Raman optical cycling for high-fidelity fluorescence detection of molecules”. In: *Phys. Rev. Research* 3 (4 Dec. 2021), p. L042041.

- [151] R. Simons. *Coplanar Waveguide Circuits, Components, and Systems*. Wiley Series in Microwave and Optical Engineering. Wiley, 2004.
- [152] R. Collin. *Foundations for microwave engineering*. 2nd ed. Wiley India Pvt. Limited, 2007.
- [153] M. Y. Frankel et al. “Terahertz attenuation and dispersion characteristics of coplanar transmission lines”. In: *IEEE Transactions on Microwave Theory and Techniques* 39.6 (June 1991), pp. 910–916.
- [154] Y. M. Wei et al. “A novel coplanar waveguide resonator on flexible substrate”. In: *Optik* 127.20 (2016), pp. 9937–9941.
- [155] DuPont. “DuPont Kapton Summary of Properties”. In: (2022).
- [156] J. Krupka et al. “Measurements of Permittivity, Dielectric Loss Tangent, and Resistivity of Float-Zone Silicon at Microwave Frequencies”. In: *IEEE Transactions on Microwave Theory and Techniques* 54.11 (Nov. 2006), pp. 3995–4001.
- [157] J. Krupka et al. “Dielectric properties of semi-insulating silicon at microwave frequencies”. In: *Applied Physics Letters* 107.8 (2015), p. 082105.
- [158] T. Edwards and M. Steer. *Foundations for Microstrip Circuit Design*. IEEE Press. Wiley, 2016.
- [159] *PTFE/Woven Fiberglass/Ceramic Filled Laminate For Microwave Printed Circuit Boards*. Rogers Corporation. 2022.
- [160] P. K. Day et al. “A broadband superconducting detector suitable for use in large arrays”. In: *Nature* 425.6960 (Oct. 2003), pp. 817–821.
- [161] A. Wallraff et al. “Strong coupling of a single photon to a superconducting qubit using circuit quantum electrodynamics”. In: *Nature* 431 (Sept. 2004), p. 162.
- [162] J. M. Sage et al. “Study of loss in superconducting coplanar waveguide resonators”. In: *Journal of Applied Physics* 109.6 (2011), p. 063915.
- [163] G. Ponchak, A. Margomenos and L. Katehi. “Low-loss CPW on low-resistivity Si substrates with a micromachined polyimide interface layer for RFIC interconnects”. In: *IEEE Transactions on Microwave Theory and Techniques* 49.5 (2001), pp. 866–870.
- [164] C. Gerry and P. Knight. *Introductory Quantum Optics*. Cambridge University Press, 2004.
- [165] A. Edmonds. *Angular Momentum in Quantum Mechanics*. Investigations in Physics Series. Princeton University Press, 1996.
- [166] A. Morgan. “Coupling Rydberg atoms to superconducting microwave circuits”. PhD thesis. University College London, 19th Apr. 2020.
- [167] S.-X. Li and J. B. Kycia. “Applying a direct current bias to superconducting microwave resonators by using superconducting quarter wavelength band stop filters”. In: *Applied Physics Letters* 102.24 (2013), p. 242601.
- [168] R. Barends et al. “Minimizing quasiparticle generation from stray infrared light in superconducting quantum circuits”. In: *Applied Physics Letters* 99.11 (2011), p. 113507.

- [169] J.-P. Gazeau. *Coherent States in Quantum Physics*. 2009.
- [170] G. S. Agarwal. *Quantum Optics*. Cambridge University Press, 2012.
- [171] B. Hacker et al. “Deterministic creation of entangled atom-light Schrödinger-cat states”. In: *Nature Photonics* 13 (2 1st Feb. 2019), pp. 110–115.
- [172] W. M. Itano et al. “Quantum projection noise: Population fluctuations in two-level systems”. In: *Phys. Rev. A* 47 (5 May 1993), pp. 3554–3570.
- [173] M. Kitagawa and M. Ueda. “Squeezed spin states”. In: *Phys. Rev. A* 47 (6 June 1993), pp. 5138–5143.
- [174] C. Gross. “Spin squeezing, entanglement and quantum metrology with Bose-Einstein condensates”. In: *Journal of Physics B: Atomic, Molecular and Optical Physics* 45.10 (May 2012), p. 103001.
- [175] R. H. Dicke. “Coherence in Spontaneous Radiation Processes”. In: *Phys. Rev.* 93 (1 Jan. 1954), pp. 99–110.
- [176] J. Ma et al. “Quantum spin squeezing”. In: *Physics Reports* 509.2 (2011), pp. 89–165.
- [177] F. T. Arecchi et al. “Atomic Coherent States in Quantum Optics”. In: *Phys. Rev. A* 6 (6 Dec. 1972), pp. 2211–2237.
- [178] M. Schulte et al. “Prospects and challenges for squeezing-enhanced optical atomic clocks”. In: *Nature Communications* 11.1 (2020), p. 5955.
- [179] M. Takeuchi et al. “Spin Squeezing via One-Axis Twisting with Coherent Light”. In: *Phys. Rev. Lett.* 94 (2 Jan. 2005), p. 023003.
- [180] G.-R. Jin, Y.-C. Liu and W.-M. Liu. “Spin squeezing in a generalized one-axis twisting model”. In: *New Journal of Physics* 11.7 (July 2009), p. 073049.
- [181] K. Cox. “Quantum-Enhanced Measurements with Atoms in Cavities: Super-radiance and Spin Squeezing”. PhD thesis. Boulder, CO, 30th Nov. 2016, p. 178.
- [182] M. H. Schleier-Smith. “Cavity-enabled spin squeezing for a quantum-enhanced atomic clock”. PhD thesis. Massachusetts Institute of Technology, 2011.
- [183] T. Vanderbruggen et al. “Spin-squeezing and Dicke-state preparation by heterodyne measurement”. In: *Phys. Rev. A* 83 (1 Jan. 2011), p. 013821.
- [184] M. R. Vanner et al. “Pulsed quantum optomechanics”. In: *Proceedings of the National Academy of Sciences* 108.39 (2011), pp. 16182–16187.
- [185] H. Bao et al. “Spin squeezing of 1011 atoms by prediction and retrodiction measurements”. In: *Nature* 581.7807 (2020), pp. 159–163.
- [186] P. Kirton et al. “Introduction to the Dicke Model: From Equilibrium to Nonequilibrium, and Vice Versa”. In: *Advanced Quantum Technologies* 2.1-2 (2019), p. 1800043.
- [187] D. J. Wineland et al. “Spin squeezing and reduced quantum noise in spectroscopy”. In: *Phys. Rev. A* 46 (11 Dec. 1992), R6797–R6800.
- [188] Y.-L. Zhang et al. “Quantum state preparation of an atomic ensemble via cavity-assisted homodyne measurement”. In: 52.21 (Oct. 2019), p. 215003.

- [189] R. H. Dicke. “The Measurement of Thermal Radiation at Microwave Frequencies”. In: *Review of Scientific Instruments* 17.7 (1946), pp. 268–275.
- [190] S. K. Lamoreaux et al. “Analysis of single-photon and linear amplifier detectors for microwave cavity dark matter axion searches”. In: *Phys. Rev. D* 88 (3 Aug. 2013), p. 035020.
- [191] C. Song et al. “Generation of multicomponent atomic Schrödinger cat states of up to 20 qubits”. In: *Science* 365.6453 (2019), pp. 574–577.
- [192] G. S. Agarwal, R. R. Puri and R. P. Singh. “Atomic Schrödinger cat states”. In: *Phys. Rev. A* 56 (3 Sept. 1997), pp. 2249–2254.
- [193] J. Pan et al. “Experimental demonstration of an all-optical analogue to the superradiance effect in an on-chip photonic crystal resonator system”. In: *Phys. Rev. B* 81 (4 Jan. 2010), p. 041101.
- [194] S.-l. Ma et al. “Two-mode squeezed states of two separated nitrogen-vacancy-center ensembles coupled via dissipative photons of superconducting resonators”. In: *Phys. Rev. A* 99 (1 Jan. 2019), p. 012325.